HOKKAIDO UNIVERSITY

Title	Study on Microbial Extracellular Electron Transfer Mechanism Under Maintenance State
Author(s)	何, 佳倫
Degree Grantor	北海道大学
Degree Name	博士(理学)
Dissertation Number	甲第16866号
Issue Date	2026-03-25
DOI	https://doi.org/10.14943/doctoral.k16866
Doc URL	https://hdl.handle.net/2115/99711
Type	doctoral thesis
File Information	HO_CHIA-LUN.pdf, 全文

Hokkaido University Collection of Scholarly and Academic Papers : HUSCAP

Study on Microbial Extracellular Electron Transfer Mechanism Under Maintenance State

(メンテナンス代謝状態における細胞外電子移動に関する研究)

Thesis by

HO, CHIA-LUN

In Partial Fulfillment of the Requirements for
the degree of
Doctor of Science



Graduate School of Chemical Sciences and Engineering

Hokkaido University

Abstract

Microorganisms can sustain viability by maintaining low metabolism under energy-limited conditions, a condition that fundamentally reduces antibiotic effectiveness and complicates clinical treatment. Understanding how bacteria remain viable in such low-energy conditions is therefore essential. This dissertation investigates how bacteria exploit extracellular electron transfer (EET) to sustain metabolism under anaerobic, energy-limited conditions. Using *Pseudomonas aeruginosa* as a model organism, the author examined how redox-active metabolites (RAMs) mediate electron shuttling and how efflux pumps together with membrane permeability govern the efficiency of this process. The author further determined how these transport and energetic constraints shape survival over extended periods of metabolic limitation. Across four research chapters, the work follows a logical progression:

Chapter 1 introduces the core physiological requirements that bacteria must sustain under low-energy conditions, including redox homeostasis, proton-motive force, and membrane functionality. It further discusses how microbes employ EET to support minimal metabolic activity when conventional anaerobic respiration is restricted. In addition, this chapter outlines the antibiotic tolerance of bacteria while operating in such energetically constrained states. Together, these concepts provide the mechanistic framework necessary to understand the EET-dependent survival strategies examined in the subsequent chapters.

Chapter 2 establishes a quantitative platform for measuring low-energy metabolism. Through collaboration with the Newman laboratory at California Institute of Technology, Division of Biology and Biological Engineering, *P. aeruginosa* electrochemically incubated in the presence of RAMs were identified as maintaince

state without any growth. However, the limited throughput of electrochemical incubation was a crucial constrain to further explore the mechanism of maintenance state. To this end, the author used a 96-well electrochemical system, developed in-house, and quantified phenazine-1-carboxamide (PCN)–mediated EET across defined concentrations under strictly anaerobic conditions. Charge integration normalized to colony forming unit, the number of viable cells, yielded a cell-specific metabolic rate of approximately 3,000 electrons s^{-1} $cell^{-1}$, suggesting the minimal energetic requirement necessary to sustain viability without growth. This platform provides a high-throughput method for characterizing maintenance metabolism and forms the analytical foundation for the mechanistic studies in subsequent chapters.

Chapter 3 investigates the role of efflux pumps in maintenance metabolism. Although these systems are classically associated with antibiotic resistance, their bioenergetic functions in non-growing cells have remained poorly understood. Using a 96-well anaerobic electrochemical platform, the author genetically manipulated efflux activity to define its impact on *P, aeruginosa* metabolism. By examining efflux overexpression strains under maintenance state, the author demonstrated that efflux capacity governs metabolic throughput. During maintenance phase, efflux overexpression increases cell-specific metabolic rate, dissipating proton-motive force (PMF), imposing a significant energetic burden that not only fails to enhance antibiotic resistance but further reduces population survival under anaerobic conditions. The increased metabolic flux per cell is consistent with compensatory metabolism that restores PMF consumed by efflux activity—supported by membrane-potential measurements. These results establish efflux pumps as bioenergetic regulators rather than simple detoxification valves, coupling export, and metabolism.

Chapter 4 demonstrates that membrane permeability is a central determinant of RAM-mediated metabolism under maintenance state in the presence of other physiologically-

relavant RAM, pyocyanin (PYO). PCN, a low-permeability RAM, becomes limited by PMF-dependent export at high concentrations, leading to a metabolic plateau. In contrast, the more permeable PYO maintains unsaturated transport and continues to drive metabolic activity even when PMF is dissipated. PYO increased antibiotic sensitivity compared with PCN: higher PYO concentrations increase tobramycin killing in proportion to metabolic rate. Across a broader RAM panel, diffusion-associated current under PMF collapse strongly predicted total metabolic flux, indicating that hydrophobicity and molecular rigidity govern passive permeability in *P. aeruginosa*. Together, these findings identify membrane permeability as a key factor controlling electron-shuttle efficiency, metabolic throughput, and antibiotic susceptibility, and highlight highly permeable RAMs as potential tools to restore antibiotic efficacy under energy-limited conditions.

Chapter 5 extends these mechanistic insights to environmental microbiology by developing a rapid, culture-free tool to identify electroactive bacteria (EAB). Having shown in earlier chapters that EET is essential for survival under low-energy conditions, the author next asked which environmental microbes naturally possess strong EET capability. To address this, osmium-grafted magnetic nanobeads (M@FA-Os NPs) were created to selectively capture cells capable of DAB-polymer–mediated redox activity on their outer membranes. Because many EAB express outer-membrane cytochromes (OMCs) that catalyze DAB polymerization, M@FA-Os NPs associated specifically with *Shewanella oneidensis* MR-1, model EAB with OMCs, but not with EET-deficient *Escherichia coli* K-12. Magnetic enrichment increased MR-1 abundance, protein content, and current generation. Applied to environmental soil microbiota, the method shifted community composition toward putative electrogenic taxa, producing faster current onset, a 16-fold higher current peak, and greater long-term charge output. These results show that M@FA-Os NPs enable rapid and selective enrichment of EAB,

improving microbial electrochemical performance and facilitating the discovery of EET-related taxa and genes in complex environments.

Chapter 6 provides an overall summary of this dissertation and outlines future directions, including investigating additional cellular processes that may be essential under maintenance conditions—such as membrane and ionic homeostasis—and applying rapid EET-enrichment tools to examine the universality of EET-supported survival strategies in natural microbial communities. Together, these findings establish transport-governed EET as a central determinant of survival under energetic scarcity and offer methodological advances for uncovering EET-linked metabolic strategies across diverse microbial systems.

Table of Contents

Abstract ..... *i*

Table of Contents ..... *v*

Chapter 1 Introduction – Survival Strategies of Aerobes Under a Low-power Metabolic State *1*

1.1 Background *2*

1.1.1 Basic physiological requirements for survival 2

1.1.2 Anaerobic Metabolic Pathways maintained by extracellular electron transfer 4

1.1.3 Dule Role of Redox-Active Metabolites in Bacterial Survival 5

1.1.4 Bacterial Survival Strategies for Antibiotic Stress 7

1.2 Motivation *9*

1.3 Overview *10*

1.4 Figures *12*

1.5 References *16*

Chapter 2 Measurement of Phenazine-1-carboxamide-Mediated Maintenance Metabolism Using High-Throughput Electrochemical System *23*

2.1 Introduction *24*

2.2 Results *26*

2.2.1 Leveraging a high-throughput electrochemical platform facilitates systematic investigation of non-growth metabolism. 26

2.2.2 Attenuation of Cellular PCN Reduction Reveals a Metabolic Plateau Near the Maintenance Threshold 27

2.3 Discussion *28*

2.4 Methods and materials *30*

2.5 Figures *33*

2.6 References *36*

Chapter 3 Efflux pump activity limits metabolism during an anaerobic maintenance state powered by phenazines redox cycling *38*

3.1 Introduction *38*

3.2 Results *40*

3.2.1 Adaptation and maintenance phases reveal distinct metabolic controls in anaerobic PCN-mediated metabolism. 40

3.2.2 Efflux pumps coupled with the metabolic activity at high PCN concentration under adaption phase 41

3.2.3 The Energetic Cost of Maintaining PMF Shapes Baseline Metabolism During the Maintenance State 43

3.2.4 Efflux pump overexpression do not increase antibiotic resistance under a low-energy maintenance state. 46

3.3 Discussion *48*

3.4 Material and methods *54*

3.5 ›Figures *60*

3.6 Supplementary materials *65*

3.7 References *75*

Chapter 4 High-diffusion redox cycling enhances metabolism and increases antibiotic sensitivity under a low-energy condition *82*

4.1 Introduction *82*

4.2 Results *84*

4.2.1 PCN is PMF-limited while PYO is diffusion-driven in mediating anaerobic metabolism 84

4.2.2 Metabolic rate controlled by RAM concentration determines antibiotic sensitivity 86

4.2.3 Membrane permeability of RAMs predicts metabolic rate *P. aeruginosa* 87

4.3 Discussion *88*

4.4 Methods and materials *92*

4.5 Figures *94*

4.6 Table *98*

4.7 References *99*

Chapter 5 Osmium-grafted Magnetic Nanobeads Improve Microbial Current Generation via Culture-free and Quick Enrichment of Electrogenic Bacteria *102*

5.1 Introduction *103*

5.2 Results *106*

5.2.1 Synthesis and characterization of Os-exposed nanobeads 106

5.2.2 Capture of DAB-polymerized bacteria using M@FA-Os NPs 108

5.2.3 Current production in magnetically enriched inoculation from the soil sample .. 111

5.3 Discussion *115*

5.4 Conclusion *117*

5.5 Materials and methods *118*

5.6 Figures *124*

5.7 Supporting information *131*

5.8 References *146*

Chapter 6 Summary and Future Perspectives *153*

6.1 Summary *153*

6.2 Future perspectives *154*

6.2.1 Essential metabolic functions for survival under low-energy conditions 154

6.2.2 Can cells reach even lower metabolic states? 155

6.2.3 Applying rapid EET-enrichment tools to assess the generality of low-energy survival strategies across natural microbial ecosystems 156

6.3 References *156*

Published Content and Contributions *158*

Acknowledgment *159*

Chapter 1 Introduction – Survival Strategies of Aerobes Under a Low-power Metabolic State

All living cells, from humans to microbes, require a continuous supply of energy to sustain life. Such energy fuels not only growth, but also essential physiological processes such as maintaining redox balance, preserving membrane potential, and exporting toxic byproducts (1-3). However, during survival, the availability of energy resources is not always guaranteed. Microorganisms—particularly aerobic bacteria—frequently encounter environments where electron acceptors, most notably oxygen, are limited or temporarily unavailable. For instance, oxygen in moist soil is rapidly depleted (4, 5), and even within the human body, bacteria that colonize the lungs often become embedded in hypoxic or anoxic mucus (6, 7). Even the interior of their self-generated biofilms is frequently oxygen-depleted (8, 9). Such oxygen-limited conditions constrain the capacity of aerobes to generate ATP through respiration (10), pushing them into a low-power metabolic state—a condition of limited energy throughput where basic physiological functions become difficult to maintain (11). Although obligate aerobes are traditionally thought to depend strictly on oxygen (12), many studies have shown that they possess anaerobic survival mechanisms to overcome this metabolic challenge (13, 14)—namely, maintaining redox homeostasis and proton motive force (PMF) despite the disruption of the electron transport chain caused by the absence of oxygen. Notably, under such oxygen-limited conditions, bacteria often exhibit heightened resistance to antibiotics, posing a major challenge in both environmental and medical contexts (15, 16). However, these survival strategies remain understudied, even though they are to be likely ecologically and clinically significant. In this chapter, I introduce the current understanding of how facultative aerobes manage to survive and adapt under oxygen-limited and antibiotic-stressed conditions. Building

upon this foundation, this chapter will also delineate the research motivation, and overview in this thesis.

1.1 Background

1.1.1 Basic physiological requirements for survival

Compared to oxic conditions, where bacteria possess sufficient energy to support rapid growth, under anoxic conditions they instead prioritize the maintenance of essential physiological functions (1-3). Among these, sustaining a minimal level of proton motive force (PMF) appears to be critical, as numerous survival-related processes—including efflux pump-mediated waste export and ion transport for osmotic regulation—depend on PMF (17, 18). Under respiratory conditions, bacteria typically generate PMF via the electron transport chain (ETC), which then drives ATP synthesis through the F_1F_0-ATP synthase in a process known as oxidative phosphorylation (Figure 1) (19). However, under fermentative conditions, the F_1F_0-ATP synthase reverses its function, hydrolyzing ATP derived from substrate-level phosphorylation to sustain residual PMF in the absence of an active electron transport chain (Figure 1) (18, 20). Although numerous studies have demonstrated that chemically disrupting PMF using agents such as CCCP (carbonyl cyanide m-chlorophenyl hydrazone) or DCCD (N,N′-dicyclohexylcarbodiimide) compromises bacterial viability (20, 21), this does not necessarily imply that higher PMF levels always favor survival under anaerobic conditions. For instance, certain facultative aerobes such as *Bacillus subtilis* actively reduce their PMF under nutrient-limited conditions, which paradoxically improves their survival (22). These findings suggest that bacteria may finely tune their PMF levels to balance energy expenditure with essential physiological needs. While technical challenges remain under oxygen-limited conditions, several approaches have been developed to quantitatively or semi-quantitatively assess PMF at the single-cell

level—including genetically encoded fluorescent biosensors (inserted into the cytoplasmic membrane) (23), radiolabeled probes (e.g., [^{3}H]TPP^{+}, [^{14}C]benzoate) (21), and membrane potential-sensitive dyes (e.g., $DiOC_2(3)$) (24). Therefore, the investigation of PMF regulation under energy-limited states is becoming increasingly feasible and holds great promise for future discoveries.

Another critical factor for anaerobic survival is redox homeostasis, which is directly tied to ATP production and metabolic flux (25). Redox balance relies on several key cofactor pairs: NADH/NAD^{+}, which is primarily associated with energy conservation; NADPH/NADP^{+}, which supports biosynthesis and reductive metabolism; and GSH/GSSG, which functions in redox buffering and maintenance of protein disulfide bonds (26-29). Disruption of any of these redox systems can lead to significant declines in viability. For instance, in *Mycobacterium tuberculosis*, deletion of NADH dehydrogenases (Ndh-1 and Ndh-2) impairs NAD^{+} regeneration, disrupting redox balance and decreasing survival (30, 31). Even in the absence of ETC, alternative NADH oxidation pathways can enhance viability (31). In non-growing *Escherichia coli*, however, it is NADPH regeneration—rather than NADH abundance—that becomes rate limiting for redox reactions, underscoring the critical role of maintaining NADPH homeostasis (32, 33). In addition, glutathione safeguards thiol-containing enzymes through reversible S-glutathionylation, thereby preventing aberrant disulfide bond formation and protecting enzyme activity under oxidative stress (34, 35).

PMF and redox balance, particularly the NAD^{+}/NADH ratio, are tightly coupled. Under respiration, oxidation of NADH via the ETC not only regenerates NAD^{+} but also drives proton translocation to establish PMF (Figure 1) (19). Conversely, when PMF is artificially reinforced under anaerobic respiration, cells can display elevated ATP synthesis, accelerated nutrient utilization, expanded NADH/NAD^{+} pools, suggesting that PMF can in turn exert a reverse influence on redox balance (36). Under

fermentation, if the NAD^+/NADH balance collapses, substrate-level phosphorylation is impaired, leading to reduced ATP production (Figure 1). Consequently, the limited ATP supply constrains the ability of ATP synthase to hydrolyze ATP and sustain residual PMF levels (18, 20). Thus, PMF and the NAD^+/NADH balance reciprocally regulate each other, and their interplay critically shapes cellular metabolism, survival.

1.1.2 Anaerobic Metabolic Pathways maintained by extracellular electron transfer

Under oxygen-limited conditions, cells can generate energy through two main strategies: anaerobic respiration and fermentation. During anaerobic respiration, electrons from NADH are transferred through the electron transport chain (ETC) to non-oxygen terminal electron acceptors, establishing a proton motive force (PMF) that drives oxidative phosphorylation to produce ATP (37). The specific form of anaerobic respiration depends on the nature of the terminal electron acceptor. When soluble electron acceptors such as fumarate, sulfate, or nitrate are used, the entire ETC can operate within the inner membrane (37, 38). However, if the terminal electron acceptor is insoluble and located extracellularly, the ETC must be extended to the outer membrane (39). A classic example is *Shewanella oneidensis* MR-1, which utilize the MtrCAB-OmcA complex to transfer electrons from the inner membrane to outer-membrane-bound cytochromes, ultimately reducing extracellular insoluble acceptors such as Fe(III) or Mn(IV) oxides (40). This process, in which outer-membrane cytochromes directly donate electrons to extracellular electron acceptors, is referred to as **direct extracellular electron transfer (direct EET)**.

In contrast, fermentation occurs in the absence of external electron acceptors. Under such conditions, ATP is generated through substrate-level phosphorylation from carbon sources like glucose (41). To maintain redox balance, electrons from NADH produced

during glycolysis are transferred to internal organic intermediates such as pyruvate, which are further reduced into products like lactate or succinate. This regenerates NAD^+ and supports continued glycolytic flux (41). Notably, redox-active metabolites contribute to NAD^+ regeneration, with phenazines—endogenous metabolites produced by *Pseudomonas aeruginosa*—serving as a prominent example (42). In *P. aeruginosa*, arginine supports anaerobic survival via the arginine deiminase pathway, which directly generates ATP without involving redox-coupled reactions (20, 43). By contrast, when glucose is available, additional ATP synthesis beyond glycolytic pyruvate production relies on the conversion of pyruvate to acetate by acetate kinase, a process that requires NAD^+ regeneration to maintain redox balance (20). Phenazines facilitate this process by accepting electrons from NADH, restoring the NAD^+ pool and allowing continued metabolic flux (44). Reduced phenazines can be exported from the cell via diffusion or active efflux mechanisms; once in the extracellular space, they are reoxidized by external electron acceptors and can re-enter the cell to repeat the cycle (45). This bidirectional process, known as extracellular electron shuttling, contributes to redox homeostasis and sustained ATP production under anaerobic conditions. Such electron transfer process effectively supplements fermentative metabolism by regenerating NAD^+, a process conceptually akin to facilitated fermentation (46).

1.1.3 Dule Role of Redox-Active Metabolites in Bacterial Survival

Redox-active metabolites (RAMs) act as a double-edged sword in bacterial physiology. Under anaerobic conditions, they serve as alternative electron acceptors, enabling the maintenance of both energy production and redox homeostasis (42). However, due to their high redox activity, these molecules can become cytotoxic in the presence of oxygen by reacting with molecular oxygen to generate reactive oxygen species (ROS) (47). Pyocyanin (PYO), a major phenazine derivative produced by *P. aeruginosa*,

exemplifies this duality (48). In anoxic or hypoxic conditions such as the biofilm core, PYO helps maintain redox balance by acting as an extracellular electron shuttle, accepting intracellular electrons and ultimately transferring them to oxygen at the biofilm surface. (44, 49). Conversely, under oxic conditions, the reduced form of PYO readily reacts with oxygen to form superoxide and hydrogen peroxide. These ROS cause oxidative damage that can lead to cell death and trigger the release of extracellular DNA (eDNA), which contributes to the structural integrity of the biofilm matrix (48, 49). Importantly, the toxicity of PYO is not limited to aerobic conditions. Even in the absence of oxygen, PYO can exert toxic effects, suggesting that the reduced form of PYO itself imposes physiological stress independent of ROS generation (48).

To combat PYO toxicity, *P. aeruginosa* activates multiple defense mechanisms. These include antioxidant systems such as AhpCF and KatB , which detoxify ROS (50, 51); efflux pumps such as MexEF-OprN and MexGHI-OpmD, which export PYO from the cell (52, 53); and Fe-S cluster biogenesis systems that repair redox-sensitive enzymes and restore cellular function (51, 54). These responses not only protect the cell from its own toxic metabolites but also confer cross-protection against antibiotics through the co-activation of shared defense pathways. In addition to its redox toxicity, pyocyanin (PYO) can suppress bacterial bioenergetic states by dissipating membrane potential under oxic conditions, thereby promoting antibiotic tolerance (24). These diverse effects of PYO underscore its complex role in bacterial survival. In addition to these defensive responses, PYO also intersects with quorum sensing networks. Through SoxR-mediated induction of MexGHI-OpmD, PYO links efflux activity to the export of quinolone signal precursors, thereby facilitating quorum-sensing–dependent community behaviors such as biofilm formation and virulence factor production (55).

Beyond PYO, other endogenous redox-active metabolites (RAMs) exhibit similar survival-supporting functions. These include additional phenazine derivatives such as

phenazine-1-carboxamide (PCN) and phenazine-1-carboxylic acid (PCA), toxoflavin from *Burkholderia gladioli* and actinorhodin from *Streptomyces coelicolor* (56-59). The widespread occurrence and functional relevance of these metabolites underscore the universality of RAMs as critical modulators of bacterial physiology and stress adaptation.

1.1.4 Bacterial Survival Strategies for Antibiotic Stress

Antibiotics remain among the most effective and widely employed interventions against bacterial infections. Their extensive use spans clinical practice, animal husbandry, agriculture, and environmental management, with far-reaching consequences for both human health and global ecosystems (60). However, the therapeutic efficacy of antibiotics is increasingly challenged by the rise of antibiotic resistance, which hampers the complete eradication of bacterial pathogens (61).

Several factors contribute to the development of antibiotic resistance. In natural environments, bacteria predominantly exist in the form of slow-growing biofilms rather than planktonic cells (62). Within these biofilms, the extracellular matrix—composed of polysaccharides, extracellular DNA, and proteins—forms a highly adhesive barrier that delays or restricts antibiotic penetration (62). Although certain antibiotics, such as ciprofloxacin, are capable of diffusing into the biofilm core, the microenvironment within is often hypoxic (8, 9). This condition drives cells into a low-power metabolic state, thereby reducing the efficacy of antibiotics whose bactericidal activity is tightly coupled to active metabolism (15, 63). Even in the oxygen-rich outer layers of the biofilm, bacteria deploy defense mechanisms—most notably efflux pumps, which actively export antibiotics to prevent intracellular accumulation and reduce cytotoxicity (64, 65). Importantly, efflux pump activity is not limited to the biofilm surface; their protective roles extend to the hypoxic core, underscoring their critical function across

both spatial and physiological gradients (66). Therefore, understanding how bacteria modulate their metabolic state and physiological responses to antibiotic stress is essential for developing strategies to overcome the limitations of current antibiotic therapies. One such regulatory mechanism involves the transcription factor SoxR, which modulates efflux pump expression across diverse bacterial species. In *Escherichia coli*, SoxR functions as a classical oxidative stress sensor, activating the *soxS* regulon to induce antioxidant defenses and efflux systems (67). In contrast, *Pseudomonas aeruginosa* and *Streptomyces coelicolor* utilize SoxR to directly activate efflux systems for endogenous redox-active metabolites such as phenazines and actinorhodin (55, 68). Interestingly, in *Acinetobacter baumannii*, SoxR functions as a repressor of efflux gene expression, and loss-of-function mutations are associated with multidrug resistance (69). These species-specific differences highlight the evolutionary flexibility of SoxR in adapting to various ecological and metabolic pressures. Despite this mechanistic diversity, SoxR universally influences efflux pump expression, reinforcing its importance as a global determinant of adaptive survival and antibiotic resistance.

In addition to SoxR, bacteria rely on global regulatory systems to enter a low-power metabolic state under energy-limited conditions. The stringent response, mediated by (p)ppGpp, downregulates RNA synthesis, thereby slowing metabolism and promoting antibiotic tolerance under nutrient starvation or antibiotic stress (70, 71). The stationary-phase sigma factor RpoS (σ^S) is a key switch that balances bacterial growth and survival (72). By competing for RNA polymerase with housekeeping sigma factor RpoD (σ^{70}), it represses growth-associated genes while activating stress-response genes, thereby shifting the cell into a low-power maintenance metabolic state under adverse conditions (72, 73). The cAMP–CRP complex functions as a pivotal positive regulator driving the entry of *E. coli* into the viable but non-culturable state (74). In *Pseudomonas*

aeruginosa, the Fnr-type transcription factor Anr senses oxygen limitation and activates genes required for fermentation (e.g., arcDABC and ackA-pta) as well as for anaerobic respiration (e.g., narXL) (75). Collectively, these regulatory systems reprogram bacterial physiology into a low-power metabolic state that supports survival under energy-limited conditions, while ensuring that resistance mechanisms such as efflux pumps remain functional even when cellular energy is scarce.

1.2 Motivation

Bacterial antibiotic resistance poses an escalating threat to public health and the environment (see detailed introduction in Section 1.1.4). While numerous studies have identified the low-power metabolic state as a major contributor to antibiotic tolerance, the mechanisms by which bacteria regulate energy generation and sustain essential physiological functions under such energy-limited conditions remain poorly understood.

During the early phase of my doctoral research (described in Chapter 5), I developed a culture-free electrochemical enrichment approach using osmium-grafted magnetic nanobeads to selectively capture electroactive bacteria from environmental samples (Ho et al., Chem. Eng. J. 2023). This study revealed that many naturally occurring bacteria sustain their survival through extracellular electron transfer processes and, as discussed earlier, predominantly persist in low-metabolic states, highlighting the ecological importance of electron transfer–mediated energy maintenance under oxygen-limited conditions. Building upon this perspective, my doctoral research transitions from population-level enrichment toward single-species physiology, employing *Pseudomonas aeruginosa* as a model system to mechanistically elucidate

how redox-active metabolites and efflux systems coordinate electron flow and cellular survival under low-energy conditions.

Phenazines, a representative class of redox-active metabolites (RAMs), are known to facilitate extracellular electron transfer and sustain redox homeostasis in the absence of oxygen. Because many bacteria exploit RAMs to maintain redox balance and support anaerobic respiration, this work not only provides mechanistic insight into phenazine-mediated metabolic regulation in P. aeruginosa but also contributes to a broader understanding of how bacteria adapt their metabolism to persist under energy-deprived states.

1.3 Overview

In Chapter 2, in collaboration with Professor Dianne Newman and Dr. John Ciemniecki at Caltech, I combined their expertise in *P. aeruginosa* physiology with Okamoto's group's high-throughput electrochemical platform to investigate anaerobic metabolism. I confirmed that under anaerobic conditions and in the presence of a sufficient concentration of phenazine-1-carboxamide (PCN), which is the most abundant phenazine in the inner layers of *P. aeruginosa* biofilms, cells can maintain survival for five days using high-throughput electrochemical platform. Remarkably, the cell-specific metabolic rate plateaued at approximately at ~3 x 10^3 e^- s^{-1} $cell^{-1}$ at 25˚C, suggesting a minimum energy requirement for maintenance. Interestingly, above a certain PCN concentration, survival remained constant, but metabolic rates did not continue to increase with the increase of PCN. This implies that cells may preferentially minimize energy expenditure rather than optimize fitness, prompting further investigation into the factors that limit or control metabolic rate under these conditions. Chapter 3 demonstrates that efflux capacity is the rate-limiting control point of PCN-

driven redox cycling and reveals efflux pumps as bioenergetic regulators that shape both short-term metabolic adaptation and long-term maintenance. Chapter 4 shows that membrane permeability is a key determinant of electron-shuttle efficiency, with highly permeable RAMs sustaining elevated metabolic rates that influence cellular susceptibility to antibiotics. Finally, Chapter 5 applies these mechanistic insights to natural microbial communities by developing osmium-grafted magnetic nanobeads capable of rapidly enriching environmental bacteria with strong EET capability.

Together, these studies provide a coherent view of how bacteria leverage redox-active metabolites and transport systems to endure extreme energetic scarcity. They also introduce methodological advances that broaden our ability to characterize, manipulate, and discover electroactive microorganisms across diverse ecological and clinical settings.

1.4 Figures

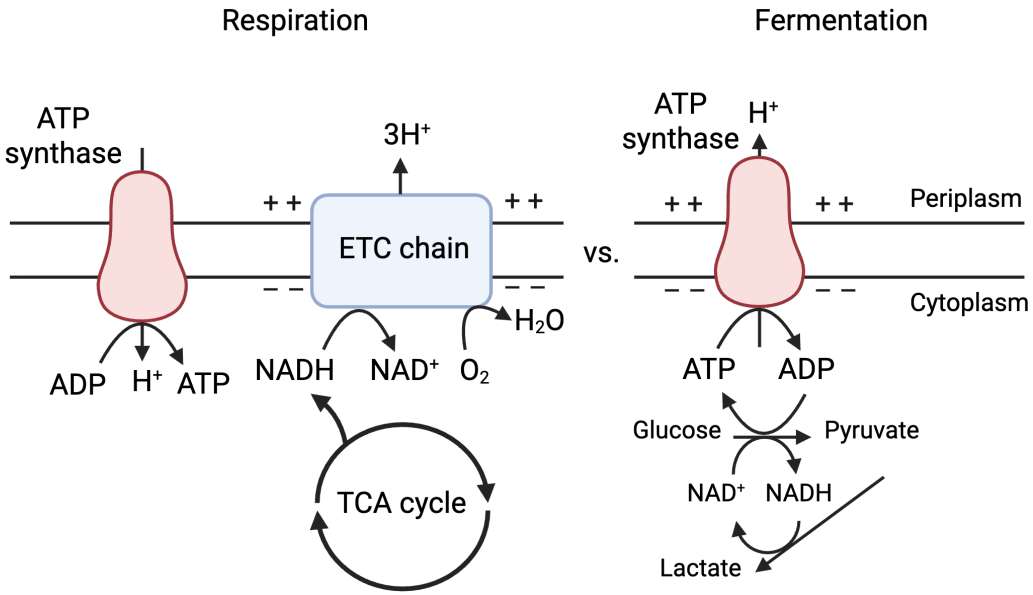


Figure 1. Coupling between PMF and the NAD^+/NADH redox balance under respiration and fermentation.

During respiration (left), NADH generated by the TCA cycle donates electrons to the electron transport chain (ETC), where oxygen serves as the terminal electron acceptor. Oxidation of NADH regenerates NAD^+ and drives proton translocation, establishing a proton motive force (PMF) that powers ATP synthase to produce ATP.

In fermentation (right), ATP is produced exclusively through substrate-level phosphorylation during glycolysis, where glucose is converted to pyruvate. NAD^+ is regenerated by reducing pyruvate to lactate, enabling glycolysis to continue in the absence of an external electron acceptor.

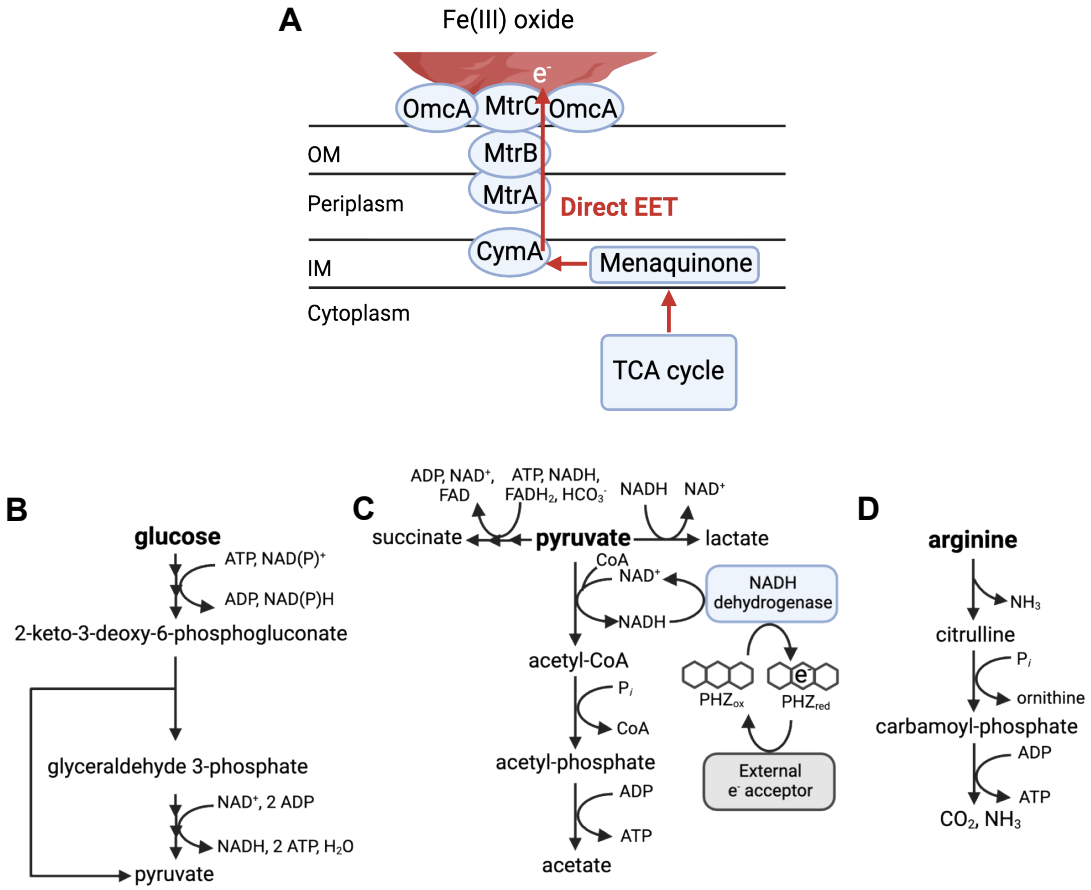


Figure 2. Anaerobic metabolic pathways in *S. oneidensis* MR-1 and *P. aeruginosa*.

(A) Anaerobic respiration with extracellular electron transfer (EET). In *Shewanella* species, electrons derived from NADH are funneled through the inner-membrane quinone pool (menaquinone) to CymA and periplasmic cytochromes and finally transferred via the MtrCAB-OmcA complex to extracellular insoluble acceptors such as Fe(III) oxides, enabling direct EET. (B-D) Metabolic pathways in *P. aeruginosa*, adapted from Glasser et al. (20) (B) Glucose oxidation via the Entner–Doudoroff pathway. (C) Pyruvate fermentation coupled with phenazine redox cycling regenerates NAD^+ and supports continued ATP synthesis. (D) The arginine deiminase pathway produces ATP independently of redox-coupled reactions through arginine catabolism.

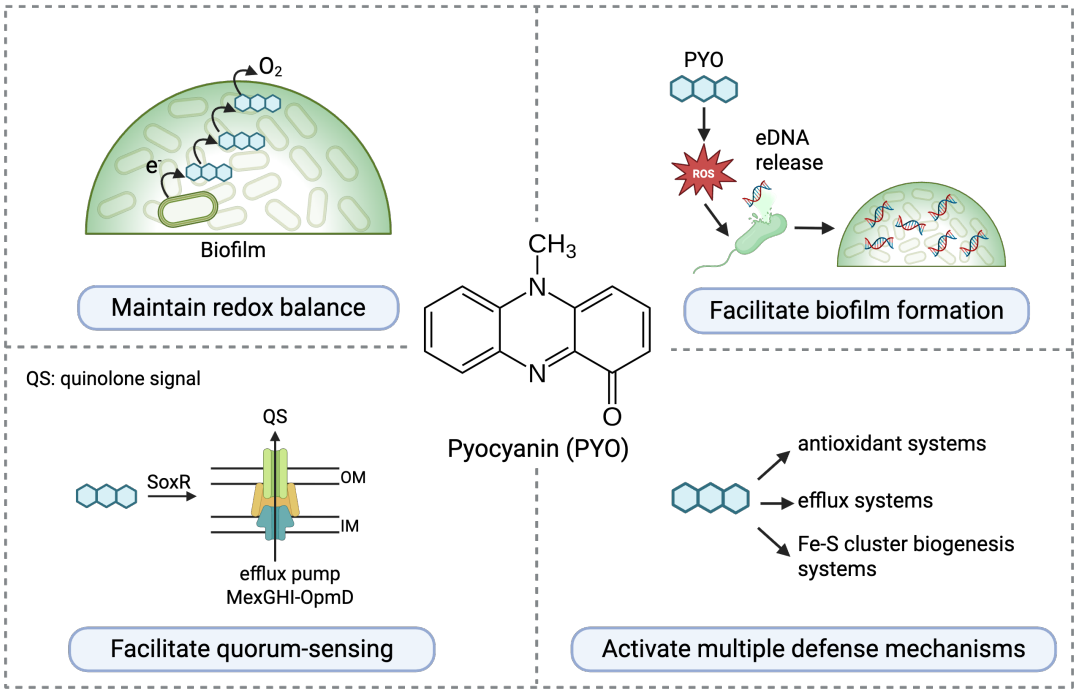


Figure 3. Multifaceted roles of pyocyanin (PYO) in *Pseudomonas aeruginosa*.

PYO acts as an extracellular electron shuttle to maintain redox balance, promotes biofilm formation, facilitates quorum sensing through SoxR–MexGHI-OpmD–mediated efflux, and triggers defense responses including antioxidant, efflux, and Fe–S cluster repair systems.

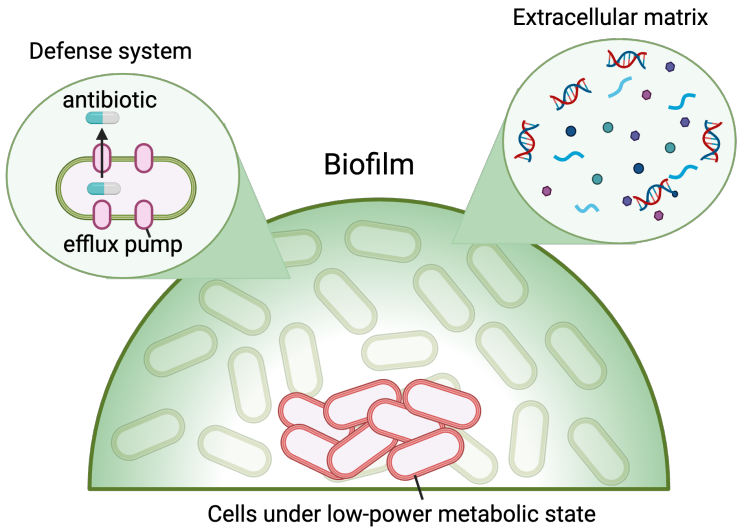


Figure 4. Multiple mechanisms of antibiotic resistance within biofilms.

Within biofilms, several factors contribute to antibiotic resistance. The extracellular matrix, composed of polysaccharides, extracellular DNA, and proteins, acts as a barrier that impedes antibiotic penetration. Cells in the biofilm core adopt a low-power metabolic state under hypoxic conditions, reducing the efficacy of metabolism-dependent antibiotics. In both the outer layers and the hypoxic core, bacteria employ efflux pumps to actively export antibiotics, preventing intracellular accumulation and enhancing survival.

1.5 References

1. K. Le Gal, E. E. Schmidt, V. I. Sayin, Cellular Redox Homeostasis. *Antioxidants* **10**, 1377 (2021).
2. A. L. Hodgkin, P. Horowicz, The influence of potassium and chloride ions on the membrane potential of single muscle fibres. *J Physiol* **148**, 127-160 (1959).
3. S. M. Soto, Role of efflux pumps in the antibiotic resistance of bacteria embedded in a biofilm. *Virulence* **4**, 223-229 (2013).
4. W. L. Silver, A. E. Lugo, M. Keller, Soil oxygen availability and biogeochemistry along rainfall and topographic gradients in upland wet tropical forest soils. *Biogeochemistry* **44**, 301-328 (1999).
5. E. M. Lacroix, R. J. Rossi, D. Bossio, S. Fendorf, Effects of moisture and physical disturbance on pore-scale oxygen content and anaerobic metabolisms in upland soils. *Science of The Total Environment* **780**, 146572 (2021).
6. E. S. Cowley, S. H. Kopf, A. LaRiviere, W. Ziebis, D. K. Newman, Pediatric Cystic Fibrosis Sputum Can Be Chemically Dynamic, Anoxic, and Extremely Reduced Due to Hydrogen Sulfide Formation. *mBio* **6**, 10.1128/mbio.00767-00715 (2015).
7. D. Worlitzsch *et al.*, Effects of reduced mucus oxygen concentration in airway Pseudomonas infections of cystic fibrosis patients. *The Journal of Clinical Investigation* **109**, 317-325 (2002).
8. K. D. Xu, P. S. Stewart, F. Xia, C.-T. Huang, G. A. McFeters, Spatial Physiological Heterogeneity in *Pseudomonas aeruginosa* Biofilm Is Determined by Oxygen Availability. *Applied and Environmental Microbiology* **64**, 4035-4039 (1998).
9. D. de Beer, P. Stoodley, F. Roe, Z. Lewandowski, Effects of biofilm structures on oxygen distribution and mass transport. *Biotechnology and Bioengineering* **43**, 1131-1138 (1994).
10. E. Gnaiger, Bioenergetics at low oxygen: dependence of respiration and phosphorylation on oxygen and adenosine diphosphate supply. *Respiration Physiology* **128**, 277-297 (2001).
11. M. D. McDonald *et al.*, What is microbial dormancy? *Trends in Microbiology* **32**, 142-150 (2024).
12. M. Berney, C. Greening, R. Conrad, W. R. Jacobs, G. M. Cook, An obligately aerobic soil bacterium activates fermentative hydrogen production to survive

reductive stress during hypoxia. *Proceedings of the National Academy of Sciences* **111**, 11479-11484 (2014).

13. C. Alvarez-Ortega, C. S. Harwood, Responses of Pseudomonas aeruginosa to low oxygen indicate that growth in the cystic fibrosis lung is by aerobic respiration. *Molecular Microbiology* **65**, 153-165 (2007).

14. S. Watanabe *et al.*, Fumarate Reductase Activity Maintains an Energized Membrane in Anaerobic Mycobacterium tuberculosis. *PLOS Pathogens* **7**, e1002287 (2011).

15. M. C. Walters, F. Roe, A. Bugnicourt, M. J. Franklin, P. S. Stewart, Contributions of Antibiotic Penetration, Oxygen Limitation, and Low Metabolic Activity to Tolerance of *Pseudomonas aeruginosa* Biofilms to Ciprofloxacin and Tobramycin. *Antimicrobial Agents and Chemotherapy* **47**, 317-323 (2003).

16. S. Gupta, N. Laskar, D. E. Kadouri, Evaluating the Effect of Oxygen Concentrations on Antibiotic Sensitivity, Growth, and Biofilm Formation of Human Pathogens. *Microbiology Insights* **9**, MBI.S40767 (2016).

17. I. T. Paulsen, M. H. Brown, R. A. Skurray, Proton-dependent multidrug efflux systems. *Microbiological Reviews* **60**, 575-608 (1996).

18. T. A. Krulwich, G. Sachs, E. Padan, Molecular aspects of bacterial pH sensing and homeostasis. *Nature Reviews Microbiology* **9**, 330-343 (2011).

19. P. Mitchell, Chemiosmotic coupling in oxidative and photosynthetic phosphorylation. *Biochimica et Biophysica Acta (BBA) - Bioenergetics* **1807**, 1507-1538 (2011).

20. N. R. Glasser, S. E. Kern, D. K. Newman, Phenazine redox cycling enhances anaerobic survival in *Pseudomonas aeruginosa* by facilitating generation of ATP and a proton-motive force. *Molecular Microbiology* **92**, 399-412 (2014).

21. S. P. S. Rao, S. Alonso, L. Rand, T. Dick, K. Pethe, The protonmotive force is required for maintaining ATP homeostasis and viability of hypoxic, nonreplicating Mycobacterium tuberculosis. *Proceedings of the National Academy of Sciences* **105**, 11945-11950 (2008).

22. H. A. Arjes *et al.*, Biosurfactant-Mediated Membrane Depolarization Maintains Viability during Oxygen Depletion in Bacillus subtilis. *Curr Biol* **30**, 1011-1022.e1016 (2020).

23. X. Jin *et al.*, Sensitive bacterial V_m sensors revealed the excitability of bacterial V_m and its role in antibiotic tolerance. *Proceedings of the National Academy of Sciences* **120**, e2208348120 (2023).

24. R. D. Horak, J. A. Ciemniecki, D. K. Newman, Bioenergetic suppression by redox-active metabolites promotes antibiotic tolerance in Pseudomonas aeruginosa. *Proceedings of the National Academy of Sciences* **121**, e2406555121 (2024).

25. A. Singh, K. Cher Soh, V. Hatzimanikatis, R. T. Gill, Manipulating redox and ATP balancing for improved production of succinate in E. coli. *Metabolic Engineering* **13**, 76-81 (2011).

26. A. Ciemniecki John, K. Newman Dianne, The Potential for Redox-Active Metabolites To Enhance or Unlock Anaerobic Survival Metabolisms in Aerobes. *Journal of Bacteriology* **202**, 10.1128/jb.00797-00719 (2020).

27. X. Chen, S. Li, L. Liu, Engineering redox balance through cofactor systems. *Trends in Biotechnology* **32**, 337-343 (2014).

28. R.-Y. Fu, J. Chen, Y. Li, The Function of the Glutathione/Glutathione Peroxidase System in the Oxidative Stress Resistance Systems of Microbial Cells. *Chinese Journal of Biotechnology* **23**, 770-775 (2007).

29. W. Ying, NAD+/NADH and NADP+/NADPH in Cellular Functions and Cell Death: Regulation and Biological Consequences. *Antioxidants & Redox Signaling* **10**, 179-206 (2007).

30. C. Vilchèze, B. Weinrick, L. W. Leung, W. R. Jacobs, Plasticity of Mycobacterium tuberculosis NADH dehydrogenases and their role in virulence. *Proceedings of the National Academy of Sciences* **115**, 1599-1604 (2018).

31. Y. Xu, S. Ehrt, D. Schnappinger, T. Beites, Synthetic lethality of Mycobacterium tuberculosis NADH dehydrogenases is due to impaired NADH oxidation. *mBio* **14**, e01045-01023 (2023).

32. A. Z. Walton, J. D. Stewart, Understanding and Improving NADPH-Dependent Reactions by Nongrowing Escherichia coli Cells. *Biotechnology Progress* **20**, 403-411 (2004).

33. V. Cracan, D. V. Titov, H. Shen, Z. Grabarek, V. K. Mootha, A genetically encoded tool for manipulation of NADP+/NADPH in living cells. *Nature Chemical Biology* **13**, 1088-1095 (2017).

34. L. López-Maury, M. Sánchez-Riego Ana, C. Reyes José, J. Florencio Francisco, The Glutathione/Glutaredoxin System Is Essential for Arsenate Reduction in Synechocystis sp. Strain PCC 6803. *Journal of Bacteriology* **191**, 3534-3543 (2009).

35. M. M. Gallogly, J. J. Mieyal, Mechanisms of reversible protein glutathionylation in redox signaling and oxidative stress. *Current Opinion in Pharmacology* **7**, 381-391 (2007).

36. W. Ding *et al.*, Proton motive force generated by microbial rhodopsin promotes extracellular electron transfer. *Synthetic and Systems Biotechnology* **10**, 410-420 (2025).

37. D. J. Richardson, Bacterial respiration: a flexible process for a changing environment1999 Fleming Lecture (Delivered at the 144th meeting of the Society for General Microbiology, 8 September 1999). *Microbiology* **146**, 551-571 (2000).

38. G. Unden, J. Bongaerts, Alternative respiratory pathways of Escherichia coli: energetics and transcriptional regulation in response to electron acceptors. *Biochimica et Biophysica Acta (BBA) - Bioenergetics* **1320**, 217-234 (1997).

39. K. Richter, M. Schicklberger, J. Gescher, Dissimilatory Reduction of Extracellular Electron Acceptors in Anaerobic Respiration. *Applied and Environmental Microbiology* **78**, 913-921 (2012).

40. L. Shi *et al.*, The roles of outer membrane cytochromes of Shewanella and Geobacter in extracellular electron transfer. *Environmental Microbiology Reports* **1**, 220-227 (2009).

41. A. J. Wolfe, The Acetate Switch. *Microbiology and Molecular Biology Reviews* **69**, 12-50 (2005).

42. Y. Wang, E. Kern Suzanne, K. Newman Dianne, Endogenous Phenazine Antibiotics Promote Anaerobic Survival of Pseudomonas aeruginosa via Extracellular Electron Transfer. *Journal of Bacteriology* **192**, 365-369 (2010).

43. C. V. Wauven, A. Piérard, M. Kley-Raymann, D. Haas, Pseudomonas aeruginosa mutants affected in anaerobic growth on arginine: evidence for a four-gene cluster encoding the arginine deiminase pathway. *Journal of Bacteriology* **160**, 928-934 (1984).

44. J. A. Ciemniecki, D. K. Newman, NADH dehydrogenases are the predominant phenazine reductases in the electron transport chain of Pseudomonas aeruginosa. *Molecular Microbiology* **119**, 560-573 (2023).

45. N. R. Glasser, S. H. Saunders, D. K. Newman, The Colorful World of Extracellular Electron Shuttles. *Annual Review of Microbiology* **71**, 731-751 (2017).

46. J. A. Ciemniecki, C.-L. Ho, R. D. Horak, A. Okamoto, D. K. Newman, Mechanistic study of a low-power bacterial maintenance state using high-throughput electrochemistry. *Cell* **187**, 6882-6895.e6888 (2024).

47. A. Price-Whelan, L. E. P. Dietrich, D. K. Newman, Rethinking 'secondary' metabolism: physiological roles for phenazine antibiotics. *Nature Chemical Biology* **2**, 71-78 (2006).

48. L. A. Meirelles, D. K. Newman, Both toxic and beneficial effects of pyocyanin contribute to the lifecycle of Pseudomonas aeruginosa. *Molecular Microbiology* **110**, 995-1010 (2018).

49. S. H. Saunders *et al.*, Extracellular DNA Promotes Efficient Extracellular Electron Transfer by Pyocyanin in *Pseudomonas aeruginosa* Biofilms. *Cell* **182**, 919-932.e919 (2020).

50. A. Ochsner Urs, L. Vasil Michael, E. Alsabbagh, K. Parvatiyar, J. Hassett Daniel, Role of the Pseudomonas aeruginosa oxyR-recG Operon in Oxidative Stress Defense and DNA Repair: OxyR-Dependent Regulation of katB-ankB, ahpB, andahpC-ahpF. *Journal of Bacteriology* **182**, 4533-4544 (2000).

51. L. E. P. Dietrich, T. K. Teal, A. Price-Whelan, D. K. Newman, Redox-Active Antibiotics Control Gene Expression and Community Behavior in Divergent Bacteria. *Science* **321**, 1203-1206 (2008).

52. D. Wolloscheck, G. Krishnamoorthy, J. Nguyen, H. I. Zgurskaya, Kinetic Control of Quorum Sensing in Pseudomonas aeruginosa by Multidrug Efflux Pumps. *ACS Infectious Diseases* **4**, 185-195 (2018).

53. H. Sakhtah *et al.*, The Pseudomonas aeruginosa efflux pump MexGHI-OpmD transports a natural phenazine that controls gene expression and biofilm development. *Proceedings of the National Academy of Sciences* **113**, E3538-E3547 (2016).

54. A. Romsang, J. M. Dubbs, S. Mongkolsuk, "The Iron–sulfur Cluster Biosynthesis Regulator IscR Contributes to Iron Homeostasis and Resistance to Oxidants in Pseudomonas Aeruginosa" in Stress and Environmental Regulation of Gene Expression and Adaptation in Bacteria. (2016), https://doi.org/10.1002/9781119004813.ch106, pp. 1090-1102.

55. L. E. P. Dietrich, A. Price-Whelan, A. Petersen, M. Whiteley, D. K. Newman, The phenazine pyocyanin is a terminal signalling factor in the quorum sensing network of Pseudomonas aeruginosa. *Molecular Microbiology* **61**, 1308-1321 (2006).

56. Y. Huang *et al.*, Endogenous phenazine-1-carboxamide encoding gene PhzH regulated the extracellular electron transfer in biocorrosion of stainless steel by marine Pseudomonas aeruginosa. *Electrochemistry Communications* **94**, 9-13 (2018).

57. Y. Wang *et al.*, Phenazine-1-Carboxylic Acid Promotes Bacterial Biofilm Development via Ferrous Iron Acquisition. *Journal of Bacteriology* **193**, 3606-3617 (2011).

58. J. Lee, J. Park, S. Kim, I. Park, Y.-S. Seo, Differential regulation of toxoflavin production and its role in the enhanced virulence of Burkholderia gladioli. *Molecular Plant Pathology* **17**, 65-76 (2016).

59. Y. Xu, A. Willems, C. Au-yeung, K. Tahlan, R. Nodwell Justin, A Two-Step Mechanism for the Activation of Actinorhodin Export and Resistance in Streptomyces coelicolor. *mBio* **3**, 10.1128/mbio.00191-00112 (2012).

60. W. H. Organization, *Global antimicrobial resistance and use surveillance system (GLASS) report 2022* (World Health Organization, 2022).

61. Y. Jee *et al.*, Antimicrobial resistance: a threat to global health. *The Lancet Infectious Diseases* **18**, 939-940 (2018).

62. J. W. Costerton, P. S. Stewart, E. P. Greenberg, Bacterial Biofilms: A Common Cause of Persistent Infections. *Science* **284**, 1318-1322 (1999).

63. M. A. Lobritz *et al.*, Antibiotic efficacy is linked to bacterial cellular respiration. *Proceedings of the National Academy of Sciences* **112**, 8173-8180 (2015).

64. L. A. Meirelles, E. K. Perry, M. Bergkessel, D. K. Newman, Bacterial defenses against a natural antibiotic promote collateral resilience to clinical antibiotics. *PLOS Biology* **19**, e3001093 (2021).

65. X.-Z. Li, P. Plésiat, H. Nikaido, The Challenge of Efflux-Mediated Antibiotic Resistance in Gram-Negative Bacteria. *Clinical Microbiology Reviews* **28**, 337-418 (2015).

66. I. Alav, J. M. Sutton, K. M. Rahman, Role of bacterial efflux pumps in biofilm formation. *Journal of Antimicrobial Chemotherapy* **73**, 2003-2020 (2018).

67. T. Nunoshiba, E. Hidalgo, C. F. A. Cuevas, B. Demple, Two-stage control of an oxidative stress regulon: the Escherichia coli SoxR protein triggers redox-inducible expression of the soxS regulatory gene. *Journal of Bacteriology* **174**, 6054-6060 (1992).

68. J.-H. Shin, K. Singh Atul, D.-J. Cheon, J.-H. Roe, Activation of the SoxR Regulon in Streptomyces coelicolor by the Extracellular Form of the Pigmented Antibiotic Actinorhodin. *Journal of Bacteriology* **193**, 75-81 (2011).

69. J. Dreier, P. Ruggerone, Interaction of antibacterial compounds with RND efflux pumps in Pseudomonas aeruginosa. *Frontiers in Microbiology* **Volume 6 - 2015** (2015).

70. D. R. Gentry, V. J. Hernandez, L. H. Nguyen, D. B. Jensen, M. Cashel, Synthesis of the stationary-phase sigma factor sigma s is positively regulated by ppGpp. *Journal of Bacteriology* **175**, 7982-7989 (1993).

71. J. K. Hobbs, A. B. Boraston, (p)ppGpp and the Stringent Response: An Emerging Threat to Antibiotic Therapy. *ACS Infectious Diseases* **5**, 1505-1517 (2019).

72. T. Nyström, MicroReview: Growth versus maintenance: a trade-off dictated by RNA polymerase availability and sigma factor competition? *Molecular Microbiology* **54**, 855-862 (2004).

73. J. Kazmierczak Mark, M. Wiedmann, J. Boor Kathryn, Alternative Sigma Factors and Their Roles in Bacterial Virulence. *Microbiology and Molecular Biology Reviews* **69**, 527-543 (2005).

74. K. Nosho *et al.*, cAMP-CRP acts as a key regulator for the viable but non-culturable state in Escherichia coli. *Microbiology* **164**, 410-419 (2018).

75. K. Trunk *et al.*, Anaerobic adaptation in Pseudomonas aeruginosa: definition of the Anr and Dnr regulons. *Environmental Microbiology* **12**, 1719-1733 (2010).

Chapter 2 Measurement of Phenazine-1-carboxamide-Mediated Maintenance Metabolism Using High-Throughput Electrochemical System

Author Contributions and Publication Note

The work presented in this chapter was conducted as part of a collaborative study with Dr. John Ciemniecki and colleagues. My contributions included performing high-throughput electrochemical assays using a 96-well potentiostat platform to quantify phenazine-1-carboxamide (PCN)-mediated extracellular electron transfer and assess cell survival under anaerobic conditions. I also integrated total charge measurements to support the calculation of PCN oxidation rate and cell-specific metabolic rates. In addition, I conducted scanning electron microscopy (SEM) to evaluate electrode colonization and carried out cell concentration experiments to examine the impact of biomass on redox cycling efficiency.

Portions of this work have been published in:

Ciemniecki, J. A., Ho, C. L., Horak, R. D., Okamoto, A., & Newman, D. K. (2024). Mechanistic study of a low-power bacterial maintenance state using high-throughput electrochemistry. *Cell*, *187*(24), 6882-6895.

https://doi.org/10.1016/j.cell.2024.09.042

2.1 Introduction

While cells in natural and clinical settings often reside in metabolically attenuated states—such as the hypoxic core of biofilms—how much energy required for maintaining viability without growth are still not well defined. Traditional estimates of "maintenance metabolism" rely on extrapolations from slow-growing continuous culture studies (1-3), which tend to significantly overstate the actual metabolic needs of non-growing cells. Moreover, metabolic rate estimates derived from environmental measurements often depend on indirect assumptions about cell activity and population structure, making direct quantification difficult (4). To address this, robust laboratory models that enable precise measurement of metabolic activity under near-zero growth are urgently needed.

Pseudomonas aeruginosa produces phenazines such as pyocyanin, phenazine-1-carboxylic acid, and phenazine-1-carboxamide (PCN), which are redox-active metabolites that function as extracellular electron shuttles, facilitating anaerobic survival metabolism (5, 6). This non-growth metabolic state supports cell viability by enabling substrate-level phosphorylation and limited ATP generation (6). Because this process requires redox balancing through the reduction of exogenous oxidants, it is referred to as facilitated fermentation (7). Given that the phenazine-mediated anaerobic survival mechanism supports viability in the absence of growth, we hypothesized that its rate may reflect the minimal metabolic flux required for cellular maintenance under energy-limited conditions. Accordingly, we used this mechanism as a quantitative framework to measure the metabolic flux that powers maintenance metabolism. Among these phenazines, PCN is the most abundant in the anoxic interior of biofilms and possesses the lowest redox potential, making it an ideal candidate for probing the lower bounds of bacterial metabolic activity (8, 9).

My collaborator, Dr. John Ciemniecki, used pulse-chase labeling with the fluorescent cell wall stain 7-hydroxycoumarincarbonylamino-D-alanine (HADA) (10) to show that cells remain metabolically active without undergoing division or death, distinguishing this condition from slow growth and defining it as a maintenance state.

Building on this observation, experiments using low-throughput electrochemical systems confirmed that PCN-mediated extracellular electron transfer (EET) supports non-growth survival under anaerobic conditions. The metabolic rate (1.6×10^3 $e^- s^{-1}$ $cell^{-1}$ at 25˚C) measured under these conditions falls well below the average basal metabolic rate reported across all life forms, confirming that facilitated fermentation enables *P. aeruginosa* to sustain viability in an exceptionally low-power state.

Based on these findings, we sought to quantitatively define the metabolic rate required to maintain this state and to determine whether cells operate near their minimum energy threshold. In this chapter, I utilized a high-throughput 96-well electrochemical system to measure PCN-mediated metabolic activity across a wide concentration range. By integrating current production over time and normalizing to viable cell counts, I calculated the cell-specific metabolic rate required to support anaerobic maintenance. These experiments revealed that PCN cycling enables *P. aeruginosa* to survive at one of the lowest known metabolic rates. This work not only established a quantitative framework for analyzing low-power metabolism, but also provided a platform for future mechanistic studies of survival under energy-limited conditions.

2.2 Results

2.2.1 Leveraging a high-throughput electrochemical platform facilitates systematic investigation of non-growth metabolism.

In all experiments, a *Δphz* strain incapable of endogenous phenazine production was used, allowing precise control over PCN concentration and eliminated confounding effects from endogenous phenazine production (5). To overcome the low-throughput nature and operational complexity from large-scale electrochemical reactors, we adopted a 96-well electrochemical platform (11), which enables parallel, independent potentiostatic measurements with streamlined operation (Figure 1A). The increased throughput of the 96-well format allowed us to test a wider range of PCN concentrations (Figure 1B). To assess whether PCN-dependent anaerobic survival assays could be reliably translated from the large reactor to the high-throughput format, we directly compared survival outcomes under matched conditions. The current profile and survival data from the large reactor were reported in the main paper and are therefore not shown in this chapter. Cells in the 96-well platform exhibited significantly enhanced survival in the presence of PCN (Figure 1C). However, we observed that cells in the high-throughput setup died more rapidly after day 5 regardless of PCN concentration, whereas survival in the large reactor was maintained until day 7. Consequently, all experiments using the 96-well platform were terminated at this time point. Although the absolute survival at 75 μM PCN was approximately two-fold lower in the high-throughput system compared to the large reactor, the difference amounted to less than a one-log reduction in viability. These results suggest that the miniaturized platform reliably reproduces the core physiological outcomes of PCN-mediated anaerobic survival and can serve as a robust alternative for quantifying maintenance metabolism across broader experimental conditions.

2.2.2 Attenuation of Cellular PCN Reduction Reveals a Metabolic Plateau Near the Maintenance Threshold

To assess how PCN concentration influences metabolic output, we first integrated current from days 1 to 5, after the initial spike had stabilized and averaged it overtime to obtain electron flux (electrons sec^{-1}). We found that the PCN-mediated electron flux plateaued at concentrations above 75 μM (Figure 2A), raising the question: what factor limits redox cycling at higher substrate availability? One possible explanation was the formation of a biofilm on the electrode surface, which could impede the diffusion of reduced PCN to the electrode. However, scanning electron microscopy revealed only a sparse monolayer of cells and no substantial biofilm formation, ruling out electrode fouling as the limiting factor (Figure 3A). To further test whether the limitation originated from the cells themselves, Δ*phz* cells from multiple replicate wells incubated with 375 μM PCN were pooled, pelleted, and resuspended in a small volume of supernatant collected from parallel wells under identical conditions. The resulting concentrated suspension was then added to wells already containing Δ*phz* cells and 375 μM PCN, thereby approximately doubling the total cell concentration. This intervention resulted in a sustained 1.5-fold increase in current over 12 hours (Figure 3B), confirming that the electrode was not rate-limiting. These results suggest that the observed plateau in redox activity is attributable to a cellular limitation in PCN reduction capacity under prolonged anaerobic conditions.

We then normalized PCN-mediated electron flux to the geometric mean of viable cell counts as the cell-specific metabolic rate ($e^- s^{-1} cell^{-1}$) (Figure 2B). Notably, the measured rate remained steady at ~3.0×10^3 $e^- s^{-1} cell^{-1}$ at 25 °C (95% CI: 1.6–5.4 $\times 10^3$), closely matching values observed in the large reactor system, suggesting that PCN-facilitated fermentation supports the minimal energy required for maintenance

metabolism. Because PCN concentration limit survival below 75 μM, this consistent metabolic rate suggests that PCN availability governs survival by controlling access to maintenance-level energy flux. Thus, we conclude that culturable cells are operating near their minimum energy threshold for anaerobic maintenance under these conditions.

2.3 Discussion

Bacteria are capable of long-term survival in energy-limited states caused by nutrient or oxygen scarcity, without undergoing growth (12, 13). Such low-energy states are not only characteristic of most natural microbial habitats but also represent a dominant physiological condition in chronic infection settings (14, 15). A detailed understanding of the molecular strategies that enable viability during low-power metabolic states remains critical for improving strategies to treat persistent infections. However, technical limitations have long impeded efforts to study this physiological state systematically.

In this work, we demonstrated that a 96-well electrochemical system overcomes previous limitations by enabling direct, parallel measurements of *P. aeruginosa* metabolic activity under energy-limited, anaerobic conditions across multiple experimental parameters. Using PCN as a redox-active molecule that facilitated EET, we calculated the metabolic rate by integrating the electrochemical current and normalizing to viable cell counts. Our measurements revealed that PCN-driven metabolism sustains cells at an exceptionally low power output—approximately 1,000-fold lower than that of actively growing cells, and roughly 10-fold slower than the average basal metabolic rate across all life forms, based on lab-measured microbial rates compiled by Hoehler et al (3). While we observed exceptionally low metabolic rates, these may not represent the absolute minimum required for survival. Because the

conditions tested in this study were relatively uniform—such as fixed buffer composition, temperature, and pH—as well as potential influences from genetic factors, further investigations will be necessary to determine how environmental and genetic variables shape or constrain the lower limits of maintenance metabolism.

In addition, our data indicate that under maintenance state, the cellular capacity to reduce PCN becomes saturated, particularly at higher PCN concentrations. This observation challenges the prevailing notion that bacteria always maximize metabolic output to optimize fitness. The physiological basis of this downshift in electron flux remains to be elucidated, especially given that the tested PCN concentrations fall within the physiological range found in the anoxic cores of *P. aeruginosa* biofilms (8).

Although the high-throughput electrochemical system enables quantitative analysis of *P. aeruginosa* metabolism under a maintenance state, this anaerobic survival state is not indefinitely stable. In our experiments, cell viability began to decline after day 5, and the overall survival rate was lower than that observed in the large-scale reactor. These findings suggest that cells were operating within a quasi-steady state rather than a truly stable maintenance phase. Moreover, the system models planktonic cells rather than the biofilm-associated lifestyle that predominates in natural and clinical environments. While stationary-phase planktonic cells may exhibit metabolic traits reminiscent of biofilm-associated populations (5, 16), important physiological distinctions between the two states remain (17). Thus, this platform may not fully recapitulate the maintenance state that occurs in vivo. Nevertheless, compared to conventional laboratory cultivation systems—such as chemostats or batch cultures with slow growth—the physiological state captured here more closely resembles the energy-limited survival modes observed in nature.

Together, our results highlight the value of a high-throughput electrochemical platform for probing the physiological limits of bacterial survival under energy-limited,

anaerobic conditions. By quantifying phenazine-mediated electron transfer rates at the single-cell level, we established that *P. aeruginosa* can sustain viability at one of the lowest metabolic rates ever measured. Although this system represents a simplified, planktonic model that may not fully capture the complexity of biofilm-associated maintenance states, it nevertheless provides a scalable and tractable framework for future investigations into non-growth metabolism.

2.4 Methods and materials

Anaerobic survival assay using 96-well electrochemical potentiostat

Starter cultures were harvested by centrifugation and washed twice with minimal medium (MM), which consisted of 100 mM MOPS buffer (pH 7.2, adjusted with 5 N NaOH), 43 mM NaCl, 93 mM NH_4Cl, 3.7 mM KH_2PO_4, and 1 mM $MgSO_4$. The cells were then resuspended to an OD_{600} of 75 and transferred into a Coy anaerobic chamber maintained at 33 °C under a hydrogen-rich atmosphere (2–3% H_2).

A custom 96-well electrochemical plate equipped with screen-printed electrodes—comprising a carbon working electrode, carbon counter electrode, and an Ag/AgCl reference electrode—was prepared (11). Each well received 10 µL of the cell suspension (diluted beforehand to $OD_{500} = 15$ using N_2-sparged MM) along with 190 µL of fresh N_2-sparged MM supplemented with 20 mM D-glucose, 3.6 µM $FeSO_4$, and PCN at final concentrations of 7.5, 37.5, 75, or 375 µM (dissolved in 2.5% DMSO). To prevent evaporation during incubation, the plate was sealed with a combination of a slit-seal cover (BioChromato, RSS-S96-10-S) and an aluminum adhesive film (DiversifiedBiotech, ALUM-1000). Electrochemical incubation was performed at 33 °C without shaking using a custom-built 96-channel potentiostat, with each well's working electrode poised at 0 mV versus Ag/AgCl.

Sampling was carried out on days 1, 3, and 5. At each time point, the aluminum seal was removed, and the cultures in each well were gently mixed by pipetting 150 μL at least ten times. A 10 μL aliquot was then withdrawn from each well for colony-forming unit (CFU) quantification. After sampling, wells were resealed with fresh aluminum films and returned to the potentiostat for continued incubation. All plasticware used inside the anaerobic chamber was pre-degassed for a minimum of three days prior to the experiment.

Colony Forming Unit (CFU) Assay

Cell suspensions were serially diluted in phosphate-buffered saline (PBS) prior to plating. Dilution series were prepared to span 5 to 6 orders of magnitude, and 5 μL aliquots from each dilution were spotted onto LB agar plates. Plates were incubated overnight at 37 °C to allow colony development. For quantification, the highest dilution spot yielding at least 10 colonies was selected. All procedures—including dilution, plating, and incubation—were conducted under aerobic conditions.

Scanning Electron Microscopy (SEM) Sample Preparation

To assess potential biofilm formation on electrode surfaces under varying phenazine concentrations, SEM samples were prepared following the procedure below. Electrochemical experiments were first conducted under anaerobic conditions using a 96-well potentiostat system, with PCN supplied at final concentrations of 0, 7.5, 75, 375, and 750 μM. Cells were incubated for 2 days without agitation. After incubation, each well was pipetted 30 times to dislodge loosely associated cells, and the resulting suspensions were collected. To fix the cells, each sample was mixed with 2.5% glutaraldehyde (prepared from 25% stock; Wako, Japan) in 0.1 M phosphate-buffered saline (PBS) and allowed to stand at 25 °C for 10 minutes. After fixation,

glutaraldehyde was gently removed, and samples were rinsed three times with 0.1 M PBS without pipetting.

Samples were then dehydrated using an ethanol gradient (25%, 50%, 75%, and 99.5%), with each step lasting 5 minutes. The dehydrated samples were subsequently treated twice with 100% tert-butanol (Wako, Japan) for 5 minutes each. The screen-printed electrode plates were disassembled, and individual electrodes were transferred into 35 mm cell culture dishes containing 100% tert-butanol, followed by vacuum freeze-drying at 0 °C for 2 days. Dried samples were sputter-coated with platinum under vacuum for 30 seconds, mounted onto SEM stubs using carbon tape, and imaged using a Keyence VE-9800 scanning electron microscope (Keyence, Osaka, Japan) at 10 or 20 kV accelerating voltage.

Calculation of Cell-Specific Metabolic Rate

Metabolic rates were calculated following the approach described by Dr. John Ciemniecki (ref). To estimate the average PCN reduction rate using the 96-well electrochemical platform, transient current fluctuations were identified and excluded. Specifically, a 3-hour period following each removal and reinsertion of the plate into the potentiostat was omitted, as these intervals exhibited sharp, non-biological current spikes. The remaining stable current data between day 1 and day 5 were integrated to yield total charge (nA*hr), which was subsequently converted to the number of electrons transferred using standard conversion factors. This value was then normalized to the effective measurement duration (90 hours) and to the geometric mean of viable cell counts (CFU per 0.2 mL) over the same period, resulting in cell-specific metabolic rates expressed in units of electrons per second per cell ($e^- s^{-1} cell^{-1}$).

2.5 Figures

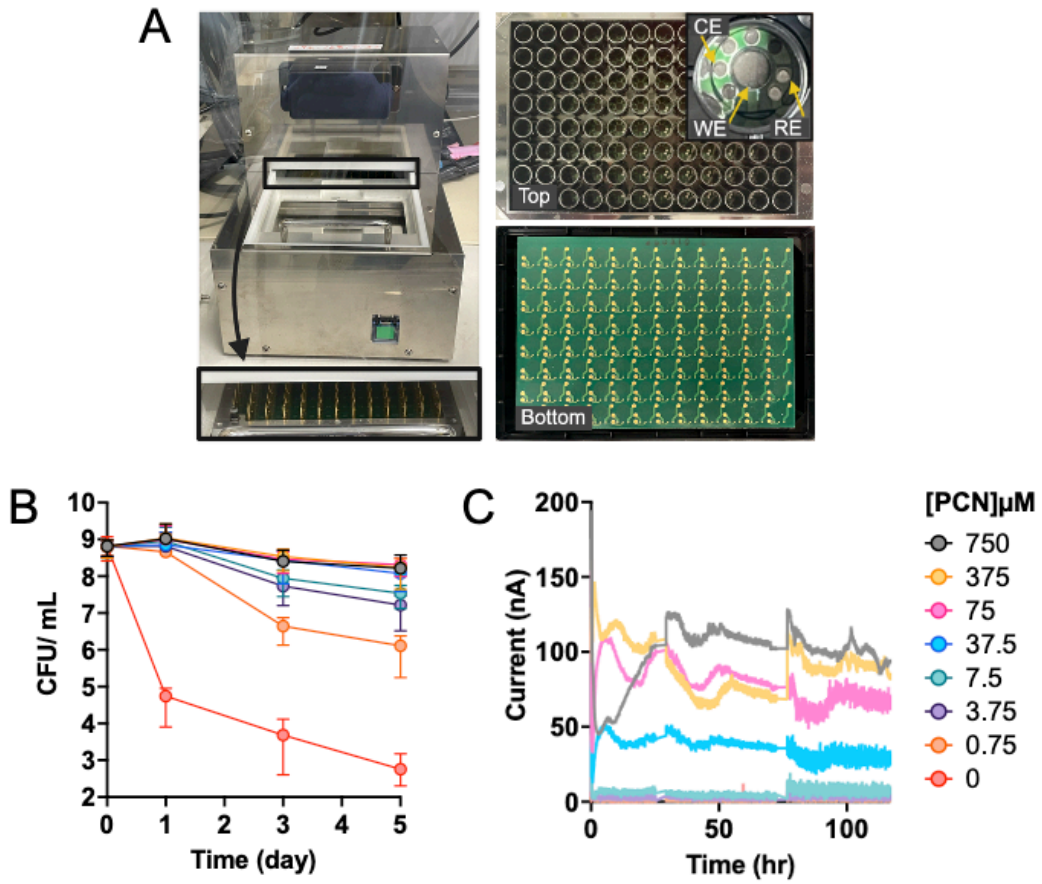


Figure 1. A high-throughput electrochemical platform enables multiplexed measurement of phenazine-dependent anaerobic survival.

(A) Schematic of the 96-well potentiostat system used in this study. Each well contains an independent working electrode (WE), counter electrode (CE), and reference electrode (RE). Conductive pads on the plate bottom align with potentiostat pins to establish electrical contact. (B) Anaerobic survival of the *Δphz* strain grown in glucose minimal medium supplemented with varying concentrations of PCN, in the presence of an applied oxidizing potential. (C) Average current produced by *Δphz* cultures over 5 days of anaerobic electrochemical incubation. Data represent the mean of five biological replicates.

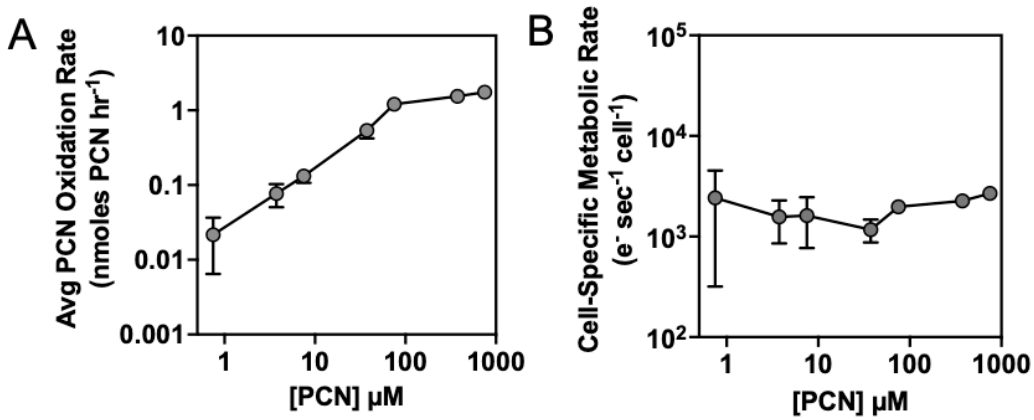


Figure 2. Metabolic Attenuation of PCN Reduction Highlights a Threshold Near the Energy Minimum for Survival.

(A) The average PCN oxidation rate at the working electrode surface was calculated during days 1–5 of anaerobic electrochemical incubation with *Δphz* cells. Data represent the mean values from at least four biological replicates, with error bars indicating the 95% confidence interval. (B) Cell-specific metabolic rates of *Δphz* cells were calculated over days 1–5 across a range of PCN concentrations. Each data point represents current normalized to the geometric mean of CFU counts from at least four biological replicates, with error bars indicating the standard deviation.

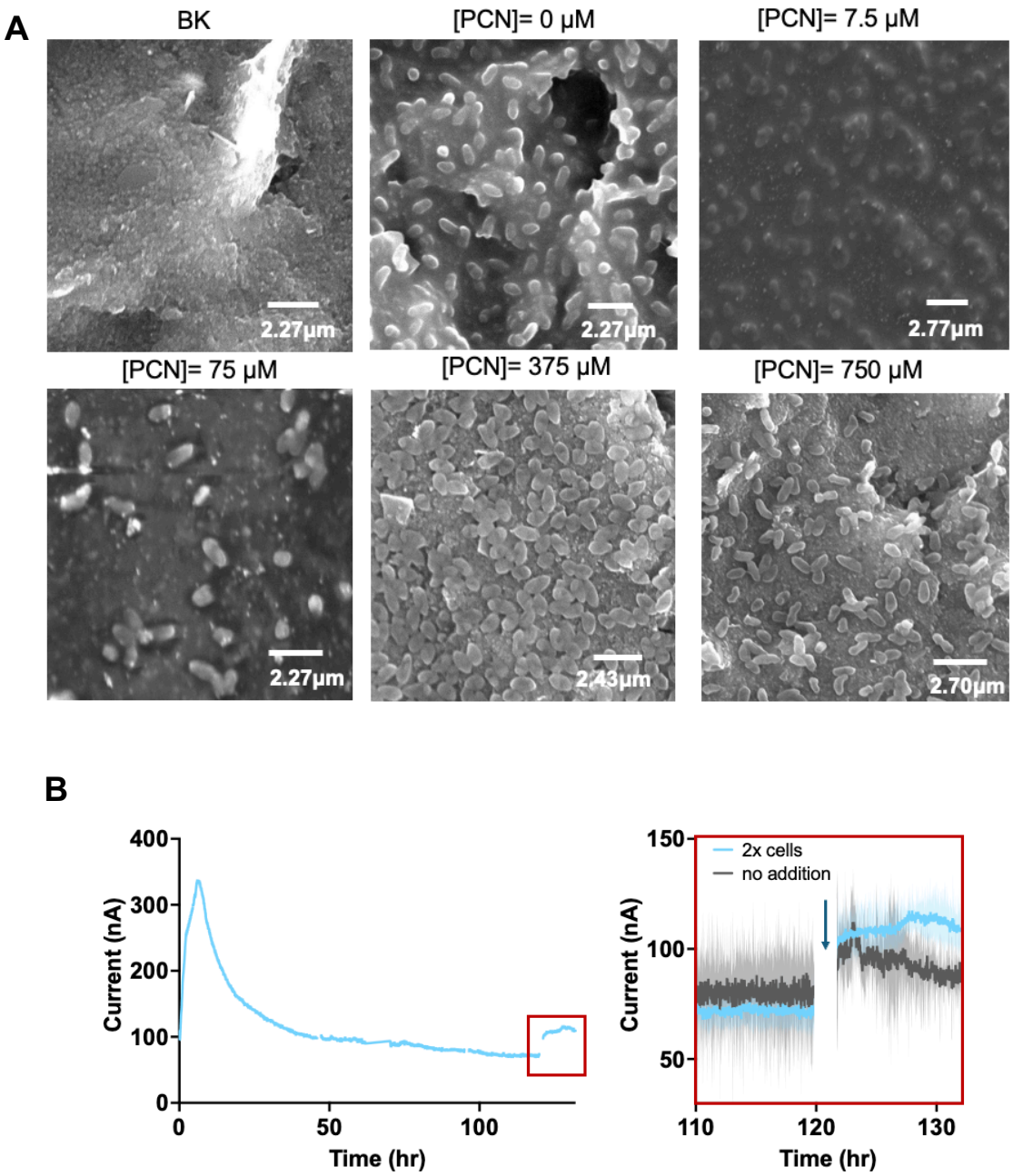


Figure 3. Evidence that the electrode is not limiting current at high PCN concentrations.

(A) Scanning electron microscopy images of the working electrode surface after 2 days of anaerobic electrochemical incubation with Δphz cells across a range of PCN concentrations. (B) Average current produced by Δphz cells in the presence of 375 µM PCN. Inset: on day 5, cells from replicate wells were pooled, concentrated, and added to the wells to approximately double the cell density. A corresponding increase in current was observed. Shaded areas represent 95% confidence intervals across four biological replicates.

2.6 References

1. P. van Bodegom, Microbial Maintenance: A Critical Review on Its Quantification. *Microbial Ecology* **53**, 513-523 (2007).
2. E. Biselli, S. J. Schink, U. Gerland, Slower growth of Escherichia coli leads to longer survival in carbon starvation due to a decrease in the maintenance rate. *Molecular Systems Biology* **16**, e9478 (2020).
3. T. M. Hoehler *et al.*, The metabolic rate of the biosphere and its components. *Proceedings of the National Academy of Sciences* **120**, e2303764120 (2023).
4. O. Braissant, M. Astasov-Frauenhoffer, T. Waltimo, G. Bonkat, A Review of Methods to Determine Viability, Vitality, and Metabolic Rates in Microbiology. *Frontiers in Microbiology* **Volume 11 - 2020** (2020).
5. Y. Wang, E. Kern Suzanne, K. Newman Dianne, Endogenous Phenazine Antibiotics Promote Anaerobic Survival of Pseudomonas aeruginosa via Extracellular Electron Transfer. *Journal of Bacteriology* **192**, 365-369 (2010).
6. N. R. Glasser, S. E. Kern, D. K. Newman, Phenazine redox cycling enhances anaerobic survival in Pseudomonas aeruginosa by facilitating generation of ATP and a proton-motive force. *Molecular Microbiology* **92**, 399-412 (2014).
7. J. A. Ciemniecki, C.-L. Ho, R. D. Horak, A. Okamoto, D. K. Newman, Mechanistic study of a low-power bacterial maintenance state using high-throughput electrochemistry. *Cell* **187**, 6882-6895.e6888 (2024).
8. S. H. Saunders *et al.*, Extracellular DNA Promotes Efficient Extracellular Electron Transfer by Pyocyanin in *Pseudomonas aeruginosa* Biofilms. *Cell* **182**, 919-932.e919 (2020).
9. J. A. Ciemniecki, D. K. Newman, NADH dehydrogenases are the predominant phenazine reductases in the electron transport chain of Pseudomonas aeruginosa. *Molecular Microbiology* **119**, 560-573 (2023).
10. A. A. Yakhnina, H. R. McManus, T. G. Bernhardt, The cell wall amidase AmiB is essential for Pseudomonas aeruginosa cell division, drug resistance and viability. *Molecular Microbiology* **97**, 957-973 (2015).
11. W. Miran, W. Huang, X. Long, G. Imamura, A. Okamoto, Multivariate landscapes constructed by Bayesian estimation over five hundred microbial electrochemical time profiles. *Patterns* **3** (2022).
12. J. M. Gonzalez, B. Aranda, Microbial Growth under Limiting Conditions-Future Perspectives. http://dx.doi.org/10.3390/microorganisms11071641.

13. M. A. Lever *et al.*, Life under extreme energy limitation: a synthesis of laboratory- and field-based investigations. *FEMS Microbiology Reviews* **39**, 688-728 (2015).

14. P. S. Stewart, M. J. Franklin, Physiological heterogeneity in biofilms. *Nature Reviews Microbiology* **6**, 199-210 (2008).

15. R. La Rosa, H. K. Johansen, S. Molin, Adapting to the Airways: Metabolic Requirements of Pseudomonas aeruginosa during the Infection of Cystic Fibrosis Patients. http://dx.doi.org/10.3390/metabo9100234.

16. M. Hentzer, L. Eberl, M. Givskov, Transcriptome analysis of Pseudomonas aeruginosa biofilm development: anaerobic respiration and iron limitation. *Biofilms* **2**, 37-61 (2005).

17. L. H. Stipetic *et al.*, A novel metabolomic approach used for the comparison of Staphylococcus aureus planktonic cells and biofilm samples. *Metabolomics* **12**, 75 (2016).

Chapter 3 Efflux pump activity limits metabolism during an anaerobic maintenance state powered by phenazines redox cycling

3.1 Introduction

Multidrug efflux pumps are widely regarded as a key mechanism of bacterial antibiotic resistance, actively exporting toxic compounds and thereby promoting survival in metabolically active cells (1, 2). While much of our current understanding stems from studies conducted under nutrient- and oxygen-rich conditions that support robust energy generation (3, 4), many natural environments with nutrient or oxygen limitation—such as biofilm interiors, sediments, or chronic infection sites —are characterized by energy-limited conditions (5-8). In these settings, cells often enter a low-energy maintenance state, in which metabolic activity, proton motive force (PMF), and ATP synthesis are markedly reduced, leaving cells in a non-growing but physiologically active state (9).

Resistance-Nodulation-Division (RND) type efflux pumps are PMF-driven and thus impose an energetic cost on cells (10, 11). One might therefore expect that, in energy-limited states already associated with drug tolerance (12, 13), bacteria would have little need—or capacity—to sustain costly efflux. Yet multiple lines of evidence indicate that efflux remains important in energy-limited conditions, including facilitating adaptation to metabolic stress and stabilizing biofilm physiology (14). This tension raises a key question: under energy limitation, is efflux primarily a detoxification valve, or can it also serve as a bioenergetic control point that shapes antibiotic responses?

Growing evidence links efflux directly to redox cycling by exporting exogenous or endogenous electron shuttles (ES) (15, 16) . ES enter cells, are reduced by intracellular

metabolism (for example via NADH-dependent reactions (17)), and are subsequently re-oxidized at extracellular electron acceptors; by cycling between these reduced and oxidized states, they mediate anaerobic electron transfer and support respiration-coupled ATP generation. Deleting efflux components reduces ES export across diverse bacterial species (15, 18), and recent work in *E. coli* suggests that AcrAB–TolC can become a rate-limiting step for respiration under anaerobic conditions (refs). These observations motivate the hypothesis that, beyond detoxification, efflux governs ES-mediated redox cycling to maintain metabolic activity in energy-limited states.

To test this hypothesis in a clinically relevant context, we leveraged a high-throughput electrochemical platform that quantifies metabolic flux in non-growing *Pseudomonas aeruginosa* under a defined maintenance state (9). *P. aeruginosa* produces phenazines—redox-active metabolites that support EET and viability in energy-limited environments (13). Among phenazines, phenazine-1-carboxamide (PCN) accumulates at high concentrations within the biofilm matrix, providing a tractable probe of maintenance metabolism (16, 17). In our assay, the measured current reports the net rate of electron-shuttle (ES) turnover, while varying PCN concentration shifts rate control between ES kinetics and upstream cellular metabolism that provides reducing equivalents such as NADH (17). This relationship allows us to identify the role of efflux in ES turnover and to track how efflux reshapes metabolic activity under a low-energy maintenance state .

Here, we evaluated the role of RND-type efflux pumps in non-growing *P. aeruginosa* by genetically increasing efflux capacity (e.g., MexEF–OprN, MexGHI–OpmD, both implicated in phenazine export (3, 18) and modulate shuttle availability to determine how efflux controls ES and metabolism in maintenance physiology. We quantified how efflux overexpression alters drug tolerance in a low-energy maintenance state, and we resolved its impact on electron shuttling, cellular metabolic

activity, and membrane energetics by varying PCN concentration and measuring PMF-linked readouts—membrane potential. In addition, our results reveal that efflux-driven export of ESs couples directly to metabolic compensation under energy limitation, thereby regulating antibiotic susceptibility in ways not captured under energy-replete conditions. This work links microbial bioenergetics to antimicrobial response and identifies energy-dependent export as a lever to modulate drug susceptibility in biofilms.

3.2 Results

3.2.1 Adaptation and maintenance phases reveal distinct metabolic controls in anaerobic PCN-mediated metabolism.

We revisited the previously reported biphasic relationship between PCN concentration and current output (9). In this assay, a maintenance physiology was established in *Pseudomonas aeruginosa* PA14 by incubating cells anaerobically at a poised electrode (0 V vs. Ag/AgCl) with glucose. Current and survival were measured after 5 days across a range of PCN concentrations using a phenazine-deficient mutant (*Δphz*), which enables defined PCN supplementation (19, 20). Because PCN-driven redox cycling spans two physiologically distinct regimes from the adaptation (day 0–1) to maintenance (day 1–5) phases, we analyzed the two phases separately (Figure 1A). Consistent with prior work, current increased proportionally with PCN in the low-concentration regime (< ~75 μM) but approached a plateau at higher concentrations (Figure 1B). This biphasic pattern was observed in both adaptation and maintenance states. However, when current was normalized by the geometric mean survival to obtain the cell-specific metabolic rate (electrons s^{-1} $cell^{-1}$), the two phases diverged (Figure 1C-D). During adaptation, the cell-specific metabolic rate remained the curve similar with current output, preserving the kinetic response to increasing PCN in the low-

concentration regime. In contrast, during maintenance, the metabolic rate became independent of PCN concentration, indicating that long-term anaerobic metabolism is constrained not by substrate availability but by the energetic demands of survival under low-energy conditions. In this regime, the key question shifts from substrate-driven kinetics to how baseline maintenance metabolism is sustained over long-term anaerobic survival. Because efflux pumps can contribute both to phenazine export (18, 21) and to cellular energy expenditure (10, 22), their impact is expected to differ across these physiological states. Therefore, separating these phases is necessary to test whether efflux pumps act as kinetic determinants of PCN redox cycling and whether they instead impose energetic liabilities that influence long-term survival.

3.2.2 Efflux pumps coupled with the metabolic activity at high PCN concentration under adaption phase

To test whether efflux pump activity contributes to metabolism during the adaptation phase, we first compared the phenazine-deficient strain (*Δphz*) with Δ*phz*Δ*mexS*, in which loss of mexS upregulates the MexEF–OprN RND efflux system (Figure 2A) (3, 23, 24). We hypothesized that if efflux pump activity constitutes a rate-limiting step for PCN-driven metabolism during the adaptation phase, then the *ΔmexS* mutation should increase the cell-specific metabolic rate. Current production of *ΔphzΔmexS* was identical to *Δphz* across 3.75–75 μM PCN, a range in which the concentration–response relationship remained linear (Figure 2B). This indicates that increased efflux pump activity does not influence metabolism when metabolic flux is still proportional to substrate availability. However, at higher PCN concentrations (150–375 μM), where current approaches a plateau, *ΔphzΔmexS* exhibited a gradual increase in current relative to *Δphz* (Figure 2B). Although the response was not linear, this enhancement suggests that under plateau conditions—when the system is no longer

substrate-limited—efflux capacity begins to constrain metabolism and may therefore become a potentially rate-limiting factor during the adaptation phase at high PCN concentrations.

To further verify the contribution of efflux pump to enhance metabolic activity at high PCN concentrations, we used a Δ*phz* attTn7::*Para:mexGHI-opmD* Gm^R strain (hereafter referred to as the Δ*phz Para:mexGHI* strain), in which the *mexGHI-opmD* operon is inducible by arabinose. Induction was performed at 375 μM PCN, a concentration at which efflux-dependent effects are expected to be most apparent. Exposure of the *Δphz Para:mexGHI* strain to 20 mM arabinose resulted in a current increase comparable to that observed for the *ΔphzΔmexS* mutant (Figure 2C). This inducible system allowed us to isolate pump-specific effects from the broader regulatory changes in the mexS mutant. Increasing arabinose concentrations led to elevated mexG expression levels, confirming tunable control of efflux pump expression (Figure 2D). After verifying that arabinose addition alone did not significantly affect cell survival (Figure. S1A) and current production in the Δ*phz* background (Figure. S1B), we plotted *mexG* expression levels against current in the inducible strain (Figure 2E). This analysis revealed a strong positive linear correlation, indicating that efflux pump expression directly influences metabolic activity. To exclude the possibility that enhanced current resulted from the metabolic burden of protein overexpression, we tested the Δ*phz* AttB::*mNeonGreen* strain, which strongly expresses a fluorescent reporter (Figure 2C). Current output in this strain remained comparable to Δ*phz*, indicating that enhanced metabolic activity is specifically due to efflux pump activity rather than protein overexpression.

3.2.3 The Energetic Cost of Maintaining PMF Shapes Baseline Metabolism During the Maintenance State

Efflux pumps are known to impose a metabolic burden by consuming the proton motive force (PMF) (10, 11). We therefore hypothesized that efflux pump overexpression may further elevate metabolic rate during the maintenance phase by increasing PMF consumption (Figure 3A). To test this, we quantified the cell-specific metabolic rate of Δ*phz* and Δ*phz*Δ*mexS* strains by normalizing current output to CFU counts from days 1–5 in PCN-mediated anaerobic survival assays. Although total current production was similar between the two strains at PCN concentration of 7.5 μM to 375 μM (Figure 3B), the markedly lower survival of Δ*phz*Δ*mexS* by day 5 resulted in a significantly higher cell-specific metabolic rate (Figure 3C). At 375 μM PCN, Δ*phz*Δ*mexS* exhibited a metabolic rate of 1.3×10^4 electrons s^{-1} $cell^{-1}$ at 25 ˚C (95% CI: 1.1×10^4 to 1.4×10^4), which was 3.3-fold higher than that of Δ*phz* (3.9×10^3 electrons s^{-1} $cell^{-1}$; 95% CI: 3.6×10^3 to 4.2×10^3) (Figure 3D). These data are consistent with the interpretation that elevated PMF consumption in the mexS mutant increases the energetic demand of maintenance metabolism, requiring cells to accelerate electron flux to compensate for heightened PMF dissipation.

To investigate whether the increased metabolic rate arises as a compensatory response to PMF dissipation, we treated cells with the protonophore CCCP (50 μM) on day 1 of the anaerobic survival assay. Although overall cell survival was one to two magnitudes reduced following CCCP treatment, current production only slightly lower from days 1 to 5 (Figure 3B-C). As shown in Figure. S2A, this sustained current was only observed in the presence of cells, indicating that it reflects ongoing metabolism rather than abiotic factors, even under the energetic stress of PMF dissipation. Metabolic rate analysis revealed that Δ*phz* treated with CCCP exhibited a rate of 1.3×10^5 electrons s^{-1} $cell^{-1}$ at 25 ˚C (95% CI: 1.0×10^5 to 1.6×10^5), representing a 34-fold increase

compared to untreated Δ*phz* (Figure 3D). To further assess intracellular energy levels, we quantified ATP concentration after 5 days of incubation (Figure. S2B). We found that ATP levels in Δ*phz* treated with CCCP and in Δ*phz*Δ*mexS* were 1.8×10^{-9} and 5.6×10^{-10} nmol cell^{-1}, respectively representing 4.7-fold and 1.5-fold increases relative to untreated Δ*phz* (3.8×10^{-10} nmol cell^{-1}). These findings indicate that PMF dissipation imposes a higher energetic burden, forcing cells to elevate their baseline metabolism during the maintenance state to compensate.

To ensure that CFU counts accurately reflected viable cell numbers without interference from viable but non-culturable (VBNC) cells, we performed fluorescence-based viability staining using SYTO 9 and propidium iodide (PI) on day 5 (25). Live cells were defined as those showing green fluorescence (SYTO 9), while dead cells showed red or overlapping green and red fluorescence (PI) (Figure. S3A). We quantified the ratio of live cells (green) to total cells (green + red) and found that this ratio closely matched the CFU-based survival measurements (Figure. S3*B*-*C*), indicating that the contribution of VBNC cells was minimal in our system, and that CFU counts reliably reflected true survival.

To further confirm the restoration of the proton motive force (PMF), we measured the membrane potential (ΔΨ) in Δ*phz*, Δ*phz*Δ*mexS*, and Δ*phz* treated with CCCP using the fluorescent dye 3,3′-diethyloxacarbocyanine iodide ($DiOC_2(3)$) (Figure 3E). This dye accumulates in cells in a ΔΨ-dependent manner, emitting green fluorescence at low concentrations. When ΔΨ is high, $DiOC_2(3)$ aggregates and shifts to red fluorescence. Thus, the ratio of red to green fluorescence serves as a semi-quantitative indicator of membrane potential, providing a basis for comparing ΔΨ across different conditions (26). At near-neutral extracellular pH, where intracellular pH is expected to be near neutral, ΔpH contributes minimally to the PMF, which is therefore dominated by ΔΨ (27, 28). PMF (Δ*p*) can be expressed as:

$$\Delta p = \Delta\Psi - (2.303 \times RT / F) \times \Delta pH$$

where ΔΨ is the membrane potential, R is the gas constant, T is the absolute temperature, and F is the Faraday constant.

To ensure that the $DiOC_2(3)$ assay reliably reflects changes in ΔΨ in our system, we included valinomycin treatment as a control. Valinomycin, a potassium ionophore known to hyperpolarize the membrane by promoting K^+ efflux (29, 30), produced the expected increase in red fluorescence, confirming that the $DiOC_2(3)$ signal quantitatively reports ΔΨ dynamics under our experimental conditions (Figure 3F). Importantly, membrane potential could still be further increased by valinomycin even after 5 days of incubation, indicating that this method remains applicable for monitoring ΔΨ under a prolonged low-energy maintenance state. When CCCP was added on day 1, the ΔΨ was slightly lower than that of Δ*phz* (Figure 3F). This reduced membrane potential was maintained until day 2 but began to recover by day 3, with ΔΨ even exceeding that of Δ*phz*, without signs of significant cell death as assessed by TODi-3 staining, which labels dead cells with red fluorescence (Figure. S4). By day 5, a further increase in ΔΨ was observed in the CCCP-treated Δ*phz*. However, the concomitant rise in TODi-3 fluorescence at this time point suggests that part of the $DiOC_2(3)$ signal may originate from dye accumulation in dead cells, potentially leading to overestimation of ΔΨ. The Δ*phz*Δ*mexS* strain also showed a slightly lower ΔΨ than Δ*phz* on day 1, but recovered to similar levels after day 2 (Figure 3F). Notably, the distribution of ΔΨ values was getting broader in Δ*phz*Δ*mexS* and the CCCP-treated Δ*phz* after day 2, indicating greater heterogeneity in PMF across the population. These results suggest that the PMF is gradually restored over time in both Δ*phz*Δ*mexS* and CCCP-treated Δ*phz*. This further supports the conclusion that both efflux pump overexpression and PMF dissipation can induce a compensatory increase in metabolic rate and ATP

production under energy-limited conditions, underscoring the importance of maintaining PMF for survival during a low-energy maintenance state.

3.2.4 Efflux pump overexpression do not increase antibiotic resistance under a low-energy maintenance state.

Although efflux pump overexpression can enhance antibiotic resistance under aerobic, energy-replete conditions, it also imposes a higher metabolic cost by increasing PMF consumption. In low-energy maintenance states, where metabolic activity is strongly reduced, we hypothesized that cells cannot generate sufficient energy to support the elevated PMF demand required for accelerated antibiotic efflux, and therefore fail to gain increased antibiotic resistance. To test this idea, cells were subjected to antibiotic challenge after 5 days of anaerobic incubation at a biofilm-relevant PCN concentration (375 μM) (Figure 4A) (20). We compared WT, Δ*phz*, and Δ*phz*Δ*mexS* strains. Under maintenance conditions, survival did not differ significantly between WT and *Δphz* across drugs (Figure 4B), consistent with prior reports (9). By contrast, Δ*phz*Δ*mexS* showed lower baseline survival even without antibiotics, yet exhibited no further decrease upon exposure to ciprofloxacin, tobramycin, gentamicin, or ceftazidime relative to Δ*phz* (Figure 4B). Because MexS loss constitutively activates MexEF-OprN, which increases PMF consumption through elevated efflux activity, the reduced survival is likely attributable to this additional metabolic burden. Complementation modestly increased sensitivity relative to *ΔphzΔmexS*, a difference plausibly attributable to plasmid maintenance costs; we therefore interpret the complementation phenotype conservatively (31) (Figure. S5). However, complementation of *mexS* under rhamnose induction restored resistance with the addition of ciprofloxacin, indicating that the decreased survival resulted from loss of *mexS* function rather than from unrelated background mutations or nonspecific effects.

These results demonstrate that efflux overexpression lose their advantage by enhancing antibiotic resistance in the maintenance state.

To distinguish energetic effects from substrate competition between antibiotics and PCN, we repeated assays under aerobic, energy-replete conditions. In an aerobic condition, Δ*phz*Δ*mexS* showed higher survival than Δ*phz* with ciprofloxacin but no advantage with aminoglycosides, matching canonical substrate specificity—MexEF–OprN exports fluoroquinolones but not aminoglycosides, which are primarily handled by MexXY–OprM (23, 32-34). Notably, we observed no significant reduction in survival following ceftazidime treatment under aerobic conditions, consistent with prior reports indicating that β-lactam antibiotics exert minimal bactericidal effects on stationary-phase cells due to halted cell-wall synthesis (35, 36). To determine whether the elevated metabolic rate of the mexS mutant is specific to PCN redox cycling or instead reflects a general, PCN-independent energetic burden, we measured oxygen consumption under aerobic conditions. *ΔphzΔmexS* displayed a higher cell-specific respiratory rate than *Δphz* even in the absence of PCN (Figure 4C, S6), indicating that efflux pump overexpression may enhance metabolism by imposing a basal proton influx, in agreement with previous studies (10, 11). Under aerobic, energy-replete conditions, this higher metabolic demand does not reduce survival. Instead, antibiotic resistance remains determined by efflux substrate specificity because ATP and PMF can be readily regenerated. In contrast, under anaerobic maintenance conditions—where energy supply is strongly limited—the basal energetic burden becomes detrimental, resulting in reduced survival. Together, these data indicate that in energy-replete settings, resistance is governed by efflux efficiency and substrate specificity, whereas in the low-energy maintenance state, efflux no longer regulates resistance and instead, differences in efflux activity mainly affect cells through their metabolic costs, which strongly shape survival outcomes.

3.3 Discussion

Efflux Pumps Function as Bioenergetic Regulators in a Low-Energy State

Low-energy metabolism in *Pseudomonas aeruginosa* is central to biofilm persistence and chronic infection (37, 38), yet the decisive control point that limits metabolic throughput has remained unclear. Here we identify multidrug efflux as that control point. By systematically varying PCN concentration and using current as a quantitative proxy for PCN-mediated metabolism (Figure. 2 and 3), we demonstrate that efflux pump activity constitutes the bottleneck that sets the pace of both adaptation and maintenance metabolism. Two lines of evidence support this conclusion. First, overexpressing efflux pumps (MexEF-OpmD or MexGHI–OpmD) increased the cell-specific metabolic rate (as read out by current) during the adaptation phase, and this increase scaled positively with inducer level, establishing a direct, quantitative link between efflux capacity and electron flux. Second, in the maintenance state, efflux pump overexpression exhibited a markedly elevated metabolic rate, reflecting the increased PMF consumption associated with high efflux activity. These results demonstrate that efflux pumps are not only detoxification valves but bioenergetic regulators that set the pace of life in biofilms.

Despite the PMF cost of running efflux pumps, efflux overexpression did not substantially shift the population-average $\Delta\Psi$ (Figure. 3) This apparent paradox is resolved by a bioenergetic compensation mechanism: cells increase ATP production and respiratory proton pumping to restore PMF while maintaining ES (Figure. 3A). In practical terms, efflux activity can modulate cell-specific flux without collapsing $\Delta\Psi$, consistent with a maintenance physiology that homeostatically preserves membrane energetics (39, 40). These findings recast efflux as a metabolic controller with two

coordinated roles. In anaerobic adaptation, once PCN concentration exceeds the range where transport scales with substrate availability, efflux pump activity becomes the limiting step for metabolic flux, producing the observed plateau. In contrast, during long-term maintenance, the primary consequence of efflux activity is PMF dissipation (10). The cell compensates for this energetic drain by increasing metabolic throughput to restore ΔΨ, leading to elevated ATP production. In this sense, efflux functions as a metabolic controller that constrains electron-shuttling flux in adaptation while imposing an energetic burden that elicits compensatory metabolism in maintenance. Such bioenergetics mechanism explains how *P. aeruginosa* drastically attenuated at high PCN concentrations and maintain the cell-specific metabolic rate under low-energy conditions. Give the broad conservation of RND efflux pump in bacteria, such mechanism could be ubiquitous in attenuating and controlling metabolism under energy-limited conditions.

This energetic interpretation also clarifies why efflux-mediated detoxification fails specifically in the long-term maintenance state, where PMF dissipation becomes the dominant consequence of efflux activity. While efflux pumps have traditionally been viewed as detoxification valves in energy-replete conditions by exporting antibiotics to reduce intracellular accumulation (1, 2), our study shows that under low-energy conditions they fail to perform this detoxification role and instead act as a PMF-consuming energetic burden (Figure. 4). We believe that survival defect associated with pump overexpression is not unique to MexEF. Under low-oxygen conditions, overexpression of other RND pumps—including MexAB, MexCD, and MexXY—has also been reported to cause pronounced growth defects (10).

Dissecting the rate-limiting step in PCN-mediated redox cycling under adaptation

Our adaptation-phase experiments showed that even within the plateau region, increasing efflux pump activity enhances metabolic flux (Figure. 2B). This

phenomenon can be explained by two mechanistic possibilities. One is that metabolism itself is rate-limiting: elevated basal proton influx from pump activity imposes an additional energetic burden, prompting cells to raise catabolic flux to restore PMF, thereby increasing the PCN reduction rate (10, 22). The alternative is that the electron-shuttling step is rate-limiting: pump overexpression accelerates PCN export, expanding the overall redox-cycling flux and consequently elevating current (18, 21). Distinguishing between these mechanisms is essential, as they represent fundamentally different modes of metabolic control. If metabolism is rate-limiting, cells actively tune their metabolic rate in response to PMF demand. In contrast, if PCN transport is rate-limiting, metabolic flux becomes constrained by the physicochemical properties of PCN—such as membrane permeability and pump affinity—rather than by intrinsic metabolic regulation (41, 42). These mechanistic differences could have important consequences for long-term viability under low-energy conditions, as the ability to sustain redox flux is closely tied to maintenance metabolism. Future experiments modulating membrane permeability should help resolve which process defines the rate-limiting step under energy-limited, anaerobic conditions.

Efflux-driven feedback promotes population robustness but reveals single-cell heterogeneity

We observed PMF heterogeneity in both Δ*phz*Δ*mexS* and Δ*phz* strains upon CCCP treatment (Figure. 3F), suggesting that the observed partial population cell death overtime in both conditions may result from insufficient PMF compensation within a subpopulation of cells (43, 44). Why does this heterogeneity arise? The most immediate potential explanation is the limited availability of PCN for electron shuttling (9). Theoretical calculations indicate that, at a cell density of 1×10^9 cells mL^{-1} ($\approx 2 \times 10^8$ cells in 200 μL), each cell transferring 1×10^5 $e^- s^{-1}$ under Δphz + CCCP conditions,

the total electron demand is ≈2×10^{13} $e^- s^{-1}$. At 375 μM PCN (7.5×10^{-8} mol; 4.5×10^{16} molecules), the solution can accept ≈9.0×10^{16} electrons (two per PCN)—more than sufficient to sustain the population's total electron flux. However, a fraction of PCN accumulating within the cell membrane may reduce the effective amount of PCN available for extracellular electron transfer (17). Additional system-level factors may also contribute. Because the assay is conducted in an undivided three-electrode cell, the counter electrode may compete with cells for oxidized PCN—whose midpoint potential is approximately –140 mV versus SHE at pH 7, compared with ≈ –410 mV for the H^+/H_2 couple—acting as a thermodynamically superior oxidant that is effectively present at a much higher concentration (45). In addition, the absence of stirring creates spatial gradients: only a subset of cells remains near the working electrode, whereas those positioned closer to the counter electrode have diminished access to the primary electron-accepting surface. Such geometric and mass-transport constraints likely amplify population-level heterogeneity. We will examine these electrode-associated effects in future work.

Another plausible explanation is related to ionic homeostasis at the single-cell level (46). Environmental ions provide numerous benefits to cells—for example, potassium and sodium gradients contribute to membrane potential (47, 48), magnesium and iron availability affect ATP synthase (49, 50) and redox enzymes (51, 52), and ammonium flux is coupled to proton homeostasis (53, 54) and amino acid availability (55, 56)—yet these parameters can vary across microenvironments or even among individual cells within the same culture. On the other hand, elevated ion concentrations can impose additional osmotic stress, requiring cells to expend more ATP to maintain plasmolysis (17, 57, 58). Beyond osmotic stress, high ionic loads can also perturb intracellular pH homeostasis (59), increased production of radicals (60), and mismetallation (61). These variations in ionic balance and energetic demand would lead to heterogeneous

capacities to maintain PMF and to perform energy-intensive processes, ultimately resulting in cell-to-cell variability in survival and metabolic output. Dissecting how PCN partitioning and ionic milieu shape single-cell energetics is an important next step.

Efflux–RAM coupling as a widespread physiological strategy for survival

Given that PCN cycling is highly sensitive to efflux capacity in our experiments, and that RND transporters such as MexGHI-OpmD are known to export other phenazines including 5-Me-PCA and PYO (18, 21), we propose that PCN may be exported through analogous pathways. Additional support for this possibility comes from the broader RND transporter family. In E. coli, the AcrAB-TolC system has been shown to efflux redox-active aromatic compounds such as PYO and basic blue 24 through allosteric (Hill-type) control [Fuji]. Although Hill-type behavior has not been experimentally demonstrated for MexGHI-OpmD in *P. aeruginosa*, the 55% sequence similarity between MexI and MexF and their conserved RND architecture suggest that such allosteric regulation raises the possibility that comparable regulatory features may exist (21). This view is further reinforced by the 30–40% sequence homology between MexEF-OprN and the AcrAB-TolC complex (62, 63), and by the structural resemblance between OprN and TolC, which share a similar gating mechanism despite differences in periplasmic entry domains that shape substrate specificity (64). Notably, both systems are capable of exporting overlapping substrates such as ciprofloxacin and levofloxacin (65), underscoring the functional versatility of RND efflux pumps. Taken together, these observations make efflux-mediated PCN export a plausible model, although direct experimental evidence will be required to identify the specific pump(s) involved.

Importantly, the link between efflux activity and the handling of redox-active metabolites is not restricted to phenazines. Many redox-active metabolites (RAMs),

including toxoflavin from *Burkholderia gladioli* (66, 67), actinorhodin from *Streptomyces coelicolor* (68, 69), tannic acid from plants (70), and humic acids from environments (15), are known to be exported by efflux pumps. Notably, actinorhodin and humic substances have been shown to promote bacterial survival under energy-limited conditions, potentially by serving as electron shuttles in EET pathways (71-74). These observations imply that efflux regulation of redox-active compounds may not be limited to phenazines. Together, these findings indicate that efflux pump–mediated control of RAM-driven redox cycling may represent a widespread physiological strategy for bacterial adaptation to energy-limited environments.

Limitations and outlook

Although this study provides mechanistic insight into efflux-mediated regulation of maintenance metabolism, undeniably, it remains limited to stationary-phase planktonic cultures. Stationary-phase planktonic cells share many physiological traits with biofilm cells (36, 75), yet differ in important respects, particularly in structural complexity. Future work should directly compare planktonic and biofilm systems to determine whether efflux influences antibiotic response and metabolism in the same way. In addition, we examined only a limited set of RAMs. Expanding to other self-produced and environmental RAMs will be important to test the generality of the mechanism we propose. Finally, our inferences about energetic loads and compensatory mechanisms are drawn from population-level current and membrane-potential measurements. Although multiple controls mitigate potential confounders, future studies using single-cell approaches—such as fluorescent reporters or microfluidics (76, 77)—will be essential to directly validate how efflux activity shapes bioenergetics within bacterial populations.

Conclusion

By identifies multidrug efflux as the bioenergetic control point that limits PCN-driven metabolism under anaerobic, energy-limited conditions—this study links export energetics to antibiotic response in a way that is invisible under energy-replete conditions. Efflux-driven feedback promotes robustness at the population level while revealing heterogeneity at the single-cell level, highlighting both the stabilizing and diversifying consequences of energetic control. Although our experiments focus on PCN, many redox-active metabolites (RAMs) can be exported by efflux pumps and assist bacterial survival under energy-limited conditions, the features revealed in this study collectively provide a mechanistic basis for context-dependent outcomes of antibiotics and support an evolutionary rationale for the broad conservation of efflux systems, which equip bacteria with tunable feedback mechanisms that enhance survival across fluctuating environments.

3.4 Material and methods

Microbial growth conditions and reagents

All *Pseudomonas aeruginosa* UCBPP-PA14 strains (Table S1) were taken from -80˚C glycerol stocks and plated on LB agar, where they were grown overnight at 37˚C. After incubation, the plates were stored at 4˚C and used within a week to start liquid cultures. For liquid cultures, initial inoculations were made in 7 mL of LB medium in glass culture tubes (Iwaki, 61-9718-32) and grown in an orbital shaker (Taitec, BR-43FL) at 37˚C with shaking at 250 rpm on a slant for 20 hours, achieving a final OD_{500} of approximately 6. All reagents are listed in Table S2.

Anaerobic survival assay using 96-well electrochemical potentiostat

This assay was performed following a previously described protocol (9). Initial cultures were centrifuged and washed twice with a minimal medium (MM) consisting of 100 mM MOPS (pH 7.2, adjusted with 5 N NaOH), 43 mM NaCl, 93 mM NH_4Cl, 3.7 mM KH_2PO_4, and 1 mM $MgSO_4$. The cultures were then resuspended to an optical density (OD) of 75 and transferred to an anaerobic Coy chamber maintained at 33 °C with 1–2% H_2. A 96-well screen-printed electrode plate was prepared, consisting of a carbon working electrode, a carbon counter electrode, and an Ag/AgCl reference electrode (78). Ten microliters of the concentrated culture (previously diluted to OD = 15 with N_2-sparged minimal medium) was added to each well together with 190 µL of N_2-sparged minimal medium supplemented with 20 mM D-glucose, 3.6 µM $FeSO_4$, and PCN at final concentrations of 7.5, 37.5, 75, or 375 µM (with 2.5% DMSO as the solvent).To minimize evaporation during electrochemical incubation, the plate was sealed with both a slit-seal cover (BioChromato, RSS-S96-10-S) and an aluminum seal cover (DiversifiedBiotech, ALUM-1000). The plate was incubated at 33 °C without shaking in a custom 96-potentiostat system (78), with each working electrode maintained at 0 mV versus Ag/AgCl. On days 1, 3, and 5 of incubation, the aluminum seal was removed, and the contents of each well were mixed by pipetting 150 µL at least 10 times. A 10 µL aliquot was then taken from each well for CFU enumeration. After sampling, the wells were resealed with a fresh aluminum seal and returned to the 96-potentiostat system for continued incubation. All plastic materials used inside the chamber were pre-degassed in the chamber for at least three days before use.

Colony Forming Unit (CFU) Assay

Cell cultures were diluted in phosphate-buffered saline (PBS) prior to plating. Serial dilutions spanning 5–6 orders of magnitude were prepared, and 5 µL from each dilution was spotted onto LB agar plates, followed by incubation overnight at 37 °C.

All CFU assays performed on Day 1 (including dilution, plating, and incubation) were conducted under aerobic conditions. On Days 3 and 5, all steps were conducted under anaerobic conditions: PBS was sparged with N_2 for at least 30 min prior to use, and all plastic materials as well as LB agar plates were stored in the Coy chamber for at least two days before use.

Antibiotics survival assay

Under anaerobic conditions with electrochemical incubation, ciprofloxacin (2 mg/mL in 0.1 M HCl), ceftazidime, tobramycin, and gentamicin (each 20 mg/mL in MM) were added to the wells after Day 1 of electrochemical incubation, when cells had entered a low-energy maintenance state. For each well, 1 μL of the respective antibiotic solution was added and mixed thoroughly with the culture. Samples (10 μL) were collected for CFU determination at Days 0, 1, 3, and 5. Under aerobic conditions without electrochemistry, the same four antibiotics were added to wells of a transparent plastic 96-well plate on Day 0, and the plates were incubated at 33 °C without shaking. After mixing, 5 μL samples were collected for CFU determination at 0, 6, 12, 24, 36, and 48 hours. PCN or PYO concentration was at 75 or 375 μM.

Dissolved Oxygen Consumption Measurement

Dissolved oxygen measurements were performed using an Ocean Optics FOSPOR-R oxygen probe (Ocean Insight) connected to a laptop running Ocean Optics software. Overnight cultures were pregrown in LB medium for 20 hours, harvested, and washed twice with minimal medium (MM). Cells were resuspended in MM to a concentrated OD of 15. For each replicate, experimental vials were prepared by adding 4.5 mL of oxygenated experimental buffer and a mini magnetic stir bar into 6 mL flat-bottom glass scintillation vials. The vials were placed on a magnetic stir plate

equipped with a prehensile arm to hold the FOSPOR-R probe. The probe was positioned so as not to contact the vial walls or the stir bar. The measurement was initiated by starting the stir bar and recording the baseline dissolved oxygen level for 30 s. Subsequently, 500 µL of concentrated cells was added to the vial by pipette without disturbing the probe, resulting in a final OD of 1.5. Oxygen consumption was continuously recorded for 2 minutes. All procedures described above were performed under aerobic conditions.

Arabinose-inducible efflux pump expression experiment

The *P. aeruginosa* UCBPP-PA14 strain *Δphz* attTn7::*Para:mexGHI-opmD* Gm^R was incubated under anaerobic electrochemical conditions with arabinose at final concentrations of 0, 2, 10, or 20 mM. After 24 hours of incubation, cells from each arabinose condition were collected into separate RNase-free tubes (each sample was pooled from four wells originating from the same biological batch, total volume approximately 800 µL). Samples were immediately removed from the anaerobic Coy chamber, centrifuged at 15,000 rpm for 4 min at 4 °C, and washed once with cold PBS. The supernatant was discarded, and cell pellets were processed for RNA extraction using the NucleoSpin RNA Plus kit (Takara). Complementary DNA (cDNA) synthesis was performed using the PrimeScript RT reagent kit (Takara). Quantitative RT-PCR was carried out on a StepOnePlus™ Real-Time PCR (Applied Biosystems) System using TB Green® Premix Ex Taq™ II (Takara). The housekeeping gene *oprI* was used as the internal control (3). Primers for *mexG* and *oprI* were designed based on a previous report (3). Relative gene expression levels were calculated using the $2^{-\Delta\Delta CT}$ method.

Membrane potential measurement

P. aeruginosa UCBPP-PA14 strains *Δphz* and *ΔphzΔmexS* were electrochemically incubated with PCN at a final concentration of 375 µM. After Day 1 of incubation, CCCP was added to a final concentration of 50 µM (with 3% DMSO). Membrane potential was measured on Days 1, 2, 3, and 5 using the $DiOC_2(3)$ dye following the Thermo Fisher BacLight™ Bacterial Membrane Potential Kit protocol. For each condition, 150 µL of culture was collected into a 1.5 mL tube containing 1 mM ethylenediamine tetraacetic acid (EDTA, pH 8), 30 µM $DiOC_2(3)$, and 100 nM Thiazole Red Homodimer (TODi-3, Lumiprobe). Samples were incubated for 20 min at 33 °C in the dark. Cells were then centrifuged at 8,000 rpm for 5 min, washed and resuspended once with anoxic MM in an equal volume. For microscopy, 2 µL of the stained cell suspension was spotted onto a 1% (w/v) agar pad that had been equilibrated in the Coy chamber for at least one day. To maintain anoxic conditions during imaging, anoxic 1000 sct of silicone oil (Sigma) was added on top of the agar pad prior to observation. The sample was imaged on a Nikon Eclipse Ti-2 inverted microscope equipped with an ORCA-Flash4.0 V3 camera. Excitation light (470 nm for $DiOC_2(3)$ and 640 nm for TODi-3) was supplied through a SpectraX LED light engine with a 200-ms exposure. Emission light from $DiOC_2(3)$ was collected using standard FITC (green) and TRITC (red) filter cubes (Semrock), respectively, with the excitation filter removed. Emission light from TODi-3 was collected using a Cy5 filter cube (Semrock). The number of cells and the fluorescence intensity in each channel were quantified using ImageJ (NIH). Cells were manually selected by applying intensity thresholds, and regions of interest (ROIs) corresponding to individual cells were defined using the ROI Manager. The fluorescence intensity of each cell was then measured in the respective channels with appropriate LUTs applied.

Statistical Analysis

All statistical analyses, except for the integration of current, were performed using Prism 10 (GraphPad Software). The integration of current was conducted using custom scripts in Python 3.

3.5 ›Figures

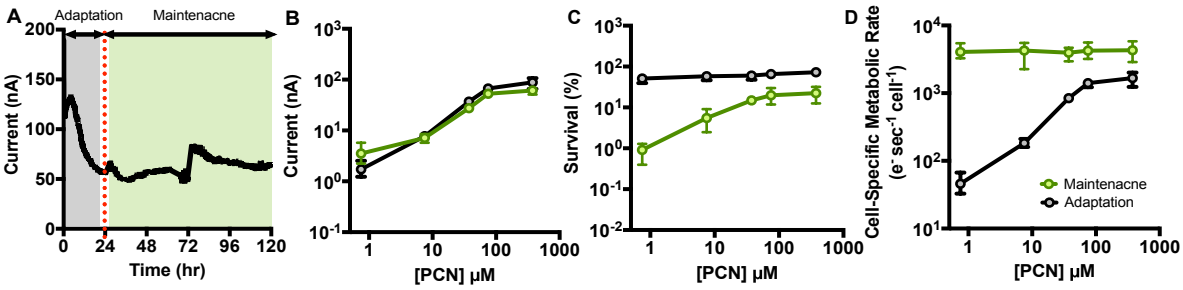


Figure 1. Adaptation and maintenance phases exhibit distinct metabolic constraints governing anaerobic PCN-driven metabolism.

(A) Mean current generated by *Δphz* strain at 375 µM over 5 days. Data represent four biological replicates.

(B) Current output, (C) survival, and (D) cell-specific metabolic rate of *Δphz* strain after 5 days of anaerobic electrochemical incubation in glucose minimal medium at various PCN concentrations. Current values were averaged over day 0-1 (adaptation) or days 1–5 (maintenance), and survival represents the geometric mean of CFU counts from day 0-1 or days 1–5 (100% survival corresponds to approximately 1×10^9 CFU mL^{-1}). Data represent mean ± SD of four biological replicates.

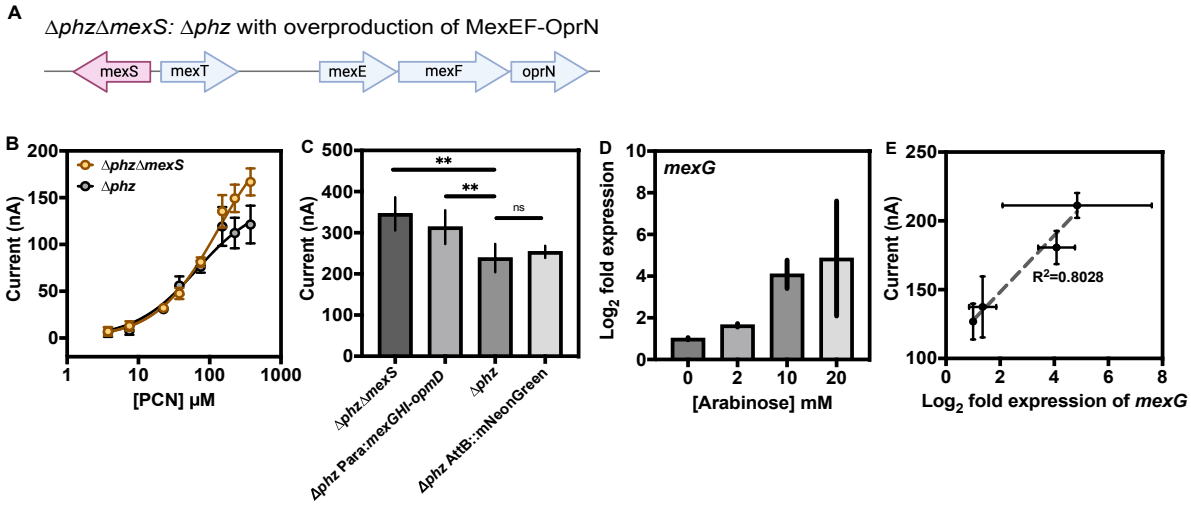


Figure 2. Efflux pump activity becomes linked to metabolic flux at high PCN levels during the adaptation phase.

(A) Regulation of the *mexEF-oprN* operon. Deletion of *mexS* derepresses *mexT*, resulting in constitutive *mexEF-oprN* overexpression.

(B) Current output of *Δphz* and *ΔphzΔmexS* strains during anaerobic electrochemical incubation in glucose minimal medium at various PCN concentrations.

(C) Current produced by *Δphz, ΔphzΔmexS,* Δ*phz Para:mexGHI* treated with arabinose (20mM), and *Δphz* AttB::mNeonGreen strains during anaerobic electrochemical incubation with 375 μM PCN.

(D) Arabinose-inducible expression of *mexG* in the *Δphz att*Tn7::Para:*mexGHI-opmD* Gm^R after 24-hour electrochemical incubation with 375 μM PCN.

(E) A correlation between *mexG* expression and current averaged over 24 hours.

All data represent mean ± SD from at least three biological replicates, and current values were averaged over days 0-1.

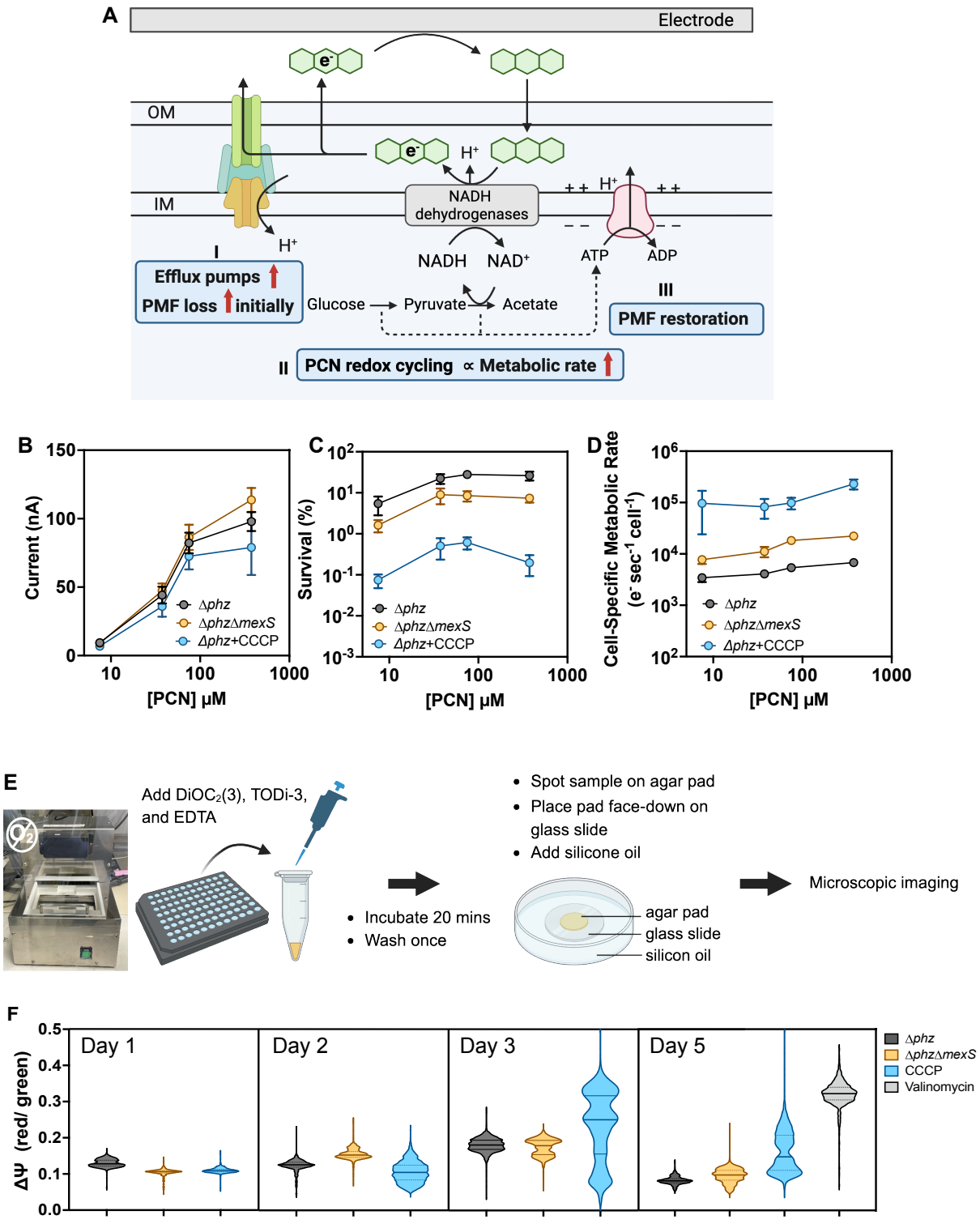


Figure 3. Metabolic compensation sustains PMF under a low-energy maintenance state.

(A) Proposed model of metabolic compensation driven by RND efflux pump overexpression. (I) Overexpression of RND efflux pumps increases their activity and PMF dissipation. (II) Increased PMF demand drives higher NADH oxidation, thereby

activating PCN redox cycling. (III) Enhanced metabolism promotes ATP generation, allowing restoration of PMF.

(B) Current output, (C) survival, and (D) cell-specific metabolic rate of *Δphz, ΔphzΔmexS*, and *Δphz* treated with CCCP (50 μM) during 5 days of anaerobic electrochemical incubation in glucose minimal medium at various PCN concentrations. Current values were averaged over days 1–5; survival represents the geometric mean of CFU counts from days 1–5; and cell-specific metabolic rates were calculated from days 1–5. All data represent mean ± SD from at least four biological replicates.

(E) Experimental design of the membrane potential measurement.

(F) Membrane potential (Δψ) dynamics of *Δphz, ΔphzΔmexS*, and *Δphz* treated with CCCP (50 μM) from day 1–5 of anaerobic electrochemical incubation in glucose minimal medium at 375 μM PCN. Violin plots show the distribution of membrane potential, expressed as the red/green fluorescence ratio of $DiOC_2(3)$, measured on days 1, 2, 3, and 5. CCCP was included as a depolarizing control, which produced a slight decrease in membrane potential measurements on day 1, and valinomycin was used as a hyperpolarization control. Each violin represents pooled single-cell measurements from two independent biological replicates, with 700–3,000 cells analyzed per replicate.

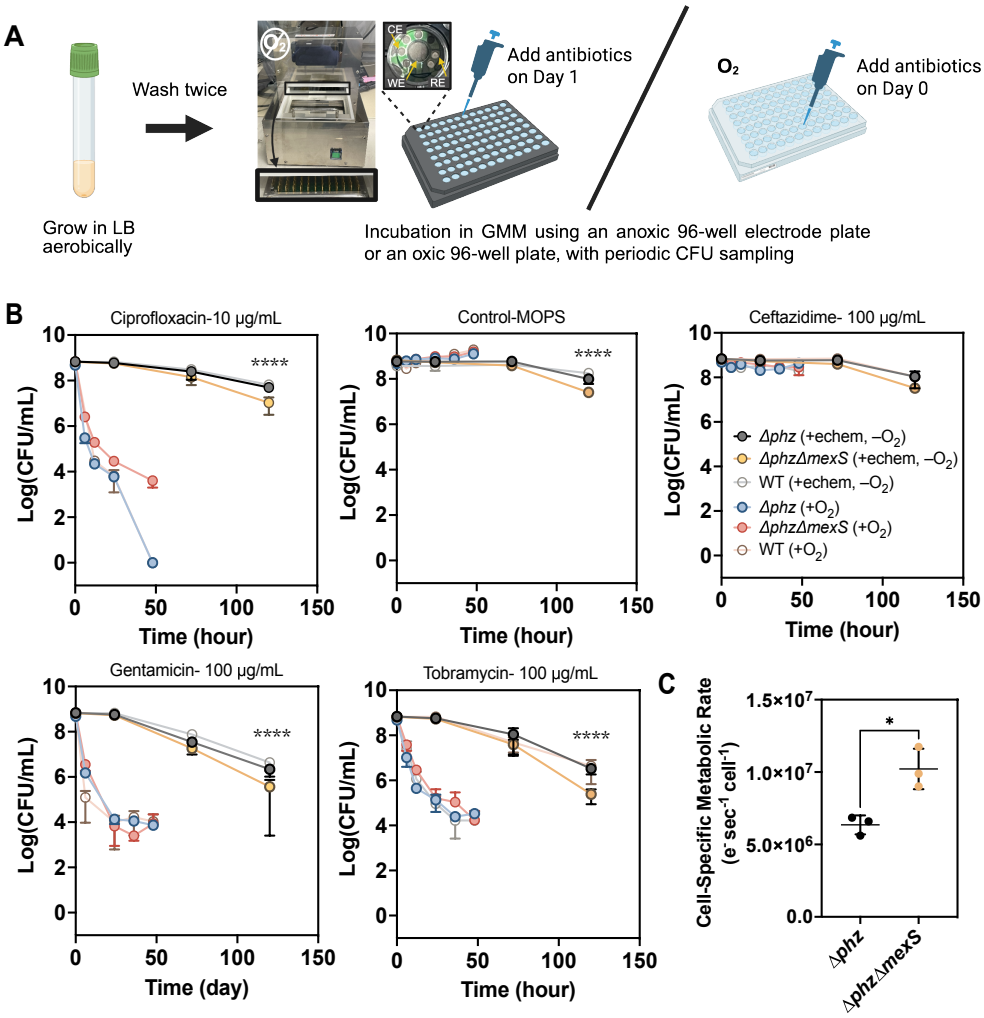


Figure 4. Unlike their role in promoting antibiotic tolerance under aerobic conditions, efflux pump overexpression paradoxically increases antibiotic sensitivity under anaerobic conditions.

(A) Experimental design of the antibiotic survival assay. A 96-well plate potentiostat system was used for anaerobic electrochemical incubation. Each well contained an independent three-electrode configuration consisting of a carbon working electrode (WE), a carbon counter electrode (CE), and an Ag/AgCl reference electrode (RE), interfacing with the potentiostat via contact pins located at the bottom of the plate. GMM, glucose minimal medium.

(B) Time-dependent survival dynamics of wild-type (WT), *Δphz* and *ΔphzΔmexS* strains under anaerobic and aerobic conditions. CFU counts were measured in the absence (Control-MOPS) or presence of tobramycin (100 μg/mL), gentamicin (100 μg/mL), ceftazidime (100 μg/mL), or ciprofloxacin (10 μg/mL). Data represent mean ± SD from at least three biological replicates.

(C) The cell-specific metabolic rate was calculated from the slope of the regression. Welch's t-test was used to compare samples, *p<0.05. Data represent mean ± SD from three technical replicates (from one of two biological replicates).

3.6 Supplementary materials

Detailed Experimental Protocols

Mutant Construction and Complementation

Δphz AttB::mNeonGreen strain (ask Richard) if data will be used.

Primers were synthesized by Integrated DNA Technologies (sequences listed below). The mexS coding region was inserted into the eGRS96 plasmid under the control of the rhamnose-inducible promoter (pRha) using Gibson Assembly (NEB). The constructed plasmid, which confers gentamicin resistance, was electroporated into P. aeruginosa ΔphzΔmexS, and transformants were selected on LB agar supplemented with gentamicin []. For complementation experiments, cultures electrochemically incubated in Glucose-MM supplemented with L-rhamnose (0.01% w/v) to induce mexS expression.

ATP Quantification

ATP levels were measured using the BacTiter-Glo™ Microbial Cell Viability Assay (Promega) according to the manufacturer's instructions. On Day 5 of anaerobic electrochemical incubation, 100 µL of culture was collected from each replicate (Δphz, ΔphzΔmexS, and Δphz treated with CCCP; n = 4 per condition), pelleted by centrifugation at 8,100 rpm for 5 min, and washed twice with an equal volume of anoxic PBS. ATP quantification was performed immediately after the final resuspension using a microplate reader SH-9000 (Corona Electric). Luminescence values were normalized to CFUs obtained on the same day to calculate ATP per viable cell.

VBNC State Measurement

On Day 5 of the anaerobic electrochemical incubation, cultures of Δphz, ΔphzΔmexS, and Δphz treated with CCCP (PCN = 75 μM) were collected by centrifugation at 8,000 rpm for 5 min and washed twice with an equal volume of anoxic PBS. Cell pellets were resuspended in anoxic PBS and stained with SYTO 9 (6.3 μM) and propidium iodide (37.5 μM) using the LIVE/DEAD® BacLight™ Bacterial Viability Kit (Invitrogen). Samples were incubated for 15 min at 33 °C in the dark under aerobic conditions. For microscopy, 2 μL of the stained cell suspension was spotted onto a 1% (w/v) agar pad. Fluorescence imaging was performed on a Leica DFC450C epifluorescence microscope equipped with FITC and TXR filter sets for SYTO 9 and propidium iodide signals, respectively. The number of cells exhibiting fluorescence in each channel was quantified using ImageJ (NIH). Cells were manually selected by applying intensity thresholds, and ROIs corresponding to individual cells were defined using the ROI Manager. A total of 500–1,500 cells were analyzed for each sample

Table S1. Bacterial strains, plasmids, and primers

Strains/ plasmids/ primers	Source/ reference
Pseudomonas aeruginosa UCBPP-PA14	
Wild type	
Δ*phz1/2*	(19)
Δ*phz1/2*Δ*mexS*	(3)
Δ*phz1/2*Δ*mexS* (eGRS96-*mexS*)	This study
Δ*phz* AttB::*mNeonGreen*	This study
Escherichia coli	
DH10-beta	Life Technology
Plasmids	
eGRS96*	
pUC18T-mini-Tn7T-GmR	
Primers	
mexS forward: TGCAGTAAGGAGGAACAGCTATGTCCCGAGTGATCCGTTT	This study
mexS reverse: TCTCATCCGCCAAAACAGCCTCAATCGGCGACGTGGATCA	This study

* pMQ72(79) derivative with yeast elements (2μ, URA3) removed and pBAD promoter replaced by rhamnose-inducible pRha promoter.

Table S2. Reagents

Chemicals	Source	Identifier
Difco LB Broth	BD	244620
Agar	Nacalai	01028-85
MOPS	Sigma-Aldrich	M1254
Sodium Chloride	Fujifilm-Wako	191-01665
Ammonium Chloride	Fujifilm-Wako	017-02995
Potassium Phosphate Monobasic	Fujifilm-Wako	136-14485
Magnesium Sulphate Heptahydrate	Fujifilm-Wako	131-00405
Iron(II) Sulphate Heptahydrate	Fujifilm-Wako	095-01095
D-Glucose	Fujifilm-Wako	049-31165
L-Arabinose	Fujifilm-Wako	012-04581
α-L-Rhamnose	Fujifilm-Wako	180-00752
Phenazine-1-carboxamide	Combi-Blocks	QC-6178
Potassium Nitrate	Nacalai Tesque	28704-85
DMSO	Nacalai Tesque	13407-45
Ciprofloxacin	Sigma-Aldrich	17850
Ceftazidime Hydrate	Sigma-Aldrich	A6987
Tobramycin	Sigma-Aldrich	T4014
Gentamicin Sulfate	Nacalai Tesque	08975-94
CCCP	Sigma-Aldrich	215911
Valinomycin	Sigma-Aldrich	94675
Nigericin Sodium Salt	MedChemExpress	HY-100381
$DiOC_2(3)$	Invitrogen	D14730
TODi-3	Lumiprobe	A2610
BCECF-AM	Invitrogen	B1150

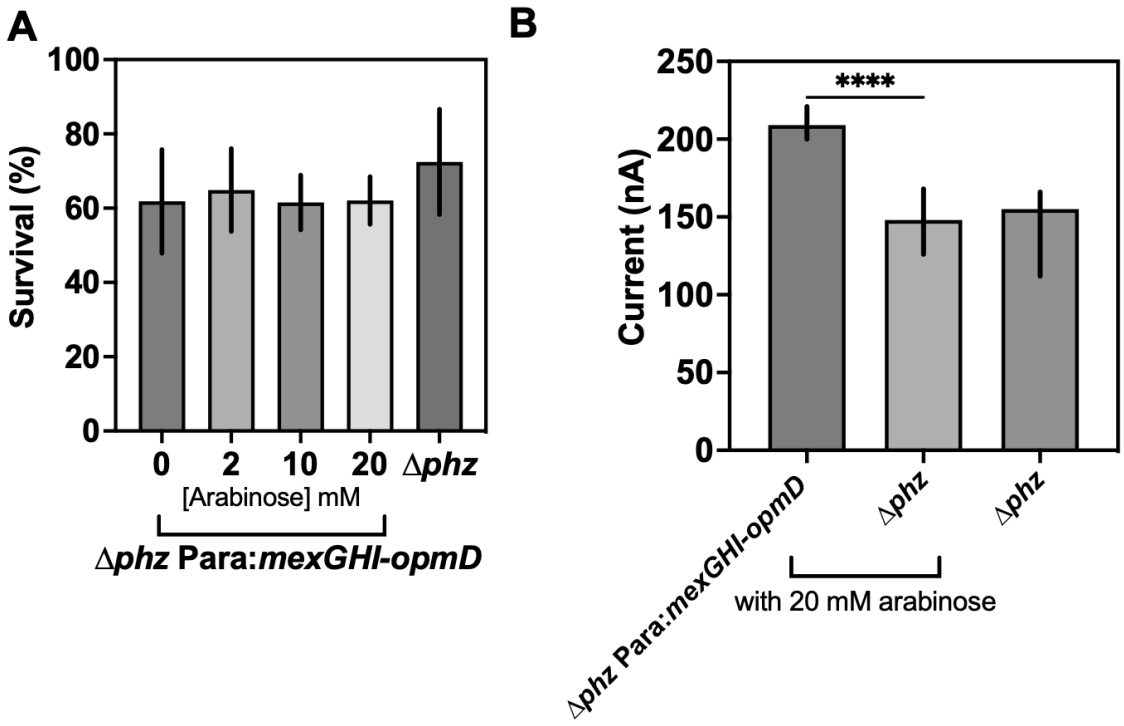


Figure S1. The arabinose-inducible *Δphz Para:mexGHI* strain shows higher current production than *Δphz* without affecting survival.

(A) Survival of *Δphz Para:mexGHI* at different concentrations of arabinose, with *Δphz* as a negative control. Data represent mean ± SD from at least four biological replicates. 100% survival corresponds to approximately 5×10^8 CFU mL^{-1}.
(B) Current produced *Δphz Para:mexGHI* with 20 mM arabinose and by *Δphz* with or without 20 mM arabinose. Current values were averaged over the first 24 hours of anaerobic electrochemical incubation with 375 µM PCN. Data represent mean ± SD from at least four biological replicates. Welch's t-test was used to compare samples, ****$p<0.0001$.

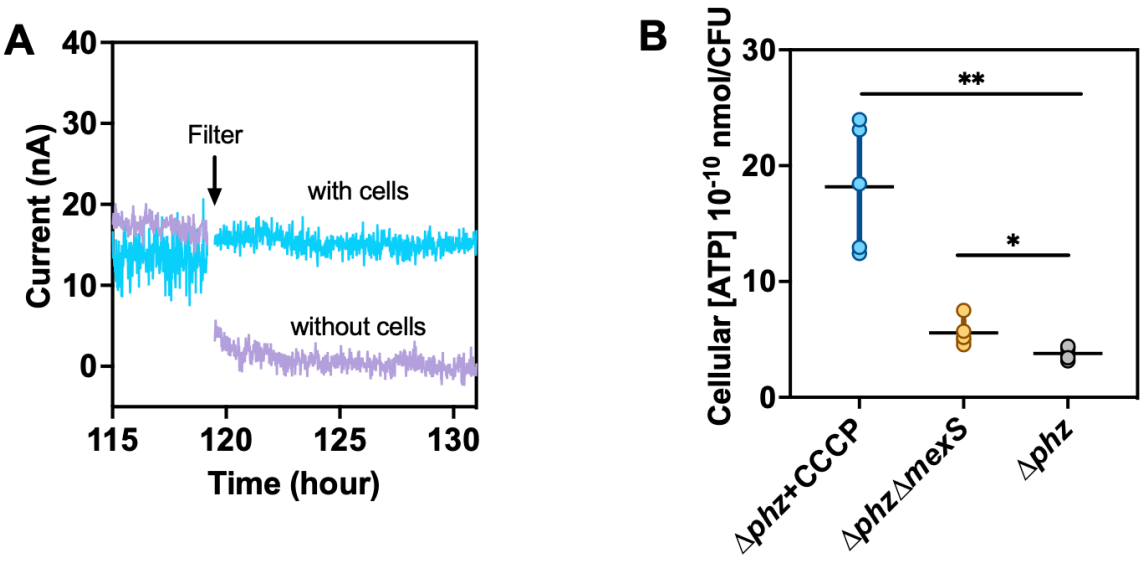


Figure S2. Low-energy maintenance metabolism in *Δphz*, *ΔphzΔmexS*, and *Δphz* treated with CCCP (50 µM).

(A) Representative current profiles from four biological replicates. After 5 days of electrochemical incubation with 375 µM PCN, cells from four wells were filtered through a 0.2 µm cellulose acetate membrane and transferred into a new electrode plate (current without *Δphz*). Cells from the other four wells were directly transferred into a new electrode plate (current with *Δphz*).

(B) Intracellular ATP levels after 5 days of anaerobic electrochemical incubation. Data represent mean ± SD from at least five biological replicates. Welch's *t*-test was used for comparisons between samples (*$p<0.05$; **$p<0.01$).

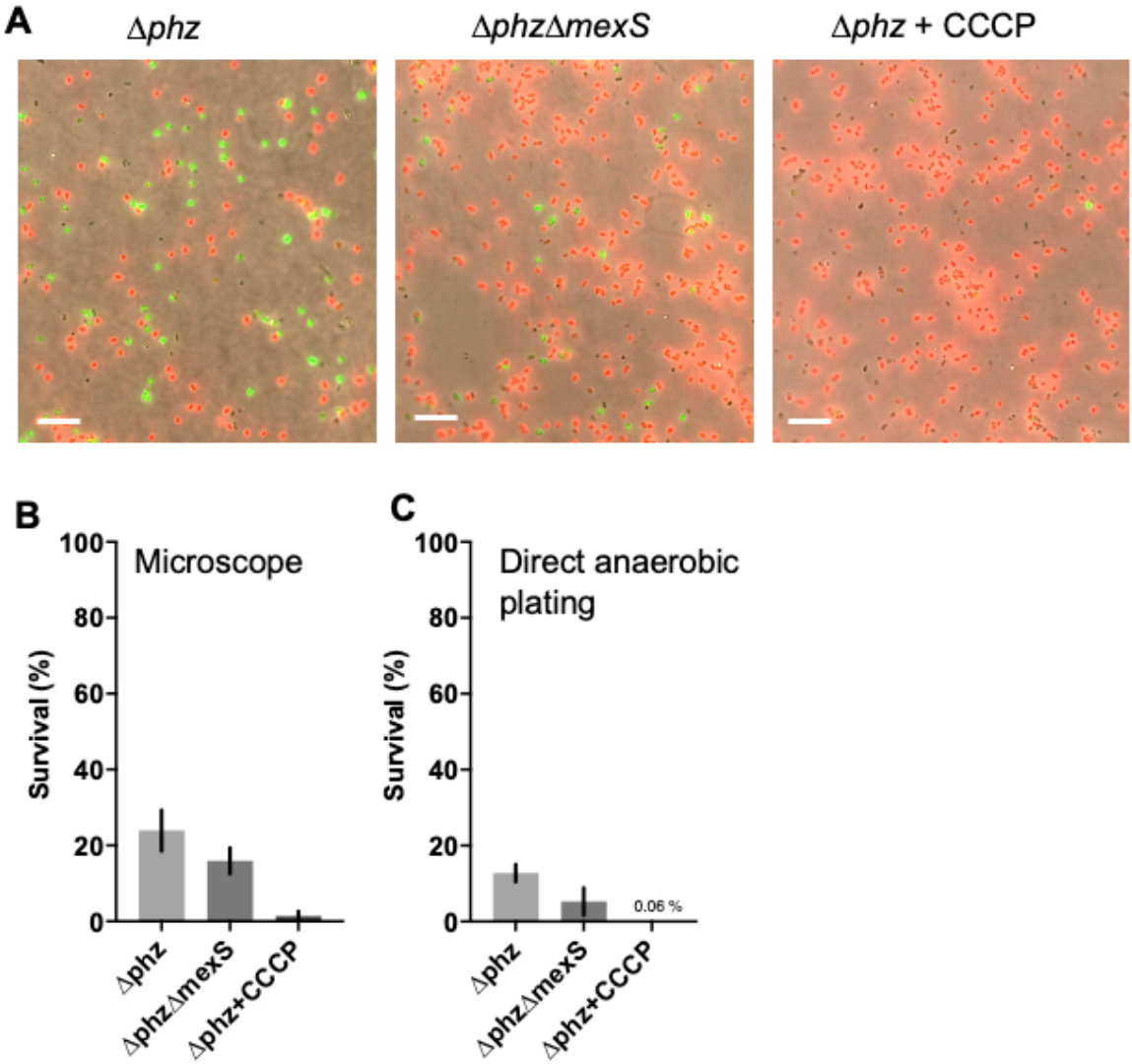


Figure S3. The contribution of VBNC cells was minimal in our system.

(A) Representative microscopy images of *Δphz*, *ΔphzΔmexS*, and *Δphz* treated with CCCP (50 µM). Syto 9 (green fluorescence) marks live cells, and propidium iodide (red fluorescence) marks dead cells. Scale bar: 10 µm.

(B) Survival calculated from fluorescence microscopy images (500–1,200 cells analyzed per batch). Data represent mean ± SD from three biological replicates.

(C) Survival calculated from direct anaerobic plating. Data represent mean ± SD from at least four biological replicates.

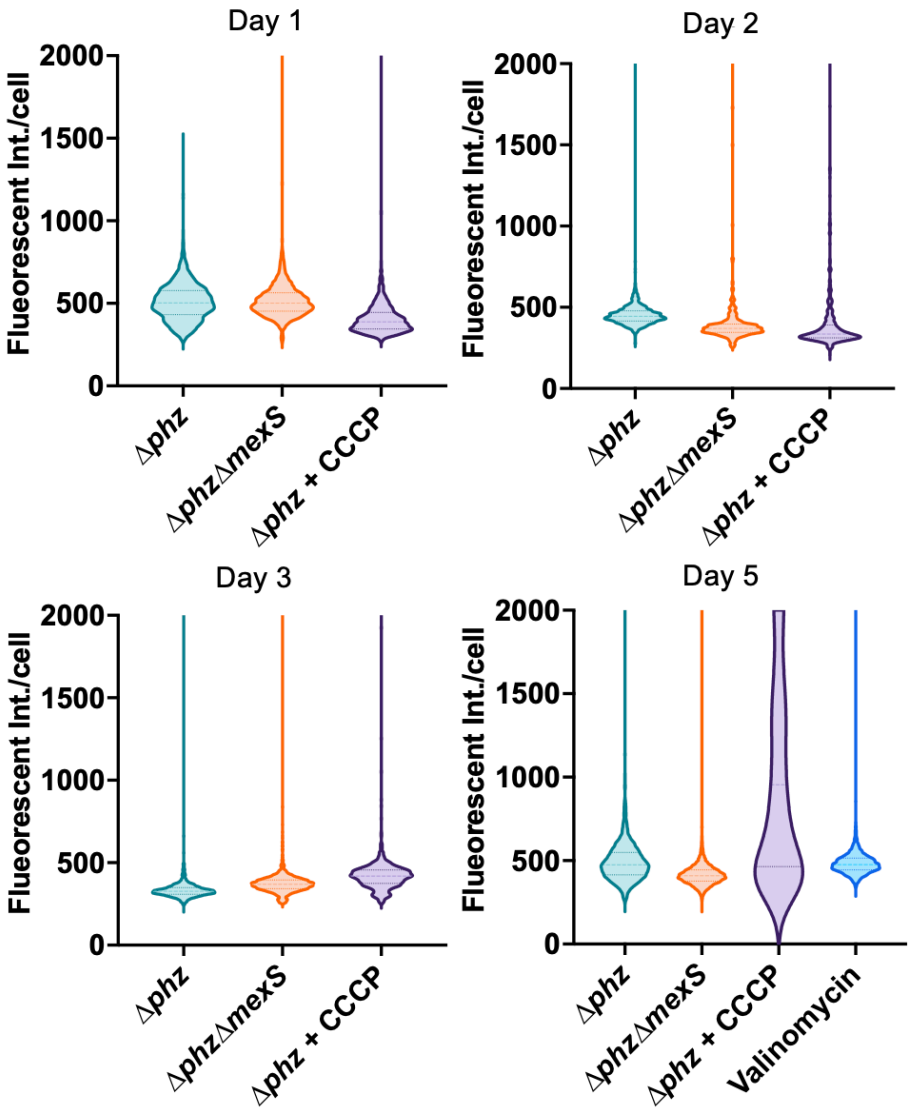


Figure S4. Fluorescence of TODi-3 in *Δphz*, *ΔphzΔmexS*, and *Δphz* treated with CCCP (50 µM) during days 1–5.

Violin plots illustrate the distribution of fluorescence intensity and allow assessment of whether cell death differs significantly between strains or conditions. Each violin represents pooled single-cell measurements from two independent biological replicates, with 400–2,000 cells analyzed per replicate.

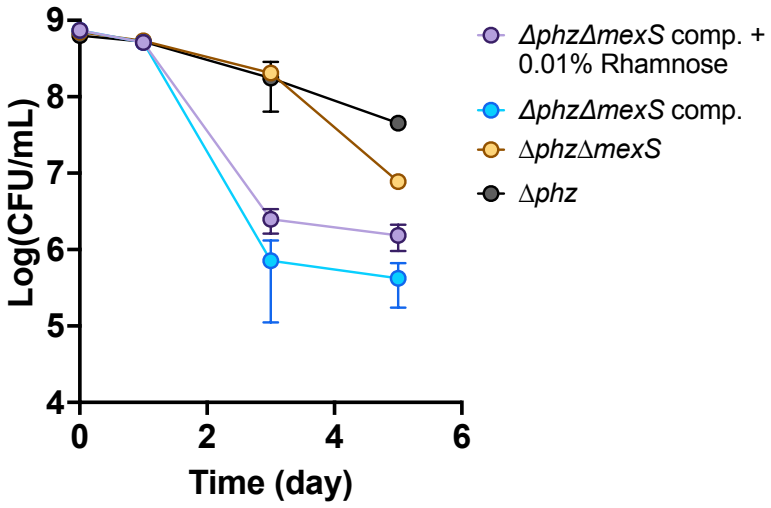


Figure S5. The *mexS* mutation increases antibiotic sensitivity under anaerobic, energy-limited conditions.

Time-dependent survival dynamics of *Δphz*, *ΔphzΔmexS*, and *ΔphzΔmexS* complemented with *mexS*, with or without 0.01% (w/v) rhamnose, during anaerobic electrochemical incubation. CFU counts were measured in the presence of ciprofloxacin (10 µg mL^{-1}). Data represent mean ± SD from at least three biological replicates.

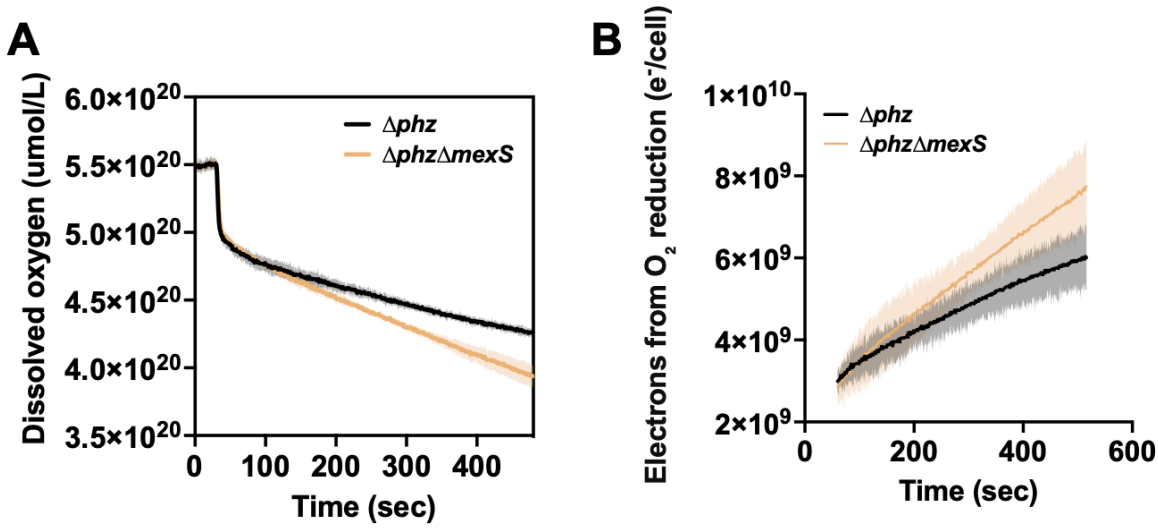


Figure S6. The *mexS* mutation increases cell-specific metabolic rate under anaerobic, energy-limited conditions.

(A) Oxygen consumption kinetics of *Δphz* and *ΔphzΔmexS* strains in minimal medium under oxic conditions. Cell density corresponds to 2×10^{10} CFU mL-1.
(B) Because molecular oxygen can accept four electrons, the data in Figure S2A were converted from μmol of oxygen consumed to electrons transferred.

3.7 References

1. D. Du *et al.*, Multidrug efflux pumps: structure, function and regulation. *Nature Reviews Microbiology* **16**, 523-539 (2018).
2. L. J. V. Piddock, Multidrug-resistance efflux pumps ? not just for resistance. *Nature Reviews Microbiology* **4**, 629-636 (2006).
3. L. A. Meirelles, E. K. Perry, M. Bergkessel, D. K. Newman, Bacterial defenses against a natural antibiotic promote collateral resilience to clinical antibiotics. *PLOS Biology* **19**, e3001093 (2021).
4. X.-Z. Li, P. Plésiat, H. Nikaido, The Challenge of Efflux-Mediated Antibiotic Resistance in Gram-Negative Bacteria. *Clinical Microbiology Reviews* **28**, 337-418 (2015).
5. P. S. Stewart, M. J. Franklin, Physiological heterogeneity in biofilms. *Nature Reviews Microbiology* **6**, 199-210 (2008).
6. M. Schobert, P. Tielen, Contribution of Oxygen-Limiting Conditions to Persistent Infection of *Pseudomonas Aeruginosa*. *Future Microbiology* **5**, 603-621 (2010).
7. J. Baishya, C. A. Wakeman, Selective pressures during chronic infection drive microbial competition and cooperation. *npj Biofilms and Microbiomes* **5**, 16 (2019).
8. L.-A. Meyer-Reil, Microbial life in sedimentary biofilms–the challenge to microbial ecologists. *Marine Ecology Progress Series* **112**, 303-311 (1994).
9. J. A. Ciemniecki, C.-L. Ho, R. D. Horak, A. Okamoto, D. K. Newman, Mechanistic study of a low-power bacterial maintenance state using high-throughput electrochemistry. *Cell* **187**, 6882-6895.e6888 (2024).
10. J. O. Pacheco, C. Alvarez-Ortega, M. A. Rico, J. L. Martínez, Metabolic Compensation of Fitness Costs Is a General Outcome for Antibiotic-Resistant *Pseudomonas aeruginosa* Mutants Overexpressing Efflux Pumps. *mBio* **8**, e00500-00517 (2017).
11. J. Olivares, C. Álvarez-Ortega, J. L. Martinez, Metabolic Compensation of Fitness Costs Associated with Overexpression of the Multidrug Efflux Pump MexEF-OprN in *Pseudomonas aeruginosa*. *Antimicrobial Agents and Chemotherapy* **58**, 3904-3913 (2014).
12. M. C. Walters, F. Roe, A. Bugnicourt, M. J. Franklin, P. S. Stewart, Contributions of Antibiotic Penetration, Oxygen Limitation, and Low

Metabolic Activity to Tolerance of *Pseudomonas aeruginosa* Biofilms to Ciprofloxacin and Tobramycin. *Antimicrobial Agents and Chemotherapy* **47**, 317-323 (2003).

13. P. S. Stewart, J. William Costerton, Antibiotic resistance of bacteria in biofilms. *The Lancet* **358**, 135-138 (2001).

14. I. Alav, J. M. Sutton, K. M. Rahman, Role of bacterial efflux pumps in biofilm formation. *Journal of Antimicrobial Chemotherapy* **73**, 2003-2020 (2018).

15. J. B. H. Shyu, D. P. Lies, D. K. Newman, Protective Role of *tolC* in Efflux of the Electron Shuttle Anthraquinone-2,6-Disulfonate. *Journal of Bacteriology* **184**, 1806-1810 (2002).

16. N. R. Glasser, S. H. Saunders, D. K. Newman, The Colorful World of Extracellular Electron Shuttles. *Annual Review of Microbiology* **71**, 731-751 (2017).

17. J. A. Ciemniecki, D. K. Newman, NADH dehydrogenases are the predominant phenazine reductases in the electron transport chain of *Pseudomonas aeruginosa*. *Molecular Microbiology* **119**, 560-573 (2023).

18. H. Sakhtah *et al.*, The *Pseudomonas aeruginosa* efflux pump MexGHI-OpmD transports a natural phenazine that controls gene expression and biofilm development. *Proceedings of the National Academy of Sciences* **113**, E3538-E3547 (2016).

19. L. E. P. Dietrich, A. Price-Whelan, A. Petersen, M. Whiteley, D. K. Newman, The phenazine pyocyanin is a terminal signalling factor in the quorum sensing network of *Pseudomonas aeruginosa*. *Molecular Microbiology* **61**, 1308-1321 (2006).

20. S. H. Saunders *et al.*, Extracellular DNA Promotes Efficient Extracellular Electron Transfer by Pyocyanin in *Pseudomonas aeruginosa* Biofilms. *Cell* **182**, 919-932.e919 (2020).

21. D. Wolloscheck, G. Krishnamoorthy, J. Nguyen, H. I. Zgurskaya, Kinetic Control of Quorum Sensing in Pseudomonas aeruginosa by Multidrug Efflux Pumps. *ACS Infectious Diseases* **4**, 185-195 (2018).

22. A. Verchère, I. Broutin, M. Picard, Photo-induced proton gradients for the in vitro investigation of bacterial efflux pumps. *Scientific Reports* **2**, 306 (2012).

23. Y. Morita, J. Tomida, Y. Kawamura, Efflux-mediated fluoroquinolone resistance in the multidrug-resistant *Pseudomonas aeruginosa* clinical isolate

PA7: identification of a novel MexS variant involved in upregulation of the mexEF-oprN multidrug efflux operon. *Frontiers in Microbiology* **6**, 8 (2015).

24. M. L. Sobel, S. Neshat, K. Poole, Mutations in PA2491 (*mexS*) Promote MexT-Dependent *mexEF-oprN* Expression and Multidrug Resistance in a Clinical Strain of *Pseudomonas aeruginosa*. *Journal of Bacteriology* **187**, 1246-1253 (2005).

25. J. Liu, L. Yang, B. V. Kjellerup, Z. Xu, Viable but nonculturable (VBNC) state, an underestimated and controversial microbial survival strategy. *Trends in Microbiology* **31**, 1013-1023 (2023).

26. L. V. Johnson, M. L. Walsh, B. J. Bockus, L. B. Chen, Monitoring of relative mitochondrial membrane potential in living cells by fluorescence microscopy. *Journal of Cell Biology* **88**, 526-535 (1981).

27. G. Terradot, E. Krasnopeeva, P. S. Swain, T. Pilizota, Escherichia coli Maintains pH via the Membrane Potential. *PRX Life* **2**, 043015 (2024).

28. R. D. Horak, J. A. Ciemniecki, D. K. Newman, Bioenergetic suppression by redox-active metabolites promotes antibiotic tolerance in Pseudomonas aeruginosa. *Proceedings of the National Academy of Sciences* **121**, e2406555121 (2024).

29. T. Ziglari, Z. Wang, A. Holian, Contribution of Particle-Induced Lysosomal Membrane Hyperpolarization to Lysosomal Membrane Permeabilization. *International Journal of Molecular Sciences* **22**, 2277 (2021).

30. J. Porter, R. Pickup, C. Edwards, Membrane hyperpolarisation by valinomycin and its limitations for bacterial viability assessment using rhodamine 123 and flow cytometry. *FEMS Microbiology Letters* **132**, 259-262 (1995).

31. A. San Millan, R. C. MacLean, Fitness Costs of Plasmids: a Limit to Plasmid Transmission. *Microbiol Spectr* **5** (2017).

32. C. Llanes *et al.*, Role of the MexEF-OprN Efflux System in Low-Level Resistance of *Pseudomonas aeruginosa* to Ciprofloxacin. *Antimicrobial Agents and Chemotherapy* **55**, 5676-5684 (2011).

33. M. L. Sobel, G. A. McKay, K. Poole, Contribution of the MexXY Multidrug Transporter to Aminoglycoside Resistance in *Pseudomonas aeruginosa* Clinical Isolates. *Antimicrobial Agents and Chemotherapy* **47**, 3202-3207 (2003).

34. S. Fraud, K. Poole, Oxidative Stress Induction of the MexXY Multidrug Efflux Genes and Promotion of Aminoglycoside Resistance Development in

Pseudomonas aeruginosa. *Antimicrobial Agents and Chemotherapy* **55**, 1068-1074 (2011).

35. E. Tuomanen, Phenotypic Tolerance: The Search for β-Lactam Antibiotics That Kill Nongrowing Bacteria. *Reviews of Infectious Diseases* **8**, S279-S291 (1986).

36. A. L. Spoering, K. Lewis, Biofilms and Planktonic Cells of *Pseudomonas aeruginosa* Have Similar Resistance to Killing by Antimicrobials. *Journal of Bacteriology* **183**, 6746-6751 (2001).

37. R. La Rosa, H. K. Johansen, S. Molin, Adapting to the Airways: Metabolic Requirements of Pseudomonas aeruginosa during the Infection of Cystic Fibrosis Patients. *Metabolites* **9**, 234 (2019).

38. D. W. Basta, M. Bergkessel, D. K. Newman, Identification of Fitness Determinants during Energy-Limited Growth Arrest in Pseudomonas aeruginosa. *mBio* **8**, 10.1128/mbio.01170-01117 (2017).

39. C. P. Kempes *et al.*, Drivers of Bacterial Maintenance and Minimal Energy Requirements. *Frontiers in Microbiology* **Volume 8 - 2017** (2017).

40. A. J. Hulbert, P. L. Else, Membranes and the setting of energy demand. *Journal of Experimental Biology* **208**, 1593-1599 (2005).

41. P. Pearson James, C. Van Delden, H. Iglewski Barbara, Active Efflux and Diffusion Are Involved in Transport of Pseudomonas aeruginosa Cell-to-Cell Signals. *Journal of Bacteriology* **181**, 1203-1210 (1999).

42. S. Gervasoni *et al.*, Molecular determinants of avoidance and inhibition of Pseudomonas aeruginosa MexB efflux pump. *mBio* **14**, e01403-01423 (2023).

43. M. Wang, E. W. C. Chan, Y. Wan, M. H.-y. Wong, S. Chen, Active maintenance of proton motive force mediates starvation-induced bacterial antibiotic tolerance in *Escherichia coli*. *Communications Biology* **4**, 1068 (2021).

44. B. Yang, Z. Tong, J. Shi, Z. Wang, Y. Liu, Bacterial proton motive force as an unprecedented target to control antimicrobial resistance. *Medicinal Research Reviews* **43**, 1068-1090 (2023).

45. D. White, J. T. Drummond, C. Fuqua, The physiology and biochemistry of prokaryotes. (1995).

46. S. Schink *et al.*, Survival dynamics of starving bacteria are determined by ion homeostasis that maintains plasmolysis. *Nature Physics* **20**, 1332-1338 (2024).

47. A. G. Kléber, Resting membrane potential, extracellular potassium activity, and intracellular sodium activity during acute global ischemia in isolated perfused guinea pig hearts. *Circulation Research* **52**, 442-450 (1983).

48. J. K. Lanyi, The role of Na^+ in transport processes of bacterial membranes. *Biochimica et Biophysica Acta (BBA) - Reviews on Biomembranes* **559**, 377-397 (1979).

49. Y. H. Ko, S. Hong, P. L. Pedersen, Chemical Mechanism of ATP Synthase: MAGNESIUM PLAYS A PIVOTAL ROLE IN FORMATION OF THE TRANSITION STATE WHERE ATP IS SYNTHESIZED FROM ADP AND INORGANIC PHOSPHATE *. *Journal of Biological Chemistry* **274**, 28853-28856 (1999).

50. Y. HE *et al.*, Correlation between the inhibition of cell growth by accumulated polyamines and the decrease of magnesium and ATP. *European Journal of Biochemistry* **217**, 89-96 (1993).

51. D. C. Yoch, R. Carithers, Bacterial iron-sulfur proteins. *Microbiological Reviews* **43**, 384-421 (1979).

52. K. O. Konhauser, A. Kappler, E. E. Roden, IRON IN MICROBIAL METABOLISMS. *Elements* **7**, 89-93 (2011).

53. R. Cord-Ruwisch, Y. Law, K. Y. Cheng, Ammonium as a sustainable proton shuttle in bioelectrochemical systems. *Bioresource Technology* **102**, 9691-9696 (2011).

54. E. Padan, D. Zilberstein, S. Schuldiner, pH homesstasis in bacteria. *Biochimica et Biophysica Acta (BBA) - Reviews on Biomembranes* **650**, 151-166 (1981).

55. D. L. Kirchman, R. G. Keil, P. A. Wheeler, The effect of amino acids on ammonium utilization and regeneration by heterotrophic bacteria in the subarctic Pacific. *Deep Sea Research Part A. Oceanographic Research Papers* **36**, 1763-1776 (1989).

56. D. Kleiner, Bacterial ammonium transport. *FEMS Microbiology Letters* **32**, 87-100 (1985).

57. L. N. Csonka, Physiological and genetic responses of bacteria to osmotic stress. *Microbiological Reviews* **53**, 121-147 (1989).

58. T. Müller, B. Walter, A. Wirtz, A. Burkovski, Ammonium Toxicity in Bacteria. *Current Microbiology* **52**, 400-406 (2006).

59. W. F. Boron, P. De Weer, Intracellular pH transients in squid giant axons caused by CO_2, NH_3, and metabolic inhibitors. *Journal of General Physiology* **67**, 91-112 (1976).

60. J. Kang, Y.-H. Cho, Y. Lee, Pyocyanin and 1-Hydroxyphenazine Promote Anaerobic Killing of Pseudomonas aeruginosa via Single-Electron Transfer with Ferrous Iron. *Microbiology Spectrum* **10**, e02312-02322 (2022).

61. T. H. Hohle, M. R. O'Brian, Magnesium-dependent processes are targets of bacterial manganese toxicity. *Molecular Microbiology* **93**, 736-747 (2014).

62. T. Ko¨hler *et al.*, Characterization of MexE–MexF–OprN, a positively regulated multidrug efflux system of Pseudomonas aeruginosa. *Molecular Microbiology* **23**, 345-354 (1997).

63. J. R. Aires, J.-C. Pechère, C. V. Delden, T. Köhler, Amino Acid Residues Essential for Function of the MexF Efflux Pump Protein of Pseudomonas aeruginosa. *Antimicrobial Agents and Chemotherapy* **46**, 2169-2173 (2002).

64. R. Yonehara, E. Yamashita, A. Nakagawa, Crystal structures of OprN and OprJ, outer membrane factors of multidrug tripartite efflux pumps of Pseudomonas aeruginosa. *Proteins: Structure, Function, and Bioinformatics* **84**, 759-769 (2016).

65. S. Yamasaki, M. Zwama, T. Yoneda, M. Hayashi-Nishino, K. Nishino, Drug resistance and physiological roles of RND multidrug efflux pumps in Salmonella enterica, Escherichia coli and Pseudomonas aeruginosa. *Microbiology* **169** (2023).

66. X. Li, Y. Li, R. Wang, Q. Wang, L. Lu, Toxoflavin Produced by *Burkholderia gladioli* from *Lycoris aurea* Is a New Broad-Spectrum Fungicide. *Applied and Environmental Microbiology* **85**, e00106-00119 (2019).

67. J. Kim *et al.*, Quorum sensing and the LysR-type transcriptional activator ToxR regulate toxoflavin biosynthesis and transport in Burkholderia glumae. *Molecular Microbiology* **54**, 921-934 (2004).

68. K. Tahlan *et al.*, Initiation of actinorhodin export in *Streptomyces coelicolor*. *Molecular Microbiology* **63**, 951-961 (2007).

69. Y. Xu, A. Willems, C. Au-yeung, K. Tahlan, J. R. Nodwell, A Two-Step Mechanism for the Activation of Actinorhodin Export and Resistance in *Streptomyces coelicolor*. *mBio* **3**, e00191-00112 (2012).

70. X. Sun *et al.*, Chemical Recording of Pump-Specific Drug Efflux in Living Cells. *Angewandte Chemie International Edition* **63**, e202409282 (2024).

71. J. A. Ciemniecki, D. K. Newman, The Potential for Redox-Active Metabolites To Enhance or Unlock Anaerobic Survival Metabolisms in Aerobes. *Journal of Bacteriology* **202**, e00797-00719 (2020).

72. S. Mak, J. R. Nodwell, Actinorhodin is a redox-active antibiotic with a complex mode of action against Gram-positive cells. *Molecular Microbiology* **106**, 597-613 (2017).

73. J. D. Coates, K. A. Cole, R. Chakraborty, S. M. O'Connor, L. A. Achenbach, Diversity and Ubiquity of Bacteria Capable of Utilizing Humic Substances as Electron Donors for Anaerobic Respiration. *Applied and Environmental Microbiology* **68**, 2445-2452 (2002).

74. E. E. Roden *et al.*, Extracellular electron transfer through microbial reduction of solid-phase humic substances. *Nature Geoscience* **3**, 417-421 (2010).

75. Y. Wang, S. E. Kern, D. K. Newman, Endogenous Phenazine Antibiotics Promote Anaerobic Survival of Pseudomonas aeruginosa via Extracellular Electron Transfer. *Journal of Bacteriology* **192**, 365-369 (2010).

76. X. Jin *et al.*, Sensitive bacterial V_m sensors revealed the excitability of bacterial V_m and its role in antibiotic tolerance. *Proceedings of the National Academy of Sciences* **120**, e2208348120 (2023).

77. R. Li, S. Bakshi, Quantitative Single-Cell Imaging of Efflux Pump Heterogeneity and Antibiotic Response Dynamics. *bioRxiv* 10.1101/2025.08.06.668869, 2025.2008.2006.668869 (2025).

78. W. Miran, W. Huang, X. Long, G. Imamura, A. Okamoto, Multivariate landscapes constructed by Bayesian estimation over five hundred microbial electrochemical time profiles. *Patterns* **3** (2022).

79. R. M. Shanks, N. C. Caiazza, S. M. Hinsa, C. M. Toutain, G. A. O'Toole, *Saccharomyces cerevisiae*-based molecular tool kit for manipulation of genes from gram-negative bacteria. *Appl Environ Microbiol* **72**, 5027-5036 (2006).

Chapter 4 High-diffusion redox cycling enhances metabolism and increases antibiotic sensitivity under a low-energy condition

4.1 Introduction

Bacterial metabolic states fundamentally shape how cells respond to antibiotics (1, 2). When energy and nutrients are abundant, bacteria upregulate metabolism to support growth, allowing metabolism-dependent antibiotics—such as aminoglycosides and fluoroquinolones—to efficiently kill cells by disrupting protein or DNA synthesis. However, under oxygen- or nutrient-limited conditions, bacteria minimize energy expenditure and enter a low-metabolic state, rendering these antibiotics ineffective (3, 4). Such energy-limited conditions are widespread in natural and clinical settings, including soils, hypoxic lung mucus, and the anaerobic cores of biofilms, posing a major obstacle to effective treatment (5-10).

Under energy-limited conditions, redox-active metabolites (RAMs) can act as alternative electron acceptors during metabolism, becoming reduced inside the cell and reoxidized extracellularly by external electron acceptors before re-entering the cell (11). This redox cycling allows RAMs to maintain intracellular redox balance and sustain metabolism (12, 13). Because redox cycling requires RAMs to repeatedly traverse the cell membrane, their physicochemical properties—which determine membrane permeability—play a crucial role. Although many studies have examined which physicochemical features most strongly influence membrane permeability (14-17), far fewer have considered how these properties affect a molecule's capacity to sustain redox cycling for metabolism. In particular, it remains unclear how membrane permeability contributes to RAM transport and thereby shapes metabolic flux under energy-limited conditions.

Previous evidence shows that membrane permeability directly governs the movement and intracellular retention of endogenous redox-active metabolites (RAMs). In *Pseudomonas aeruginosa*, genetically increasing outer-membrane porosity enhances the export of pyocyanin (PYO), demonstrating that diffusion through the outer membrane substantially contributes to its steady-state distribution (18). Conversely, loss of porins—such as deletion of OmpF in *Escherichia coli*—markedly reduces the permeation of small solutes by restricting diffusion across the outer membrane (19).

These findings led us to hypothesize that the membrane permeability of RAMs influences metabolic flux. Under energy-limited conditions, compounds with low membrane permeability may become constrained by efflux pump capacity or by slow membrane transit, thereby limiting metabolic flux. In contrast, diffusion-favored molecules can sustain higher fluxes because their transport does not encounter such bottlenecks. This diffusion-driven enhancement of metabolism may, in turn, reduce the antibiotic tolerance characteristic of low-energy states.

To test this hypothesis, we leveraged a high-throughput electrochemical platform that quantifies metabolic flux in non-growing *P. aeruginosa* under anoxic conditions. We first examined whether concentration-dependent metabolic activation influences antibiotic sensitivity, and then investigated how diffusion capability—serving as a proxy for membrane permeability—correlates with metabolic rate. Finally, we analyzed which physicochemical traits of RAMs govern their membrane permeability in *P. aeruginosa*. Together, these approaches reveal an alternative means to enhance antibiotic sensitivity under energy-limited conditions by stimulating metabolism with highly membrane-permeable molecules.

4.2 Results

4.2.1 PCN is PMF-limited while PYO is diffusion-driven in mediating anaerobic metabolism

In our previous work, we demonstrated that under energy-limited conditions, when phenazine-1-carboxamide (PCN) exceeded a threshold concentration, its metabolism became limited by efflux capacity, reflecting a pump-saturation bottleneck that, prevents further increases in metabolic rate in *P. aeruginosa*. Inspired by this observation, we next asked whether RAMs with different membrane permeability would exhibit distinct metabolic behaviors. To test this, we examined another endogenous electron shuttle produced by *P. aeruginosa*—pyocyanin (PYO). PYO is predicted to have higher membrane permeability than PCN, as it exhibits a lower topological polar surface area (TPSA) (20), fewer hydrogen-bond donors (fuji), and lower conformational flexibility (fewer rotatable bonds) (fuji) (Table 1). Based on these physicochemical differences, we hypothesized that PYO should sustain higher metabolic fluxes than PCN at elevated concentrations.

To address this, we applied the protonophore carbonyl cyanide m-chlorophenyl hydrazone (CCCP), a chemical uncoupler that dissipates the proton motive force (PMF), with a range of PCN/ PYO concentration (37.5, 75, 150, and 375 μM). Because PMF dissipation inhibits energy-dependent efflux while leaving passive diffusion unaffected, the metabolic flux of a metabolite that is diffusion-limited should remain unchanged in the presence of CCCP (21). These phenazines were tested in *P. aeruginosa* under anaerobic incubation at a poised potential (0 V vs. Ag/AgCl) with glucose as the electron donor. We first focused on the initial 24 hours of anaerobic incubation, during which cell viability remains largely unchanged (Figure 1A). This time window therefore provides a stable physiological state that allows us to examine the kinetic

response of electron shuttles without confounding effects from changes in population size. We observed a significant decrease in metabolic flux (read out as current) with PCN upon CCCP treatment, suggesting that PCN-redox cycling is strongly related to PMF (Figure 1B). In contrast, metabolic flux with PYO did not change with CCCP treatment, suggesting that PYO redox cycling is mediated by diffusion (Figure 1C). Together, these results suggest that PCN-mediated metabolism is constrained by PMF, while PYO-mediated metabolism proceeds largely through passive diffusion, revealing distinct transport bottlenecks that shape their metabolic fluxes.

To determine how these distinct transport bottlenecks influence metabolic rate and survival during a maintenance state, we performed 5-day electrochemical incubations with PCN and PYO across a range of concentrations (Figure 2A). Current output increased linearly with PYO concentration, and viability was maintained only at concentrations above 75 μM (Figure 2B), resulting in a 3.5-fold higher cell-specific metabolic rate at 375 μM compared to 75 μM (Figure 2B). Unlike PCN, which reached a plateau in metabolic rate at high concentrations, PYO supported continued increases in metabolic activity, indicating that its transport does not encounter the same capacity-limiting bottleneck during prolonged maintenance.

To test whether the elevated metabolic activity at high PYO concentrations reflects increased metabolic burden or simply highly efficient electron shuttling, we compared *Δphz* and *ΔphzΔmexS* strains under PYO exposure (Figure 2C). If the enhanced current at high PYO concentrations were driven by basal metabolic burden, the *ΔphzΔmexS* mutant—which experiences greater PMF drain due to efflux overexpression—should exhibit a further increase in metabolic flux. However, during long-term incubation, metabolic flux did not increase in the *ΔphzΔmexS* mutant at high PYO concentrations, indicating that flux at this regime is set by the electron-shuttle transport capacity rather than by basal metabolic burden.

In addition, based on the finding that the metabolic rate did not differ between *Δphz* and *ΔphzΔmexS* strains at 375 μM PYO but was significantly elevated at 75 μM, we hypothesized that drug sensitivity likewise be similar at 375 μM but reduced in *ΔphzΔmexS* at 75 μM. To test this, we measured day 5 survival in the presence of 75 or 375 μM PCN or PYO after adding ciprofloxacin following 1 day of anaerobic electrochemical incubation (Figure 2D). In contrast to PCN, where *ΔphzΔmexS* shows a higher metabolic rate than *Δphz* at high concentrations and thus exhibits altered drug sensitivity, no survival difference was observed between the two strains with PYO at 375 μM. However, at 75 μM, survival of Δ*phz*Δ*mexS* was significantly decreased compared to Δ*phz* in the presence of either PCN or PYO. These results further indicate that the link between metabolic activity and antibiotic sensitivity may be a general outcome under energy-limited conditions.

4.2.2 Metabolic rate controlled by RAM concentration determines antibiotic sensitivity

To further test whether metabolic activity underlies these differences in antibiotic sensitivity, we next examined sensitivity under conditions where the metabolic rate (read out as current output) was modulated by RAM concentration. We first used PCN and PYO, which exhibit distinct concentration-dependent current profiles. We focused on the initial 20 h, during which most cells remain viable, to capture the early metabolic activation phase before substantial cell death. Ciprofloxacin and tobramycin were selected because they primarily act on metabolically active cells (2). When exposed to ciprofloxacin, cell survival increased with RAM concentration (Figure 3A), whereas the opposite trend was observed with tobramycin (Figure 3B). This opposite pattern likely reflects efflux pump substrate specificity: phenazines induce the MexEF-OprN efflux system, for which ciprofloxacin is a substrate, leading to increased resistance at

higher phenazine concentrations (22). In contrast, tobramycin is primarily exported by MexXY-OprM, which is not induced by phenazines, explaining why tobramycin susceptibility did not change with phenazine-dependent efflux induction (23). Given this, we focused subsequent analyses on tobramycin to isolate the contribution of metabolic regulation from efflux induction. We found that tobramycin sensitivity increased with PYO and PCN concentration, with a more pronounced trend at high tobramycin levels. PYO showed stronger sensitization because its metabolic rate continued to rise at high concentrations, whereas PCN exhibited a metabolic plateau, resulting in a correspondingly weaker increase in sensitivity. We consider it unlikely that phenazine–antibiotic competition for efflux explains this sensitivity: pumps such as MexXY–OprM, which belong to the aminoglycoside-specific subfamily of RND transporters, are broadly associated with resistance to positively charged, highly polar antibiotics (23). These pumps are neither induced by phenazines nor reported to transport them (22, 24, 25), making phenazine–antibiotic competition for efflux mechanistically unlikely.

4.2.3 Membrane permeability of RAMs predicts metabolic rate *P. aeruginosa*

Since PYO and PCN have distinct physicochemical properties, with PYO predicted to have higher membrane permeability than PCN, this difference may explain their divergent metabolic rates at high concentrations. To test whether membrane permeability generally correlates with metabolic rate, we examined a broader panel of RAMs with 375 μM. We hypothesized that compounds with higher passive permeability would support higher metabolic rates.

To isolate the contribution of passive diffusion from active transport, we performed assays with and without CCCP. CCCP, a protonophore that dissipates the proton motive force (PMF), inhibits energy-dependent efflux and thereby approximates a passive-

diffusion condition. We therefore treated the current measured under CCCP as a proxy for membrane permeability. Although some molecules showed a marked decrease in current upon CCCP treatment, indicating that PMF-dependent process contributes to their export, permeability-associated current and total current remained strongly positively correlated ($R^2 = 0.88$, $r = +0.94$), indicating that membrane permeability contributes substantially to the overall metabolic rate supported by RAMs (Figure 4A). To further identify which physicochemical features govern permeability in *P. aeruginosa*, we plotted permeability-associated current against several descriptors, including molecular weight (MW), topological polar surface area (TPSA), number of rotatable bonds (molecular flexibility), hydrogen-bond donors (HBD), and calculated logP (MlogP, hydrophobicity) (Figure 4B-F). Current showed strong correlations with MlogP ($r = -0.71$) and the number of rotatable bonds ($r = -0.78$), and a moderate correlation with MW ($r = -0.57$), whereas correlations with TPSA and HBD were weak. These results indicate that hydrophobicity and molecular flexibility—rather than polarity—are the physicochemical features most strongly associated with passive permeability and thus diffusion-based export in *P. aeruginosa*.

4.3 Discussion

Bacterial low-metabolic states pose major challenges for antibiotic treatment. Here, we show that redox-active metabolites (RAMs) with high diffusion capability can enhance metabolic activity even under energy-limited conditions because their greater membrane permeability enables rapid transmembrane transport. Whereas PMF-dependent processes and low-permeability molecules become transport-limited at high substrate concentrations, passive diffusion by highly permeable RAMs remains unsaturated, supporting sustained metabolic activation. This mechanistic difference

explains the distinct aminoglycoside sensitivity patterns observed for PYO and PCN. PYO, with higher membrane permeability, continues to boost metabolic activity at higher concentrations and therefore enhances antibiotic killing. In contrast, PCN, which has lower membrane permeability and relies more heavily on PMF, exhibits a saturated metabolic rate at high concentrations and consequently shows weaker killing efficiency. Although aminoglycosides are known to primarily kill cells at the biofilm surface due to their high polarity, which limits penetration into the biofilm matrix (26, 27), we hypothesize that high levels of RAMs could reshape the biofilm matrix—consistent with recent findings that phenazine-dependent redox gradients remodel matrix architecture (28)—and thereby potentially influence antibiotic access to deeper layers. Future biofilm experiments will be required to verify this possibility.

In biofilms, phenazines segregate spatially: PYO is enriched in the outer layers (~70–80 μM), whereas PCN accumulates deeper in the matrix at substantially higher concentrations (~400 μM) (29, 30). Despite this difference, our measurements show that PCN at 375 μM supports a similar cell-specific metabolic rate to PYO at 75 μM, indicating that biofilm-layer–specific fluxes may be comparable even when local concentrations differ by several fold. Although we used a planktonic electrochemical system to estimate metabolic rates, this approach remains physiologically relevant because prior work shows that oxidized PYO is retained by the eDNA matrix, whereas reduced PYO—and PCN, which binds eDNA only weakly—diffuse readily through biofilms (29). Since reduced phenazines do not substantially accumulate extracellularly in biofilms, their export is not limited by matrix retention. This supports the idea that our electrochemical system, which continuously removes reduced phenazines at the electrode, recapitulates the in-situ transport dynamics of biofilms, where reduced phenazines likewise remain freely diffusible.

At supraphysiological PYO (well above biofilm levels), membrane diffusion is likely to dominate: efflux overexpression and CCCP no longer change metabolic flux. Interestingly, this result differs from previous reports showing that efflux pumps such as MexGHI-OpmD contribute to PYO export, and that loss of this system leads to intracellular PYO accumulation and increased sensitivity (18). Although those studies did not explicitly distinguish the redox state of PYO, their experiments were carried out under aerobic conditions in which oxidized PYO is expected to predominate and to drive oxidative stress. By contrast, the current that we measured under anaerobic electrochemical conditions is generated primarily by the reduced form of PYO, which is substantially less toxic. The lack of a CCCP effect on PYO-mediated current therefore indicates that reduced PYO is exported largely by passive diffusion, even though oxidized PYO can be an efflux substrate in other physiological regimes.

Correlation analysis across multiple RAMs using diffusion-only current (CCCP condition) allowed us to examine membrane permeability without interference from PMF-dependent processes, which preferentially transport substrates with physicochemical properties distinct from those that passively diffuse. For example, small and hydrophilic molecules such as C_4–C_6 acyl-HSLs diffuse readily across membranes, whereas larger or more hydrophobic analogs like C_{12} show poor passive permeability and therefore rely heavily on efflux-mediated export (31). Consistent with this pattern, our analysis revealed that hydrophobicity and molecular flexibility—both negatively correlated with diffusion-associated current—are key structural determinants governing passive diffusion across the *P. aeruginosa* membrane. These findings explain why highly permeable compounds such as PYO can sustain redox cycling even when PMF or efflux capacity becomes limiting.

Together, these results identify membrane permeability as the primary determinant linking RAM structure to metabolic rate and antibiotic susceptibility under energy-

limited conditions. By establishing how physicochemical properties control transport mechanisms and metabolic flux, this work provides a conceptual framework for understanding how RAMs modulate antibiotic sensitivity in *P. aeruginosa*.

4.4 Methods and materials

Microbial Growth Conditions and Reagents

All *Pseudomonas aeruginosa* UCBPP-PA14 strains were revived from –80 °C glycerol stocks and streaked onto LB agar, followed by overnight incubation at 37 °C. Plates were stored at 4 °C and used within one week to inoculate liquid cultures. For liquid culture preparation, cells were grown in 7 mL LB in glass culture tubes (Iwaki, 61-9718-32) at 37 °C with shaking at 250 rpm on a slanted rack for 20 h, yielding a final OD500 of ~6.

Anaerobic Survival Assay Using a 96-Well Electrochemical Potentiostat

Starter cultures were centrifuged and washed twice with minimal medium (MM; 100 mM MOPS pH 7.2, 43 mM NaCl, 93 mM NH_4Cl, 3.7 mM KH_2PO_4, 1 mM $MgSO_4$). Cells were then concentrated to OD 75 and transferred into an anaerobic Coy chamber (33 °C, 1–2% H_2). A 96-well screen-printed electrode plate containing carbon working/counter electrodes and an Ag/AgCl reference electrode (88) was prepared. Ten microliters of culture (diluted beforehand to OD 15 in N_2-sparged MM) was added to each well with 190 µL N_2-sparged MM supplemented with 20 mM glucose, 3.6 µM $FeSO_4$, and PCN or PYO at 7.5, 37.5, 75, 150, 225 or 375 µM (2.5% DMSO). Wells were sealed with a slit seal (BioChromato) plus an aluminum seal (DiversifiedBiotech) to minimize evaporation. Plates were incubated at 33 °C without shaking in a custom 96-channel potentiostat at 0 mV vs Ag/AgCl. On Days 1, 3, 5, the aluminum seal was removed, wells were mixed by pipetting, and 10 µL was collected for CFU counting. Wells were resealed and returned to the chamber. All plasticware used inside the chamber was pre-degassed for ≥ 3 days.

Colony Forming Unit (CFU) Assay

Cells were serially diluted in PBS prior to plating. Dilutions spanning 5–6 logs were prepared, and 5 µL from each dilution was spotted on LB agar, followed by overnight incubation at 37 °C. All Day 1 CFU procedures (dilution, spotting, incubation) were performed aerobically. For Days 3 and 5, all steps were performed anaerobically: PBS was N_2-sparged for ≥ 30 min, and all plasticware and LB plates were pre-equilibrated in the Coy chamber for ≥ 2 days.

Antibiotic Survival Assay

Under anaerobic electrochemical conditions, ciprofloxacin (0.4 and 10 mg/mL in 0.1 M HCl), and tobramycin (each 4 and 80 mg/mL in MM) were added to wells on day 0. One microliter of antibiotic solution was mixed into each well, and 10 µL samples were collected for CFU enumeration after 24-hour incubation. PCN or PYO was supplied at 75, 150, 262 or 375 µM.

CCCP experiment

Before the addition of RAMs (final concentration 375 µM), CCCP was added to each well at final concentrations of 50 µM (with 3% DMSO as the solvent). The cultures were incubated with CCCP for 15 minutes at 33 °C. RAM was then added to reach the final concentration, the wells were mixed thoroughly, and electrochemical incubation was initiated. All procedures were performed under anaerobic conditions within the Coy chamber. All stocks of RAMs (30mM) were dissolved in DMSO.

4.5 Figures

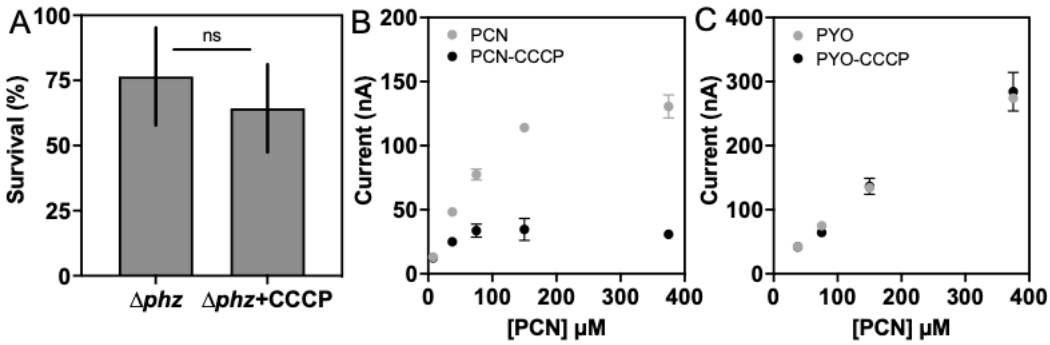


Figure 1. PCN-mediated metabolism is PMF-limited, whereas PYO is diffusion-driven.

(A) Survival of *Δphz* cells after 24 h anaerobic electrochemical incubation with or without CCCP.
(B) Current output from *Δphz* cells supplied with increasing PCN concentrations in the presence or absence of CCCP.
(C) Current output from *Δphz* cells supplied with increasing PYO concentrations under the same conditions.
Current values were averaged over days 0-1. Data represent mean ± SD from four technical replicates.

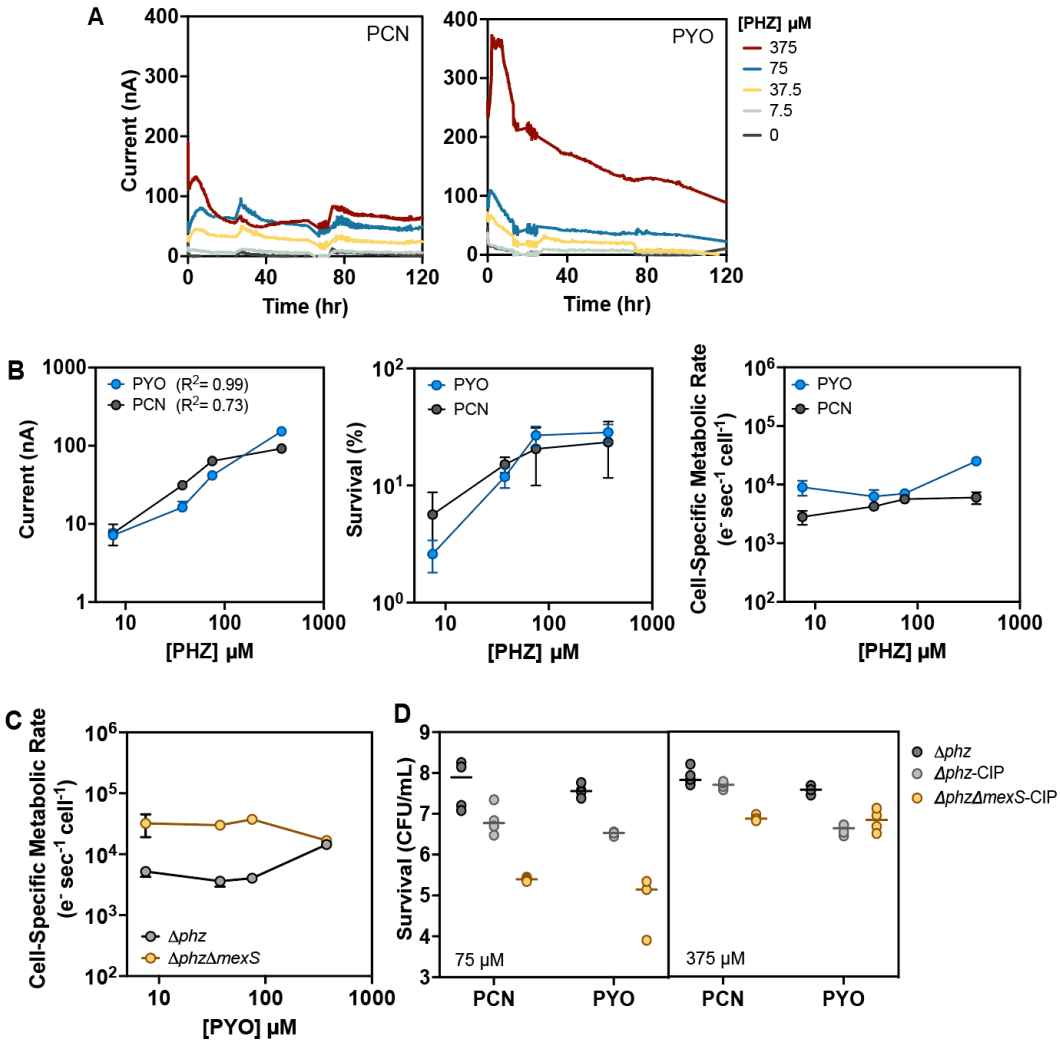


Figure 2. Distinct transport constraints determine metabolic flux and antibiotic sensitivity during long-term maintenance

(A) Mean current generated by Δ*phz* strain with varying concentrations of PYO or PCN over days 1–5. Data represent four biological replicates.

(B) Current output (left), survival (middle), and cell-specific metabolic rate (right) during 5 days of anaerobic electrochemical incubation in glucose minimal medium with varying concentrations of PYO or PCN. Current values are averaged over days 1–5; survival represents the geometric mean of CFU counts from days 1–5. Data represent mean ± SD from at least four biological replicates. 100% survival corresponds to approximately 5×10^8 CFU mL^{-1}.

(C) Cell-specific metabolic rate of *Δphz* and *ΔphzΔmexS* strains during days 1–5 of anaerobic incubation across various PYO concentrations.

(D) Day 5 survival of *Δphz* and *ΔphzΔmexS* strains under anaerobic conditions with 75 or 375 µM PCN or PYO. Ciprofloxacin (10 µg/mL) was added after 1 day of anaerobic electrochemical incubation. Data represent at least four biological replicates.

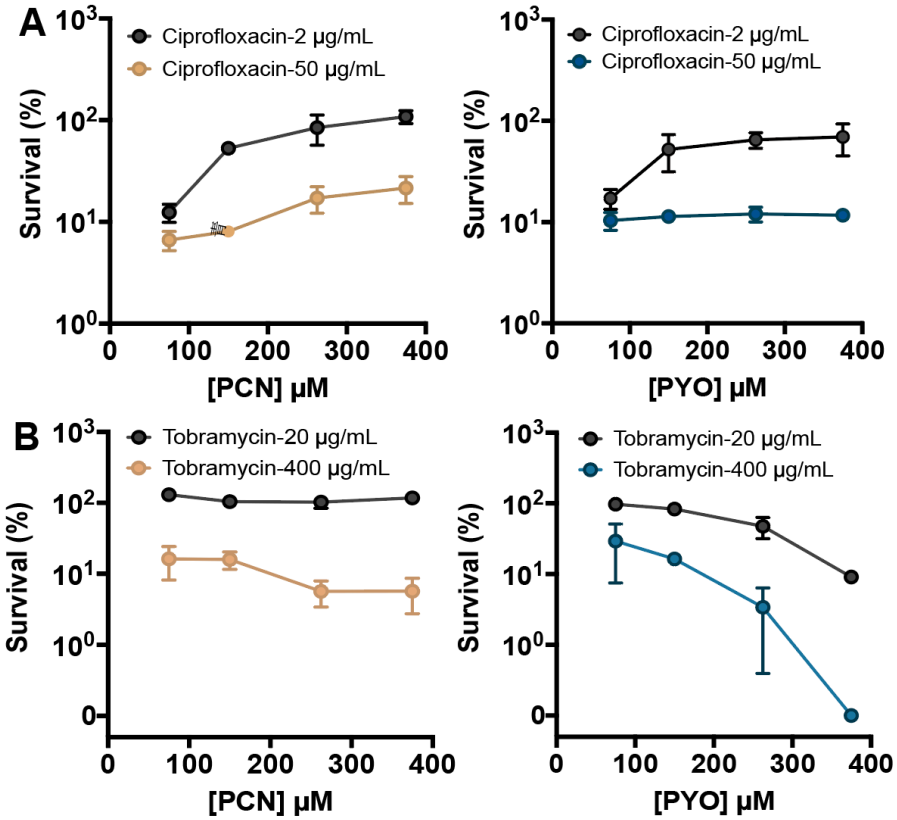


Figure 3. Concentration-driven metabolic activation reveals opposing sensitivity patterns to ciprofloxacin and tobramycin.

(A) Survival of Δ*phz* cells exposed to ciprofloxacin (2 or 50 µg/mL) after one day anaerobic electrochemical incubation with increasing concentrations of PCN or PYO. (B) Survival of *Δphz* cells exposed to tobramycin (20 or 400 µg/mL) under the same conditions.
Data represent mean ± SD from three technical replicates.

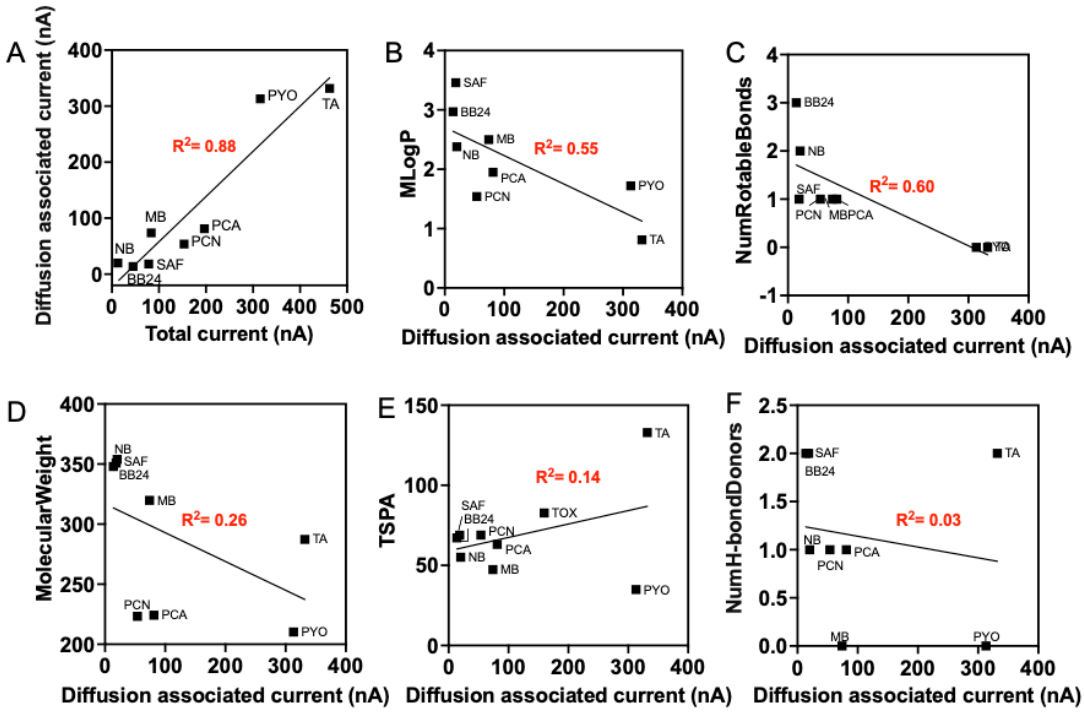


Figure 4. Membrane permeability predicts RAM-mediated metabolic rate in *P. aeruginosa*.

(A) Correlation between total current and diffusion-associated current (measured under CCCP), showing that passive permeability strongly contributes to overall metabolic rate supported by redox-active metabolites (RAMs) ($R^2 = 0.88$).

(B–F) Diffusion-associated current plotted against physicochemical descriptors of each RAM:

(B) calculated logP (MlogP),

(C) number of rotatable bonds,

(D) molecular weight,

(E) topological polar surface area (TPSA), and

(F) number of hydrogen-bond donors (HBD).

Current values were averaged over days 0-1. Data represent mean ± SD from four technical replicates.

4.6 Table

Table 1. Physiochemical properties of PYO and PCN

	PYO_{ox}	PYO_{red}	PCN_{ox}	PCN_{red}
SMILES	CN1C2=CC=CC=C2N=C3C1=CC=CC3=O	CN1C2=C(NC3=C1C=CC=C3O)C=CC=C2	C1=CC=C2C(=C1)N=C3C=CC=C(C3=N2)C(=O)N	NC(=O)C1=CC=CC2=C1NC1=C(N2)C=CC=C1
TPSA	34.89	40.95	68.87	74.67
H-bond donor	0	2	1	3
Rotatable bond	0	0	1	1

TPSA, topological polar surface area. Log $P_{o/w}$, octanol–water partition coefficient.

Data were obtained from the SwissADME online tool (http://www.swissadme.ch)

4.7 References

1. J. M. Stokes, A. J. Lopatkin, M. A. Lobritz, J. J. Collins, Bacterial Metabolism and Antibiotic Efficacy. *Cell Metabolism* **30**, 251-259 (2019).
2. M. A. Lobritz *et al.*, Antibiotic efficacy is linked to bacterial cellular respiration. *Proceedings of the National Academy of Sciences* **112**, 8173-8180 (2015).
3. J. A. Ciemniecki, C.-L. Ho, R. D. Horak, A. Okamoto, D. K. Newman, Mechanistic study of a low-power bacterial maintenance state using high-throughput electrochemistry. *Cell* **187**, 6882-6895.e6888 (2024).
4. C. P. Kempes *et al.*, Drivers of Bacterial Maintenance and Minimal Energy Requirements. *Frontiers in Microbiology* **Volume 8 - 2017** (2017).
5. W. L. Silver, A. E. Lugo, M. Keller, Soil oxygen availability and biogeochemistry along rainfall and topographic gradients in upland wet tropical forest soils. *Biogeochemistry* **44**, 301-328 (1999).
6. E. M. Lacroix, R. J. Rossi, D. Bossio, S. Fendorf, Effects of moisture and physical disturbance on pore-scale oxygen content and anaerobic metabolisms in upland soils. *Science of The Total Environment* **780**, 146572 (2021).
7. E. S. Cowley, S. H. Kopf, A. LaRiviere, W. Ziebis, D. K. Newman, Pediatric Cystic Fibrosis Sputum Can Be Chemically Dynamic, Anoxic, and Extremely Reduced Due to Hydrogen Sulfide Formation. *mBio* **6**, 10.1128/mbio.00767-00715 (2015).
8. D. Worlitzsch *et al.*, Effects of reduced mucus oxygen concentration in airway Pseudomonas infections of cystic fibrosis patients. *The Journal of Clinical Investigation* **109**, 317-325 (2002).
9. K. D. Xu, P. S. Stewart, F. Xia, C.-T. Huang, G. A. McFeters, Spatial Physiological Heterogeneity in *Pseudomonas aeruginosa* Biofilm Is Determined by Oxygen Availability. *Applied and Environmental Microbiology* **64**, 4035-4039 (1998).
10. D. de Beer, P. Stoodley, F. Roe, Z. Lewandowski, Effects of biofilm structures on oxygen distribution and mass transport. *Biotechnology and Bioengineering* **43**, 1131-1138 (1994).

11. N. R. Glasser, S. H. Saunders, D. K. Newman, The Colorful World of Extracellular Electron Shuttles. *Annual Review of Microbiology* **71**, 731-751 (2017).

12. J. A. Ciemniecki, D. K. Newman, NADH dehydrogenases are the predominant phenazine reductases in the electron transport chain of Pseudomonas aeruginosa. *Molecular Microbiology* **119**, 560-573 (2023).

13. N. R. Glasser, S. E. Kern, D. K. Newman, Phenazine redox cycling enhances anaerobic survival in *Pseudomonas aeruginosa* by facilitating generation of ATP and a proton-motive force. *Molecular Microbiology* **92**, 399-412 (2014).

14. X. Liu, B. Testa, A. Fahr, Lipophilicity and Its Relationship with Passive Drug Permeation. *Pharmaceutical Research* **28**, 962-977 (2011).

15. L. Di *et al.*, The Critical Role of Passive Permeability in Designing Successful Drugs. *ChemMedChem* **15**, 1862-1874 (2020).

16. J. Mehla *et al.*, Predictive Rules of Efflux Inhibition and Avoidance in Pseudomonas aeruginosa. *mBio* **12**, 10.1128/mbio.02785-02720 (2021).

17. I. V. Leus *et al.*, Property space mapping of Pseudomonas aeruginosa permeability to small molecules. *Scientific Reports* **12**, 8220 (2022).

18. D. Wolloscheck, G. Krishnamoorthy, J. Nguyen, H. I. Zgurskaya, Kinetic Control of Quorum Sensing in Pseudomonas aeruginosa by Multidrug Efflux Pumps. *ACS Infectious Diseases* **4**, 185-195 (2018).

19. X. Liu, T. Ferenci, Regulation of Porin-Mediated Outer Membrane Permeability by Nutrient Limitation in Escherichia coli. *Journal of Bacteriology* **180**, 3917-3922 (1998).

20. J. Fernandes, C. R. Gattass, Topological Polar Surface Area Defines Substrate Transport by Multidrug Resistance Associated Protein 1 (MRP1/ABCC1). *Journal of Medicinal Chemistry* **52**, 1214-1218 (2009).

21. T. D. Davis, C. J. Gerry, D. S. Tan, General Platform for Systematic Quantitative Evaluation of Small-Molecule Permeability in Bacteria. *ACS Chemical Biology* **9**, 2535-2544 (2014).

22. L. A. Meirelles, E. K. Perry, M. Bergkessel, D. K. Newman, Bacterial defenses against a natural antibiotic promote collateral resilience to clinical antibiotics. *PLOS Biology* **19**, e3001093 (2021).

23. L. G. Kavanaugh, M. E. Hinrichsen, C. M. Dunham, G. L. Conn, Regulation, structure, and activity of the *Pseudomonas aeruginosa* MexXY efflux system. *Antimicrobial Agents and Chemotherapy* **69**, e01825-01824 (2025).

24. N. Masuda *et al.*, Substrate Specificities of MexAB-OprM, MexCD-OprJ, and MexXY-OprM Efflux Pumps in Pseudomonas aeruginosa. *Antimicrobial Agents and Chemotherapy* **44**, 3322-3327 (2000).

25. L. G. Kavanaugh, S. M. Hariharan, G. L. Conn, Determination of Pseudomonas aeruginosa MexXY-OprM substrate profile in a major efflux knockout system reveals distinct antibiotic substrate classes. *Microbiology Spectrum* **13**, e02903-02924 (2025).

26. M. C. Walters, F. Roe, A. Bugnicourt, M. J. Franklin, P. S. Stewart, Contributions of Antibiotic Penetration, Oxygen Limitation, and Low Metabolic Activity to Tolerance of *Pseudomonas aeruginosa* Biofilms to Ciprofloxacin and Tobramycin. *Antimicrobial Agents and Chemotherapy* **47**, 317-323 (2003).

27. P. Meers *et al.*, Biofilm penetration, triggered release and in vivo activity of inhaled liposomal amikacin in chronic Pseudomonas aeruginosa lung infections. *Journal of Antimicrobial Chemotherapy* **61**, 859-868 (2008).

28. C. R. Evans *et al.*, Spatial heterogeneity in biofilm metabolism elicited by local control of phenazine methylation. *Proceedings of the National Academy of Sciences* **120**, e2313208120 (2023).

29. S. H. Saunders *et al.*, Extracellular DNA Promotes Efficient Extracellular Electron Transfer by Pyocyanin in *Pseudomonas aeruginosa* Biofilms. *Cell* **182**, 919-932.e919 (2020).

30. K. T. Schiessl *et al.*, Phenazine production promotes antibiotic tolerance and metabolic heterogeneity in *Pseudomonas aeruginosa* biofilms. *Nature Communications* **10**, 762 (2019).

31. P. Pearson James, C. Van Delden, H. Iglewski Barbara, Active Efflux and Diffusion Are Involved in Transport of Pseudomonas aeruginosa Cell-to-Cell Signals. *Journal of Bacteriology* **181**, 1203-1210 (1999).

Chapter 5 Osmium-grafted Magnetic Nanobeads Improve Microbial Current Generation via Culture-free and Quick Enrichment of Electrogenic Bacteria

Citation and copyright notice

This chapter is based on work previously published as:

Ho, C. L., Emran, M. Y., Ihara, S., Huang, W., Wakai, S., Li, W. P., & Okamoto, A. (2023). Osmium-grafted magnetic nanobeads improve microbial current generation via culture-free and quick enrichment of electrogenic bacteria. ***Chemical Engineering Journal***, 466, 142936.

https://doi.org/10.1016/j.cej.2023.142936

© 2023 Elsevier.

This chapter includes material adapted from the author-accepted manuscript of the above article. According to Elsevier's Thesis Reuse Policy, authors are permitted to incorporate the accepted manuscript version of their published work into a thesis or dissertation provided that proper citation and acknowledgment are included. The final, published version of the article is available on the publisher's website at the DOI listed above.

5.1 Introduction

Chapters 2 and 3 establish that *Pseudomonas aeruginosa* survives under anaerobic, energy-limited conditions by sustaining extracellular electron transfer (EET) through redox-active metabolites and export systems. Because EET is also used by well-known environmental electroactive bacteria such as *Shewanella* and *Geobacter*, these mechanistic findings indicate that EET is not a species-specific phenomenon but a broadly conserved survival strategy in low-energy environments. This understanding naturally raises an ecological question: how widespread are EET-dependent survival mechanisms in environmental microbial communities, and which bacterial taxa are particularly capable of thriving under anaerobic, energy-limited conditions? The osmium-grafted magnetic nanobead enrichment method described in Chapter 5 was developed to address this question. By selectively isolating cells that exhibit strong surface redox activity—a phenotypic indicator of potential EET capability—this method provides a means to identify electroactive bacteria that can outcompete others under oxygen-limited conditions. In doing so, it extends the mechanistic insights gained from *P. aeruginosa* to a community context, providing ecological insight into how EET shapes survival and competitiveness in natural microbial assemblages.

Microbial electrochemical technologies (METs) are emerging environmental biotechnologies in which electroactive bacteria perform electrode catalysis coupled with interfacial electron transfer, referred to as extracellular electron transfer (EET) (1-3). Thus, EET-capable bacteria have been applied in numerous biotechnological applications such as in microbial fuel cells (MFCs), bioremediation of environmental pollutants and metal recovery, chemical production, and biosensors (1, 4, 5). Remarkable progress has been made in understanding the biological interactions between nanomaterials and model electrogenic bacteria such as *Shewanella* and

Geobacter (6-8), supporting the potential of using METs with highly durable, low cost, and highly efficient processes compared with conventional chemical and environmental processes for sustainable energy and carbon neutrality. However, METs mainly rely on mixed bacterial cultures, which are typically obtained from natural environments such as soil or sewage sludge. Therefore, the bioelectrocatalytic activity depends largely on the number of electrogenic bacteria, which requires that the number of inactive or suppressing bacteria is minimized in this system (9). Transfer of a pre-incubated bacterial consortium (as an inoculum) from an operating electrode to a new electrode is a common strategy for improving power generation; however, constructing and running the reactor for the pre-enrichment process takes at least a few weeks (10, 11). Therefore, in the present study, we are urged to develop a quick method for enriching electrogenic bacteria.

Redox-dependent 3,3′-diaminobenzidine (DAB) polymerization is commonly used to stain electron transfer enzymes on the surface of electrogenic bacteria cells by conjugating them with heavy metals such as osmium and cobalt, thereby resulting in dark contrast in transmission electron microscopy (TEM) imaging (12, 13). This specific interaction proceeds as a function of the heme iron center in *c*-type cytochrome, which activates DAB oxidation, with further cross-linking aided by the oxidant hydrogen peroxide (14, 15). Cell-surface enzymes with heme iron centers are commonly observed in environmental electrogenic bacteria; approximately ten different cytochrome genes have been proposed in both iron-reducing and iron-oxidizing bacteria (16). Moreover, DAB staining in electrogenic bacteria has been reported even in the absence of cytochrome genes (17). Therefore, efficient catalysis of DAB polymerization on the cell surface may be specific to electrogenic bacteria and thus can be used to enrich bacteria from the environment without culture or MFC construction. Magnetic nanoparticles (MNPs) with uniform surface characteristics have

been used for capturing bacteria, which i) display good controllability in terms of particle size during preparation (18, 19), ii) high feasibility for functionalized surface features by using various chemical modification methods (20-22), and iii) strong magnetic properties for a rapid kinetic response in solution because of the remote magnet operation (23, 24). Jin *et al.* functionalized MNPs *via* surface modification with amino acids, which displayed rapid and efficient capture of both the gram-positive and gram-negative bacteria *Bacillus subtilis* and *Escherichia coli*, respectively (25). Sung *et al.* synthesized antibody-modified magnetic nanocomposites to capture *Staphylococcus aureus* in milk, achieving a capture efficiency of 75% because of the specific binding between the antibody and *S. aureus* (26). Therefore, separation using functionalized MNPs is a promising strategy for isolating electrogenic bacteria.

In the present study, we developed a rapid method for enriching electrogenic bacteria (within 30 min) to enhance microbial current production without additional electrochemical incubation. As the DAB polymer binds strongly with OsO_4 (27, 28), folic acid (FA) was used to conjugate the MNPs using OsO4 as a linker to form Os-exposed MNPs (Scheme 1A) (29, 30). To assess the selectivity of these MNPs for electrogenic bacteria (Scheme 1B), Shew*anella oneidensis* MR-1 was used (with outer-membrane cytochromes, OMCs) as EET-capable bacteria, whereas *E. coli* (without OMCs) was used as the negative control. The optimized magnetic separation conditions were applied to enrich electrogenic bacteria from an environmental sample, after which 16S rRNA analysis and electrochemical assay were performed. Direct enrichment of electrogenic bacteria without costly culturing processes may improve the efficiency of power generation in MFCs.

5.2 Results

5.2.1 Synthesis and characterization of Os-exposed nanobeads

A simple process was designed for preparing Os-exposed nanobeads (**Scheme 1A**). Briefly, commercial MNPs were used as the starting material and subjected to two surface modification reactions. First, the functional groups of carboxylic acid on FA have a strong affinity for the metal ion; thus, FA easily chelated bare iron on the nanobead surface to form FA-modified nanobeads (M@FA NPs) (31). Second, M@FA NPs were conjugated with OsO_4 to produce Os-exposed nanobeads (M@FA-Os NPs). FT-IR was performed to analyze the surface functional groups in each stage of material preparation (Figure 1A). Three spectra showed the same band at 580–640 cm^{-1}, which corresponded to the stretching vibration of Fe-O, suggesting the presence of iron oxide. After modifying FA onto the surface of MNPs, we observed additional FT-IR vibration bands, including C-H stretching at 2974 cm^{-1}, N-H bending and C=O stretching at 1600–1700 cm^{-1}, and N-H and O-H stretching at 3300–3500 cm^{-1}. In the sample of M@FA-Os NPs, the signal of N-H bending at 1620–1630 cm^{-1} disappeared, and the peak of N-H stretching at approximately 3500 cm^{-1} was reduced, suggesting changes in the bonding of N-H within the structure of FA, and H atoms were replaced by Os during modification of M@FA NP by OsO_4. New peaks at 1000–1300 cm^{-1} appeared for M@FA-Os NPs, assignable to the vibration signal of Os=N bonding appeared at 1000–1300 cm^{-1} (32). These results suggest that the deprotonation of N-H and coordination bonding occurred between folic acid and OsO_4.

To further detect binding between Os and FA, the peak intensity at the 580 cm–1 band assigned to the Fe-O mode of MNPs was normalized in each spectrum, and the spectrum of M@FA NPs was subtracted from the FT-IR spectrum of M@FA-Os and M/Os NPs (Figure 1B). The FT-IR spectrum of M@FA-Os NPs minus that of M@FA

NPs revealed observable signals at 1051 and 1089 cm–1, which corresponded to the stretching of Os=N (Figure 1B, red line) (32). No signals for Os=N bonding were obtained in the group without FA [mixed powder of MNPs with OsO4 (MNP/Os)], indicating that the remaining peaks at 1157, 1211, 1238, 2850, and 2920 cm–1 corresponded to the vibration of Os=O (Figure 1B, black line) (33). X-ray photoelectron spectroscopy (XPS) was conducted to confirm the bonding model of FA-Os-DAB. Direct comparison of M@FA-Os and M@FA NPs revealed no significant shift in the binding energy in Fe 2p, O 1s, and N 1s, and the signal of Os in 4f was completely shielded because of overlap with the intense signal of Fe in 3p (Figure S1), which was contributed by iron (II,III) of MNPs (34). Therefore, a 1:1 stoichiometric mixture of FA and OsO4 without MNPs was found to be feasible for testing FA-Os coordination. Upon normalizing to C peak in 1s at 284.8 eV in the samples of FA and FA-Os, peaks were observed for Os in 4f at 51.6 and 54.4 eV (Figure 1C). Additionally, the peak of N in 1s shifted from 399.5 to 399.9 eV (+0.4 eV) in the presence of OsO4, a differentiated peak of N=Os at 401.7 eV emerged, and the N-H peak at 398.8 eV decreased by approximately 4.4% comparing to the sample of FA, as analyzed using CASAXPS software (Figure 1D) (35), suggesting that N=Os bonds formed between FA and OsO4. X-ray diffraction measurement was performed to analyze the composition and crystal structure of the M@FA-Os NPs (Figure 1E). Six X-ray diffraction peaks were observed and centered at 2θ of 30.35, 35.57, 43.31, 53.73, 57.19, and 62.80, which corresponded to reflections of the (220), (311), (400), (422), (511), and (440) planes, respectively, of the Fe3O4 crystal with a cubic spinel structure. The diffraction patterns did not differ between M@FA-Os NPs and the original MNPs (JCPDS no. 19-629), suggesting that the composition was not changed by surface modification. Moreover, the structural morphology and particle size of M@FA-Os NPs were confirmed using high-resolution TEM. The morphology of M@FA-Os NPs, with

an irregular cubic platelet shape and sizes of 20–50 nm, was identical to that of the original MNPs (Figure 1F and S2). High-resolution TEM imaging of single M@FA-Os NP revealed obvious lattice fringes, with the d spacing calculated to be approximately 0.25 nm; this result agrees well with the orientation of Fe3O4 (311) (Figure 1F). These results suggest that the morphology, size, composition, and fundamental properties of MNPs were the same before and after surface modification.

5.2.2 Capture of DAB-polymerized bacteria using M@FA-Os NPs

To examine whether the synthesized M@FA-Os NPs can specifically capture bacteria capable of polymerizing DAB, we performed TEM using a pair of model bacterial strains: EET-capable *S. oneidensis* MR-1 and EET-deficient bacteria *E. coli* K12. Because of the large number of cytochromes on the surface of MR-1, DAB can easily react to form a DAB polymer, even without the addition of an oxidant. The surface of *S. oneidensis* MR-1 with DAB polymerization was clearly stained with OsO4, showing a dark edge in the images (Figure 2A). *Shewanella oneidensis* MR-1 without and *E. coli* K12 with DAB polymerization did not show clear contrast at the cellular edge (Figure 2B-C), indicating that *E. coli* K12 has a much lower ability to polymerize DAB compared to *S. oneidensis* MR-1 with OMCs. Consistently, the application of M@FA-Os NPs to DAB polymer-coated *S. oneidensis* MR-1 (PDAB@MR-1) led to the significant localization of M@FA-Os NPs at the cell surface using the optimized magnetic isolation step (Figure 2D). The aggregated particles of M@FA-Os NPs outlined the outer surface of a single cell of PDAB@MR-1, suggesting active interactions and selective binding of M@FA-Os NPs on the outer surface of DAB-stained EET-capable bacteria (Figure 2E). In contrast, we did not detect the localization of M@FA-Os NPs aggregated on the bacterial surface for *E. coli* K12 treated with a rigorous washing process (Figure 2F). These data demonstrate that a linkage formed

between M@FA-Os NPs and the DAB polymer deposited on the cell surface of *S. oneidensis* MR-1. Direct conjugation of FA-Os and DAB polymer was examined without MNPs. The Os 4f signal did not greatly change in position and intensity compared to those of FA-Os and FA-Os-DAB, demonstrating stable coordination between FA and Os after the reaction with DAB polymer (Figure 2G). The O 1s signal from FA-Os significantly shifted from 531.5 to 532.1 (+0.6 eV), and the peak width broadened after DAB polymer addition, resulting in a peak intensity increase and decrease assignable to O-C and O=Os bonding, respectively (Figure 2H). Because the peak shift in the binding energy suggests a transition from a double to single bond in O 1s (36), an O-C bond likely formed between FA-Os and DAB polymer via alkene oxidation, which typically occurs in OsO_4 and alkene reactions (37). These data confirm that FA-Os are paired with DAB to form stable and specific linkages between Os-exposed nanobeads and DAB-coated bacteria.

To identify the optimized conditions for magnetic isolation, we examined various buffer solutions with different pH values and ionic strengths to minimize the surface charge-induced non-specific association between the nanobeads and bacteria, which is evaluated by the bacterial protein concentration. First, we adjusted the pH and ionic strength of the washing buffer solution to reduce the non-specific adhesion of nanobeads on the bacterial surface (0.5 M NaCl, pH 9) and enhance the specificity of DAB-coated *S. oneidensis* MR-1. However, no significant improvement in reversing the non-specific adhesion of nanobeads to *E. coli* K12 was observed (Figure 3A–B). In contrast, non-specific binding between the nanobeads and DAB-polymerized *E. coli* K12 ($p < 0.001$) and *S. oneidensis* MR-1 ($p < 0.01$) was significantly inhibited by using a neutral binding solution with an ionic strength of 0.005 M (Figure 3C). The zeta potential of M@FA-Os NPs significantly changed from positive (~+0.25 mV) to negative (~-0.35 mV). As the bacteria surface has a negative charge, there was no

electrostatic interaction between M@FA-Os NPs and bacteria (Figure 3D). The protein concentration of each sample after the optimized magnetic isolation corresponded with the differences in interactions between the nanobeads and various bacteria observed in TEM images (Figure 2D-F).

When DAB-coated *S. oneidensis* MR-1 were magnetically isolated using M@FA-Os NPs under the optimized binding and washing buffer solutions, a >20-fold higher protein concentration was obtained as compared to that obtained when isolating DAB-polymerized *E. coli* K12 ($p < 0.001$, data not shown). The concentrations of captured protein from DAB-coated *S. oneidensis* MR-1 *versus* DAB-polymerized *E. coli* K12 using other nanobead types, including M@FA-Co NPs, M@FA NPs, M/Os NPs, and MNPs, were significantly lower than that obtained using M@FA-Os NPs ($p < 0.0001$) (Figure 4A). These results indicate that binding between the FA-osmium-DAB polymer is highly specific for *S. oneidensis* MR-1. For example, the non-covalent coordination pair between cobalt ion and FA was relatively unstable compared to that observed under the FA-Os condition, although $CoCl_2$ is used as a tracer agent for DAB staining (38). This unstable interaction led to unsatisfactory capture in the M@FA-Co NP group. We further evaluated the relative efficiency of enrichment using DAB-coated and original *S. oneidensis* MR-1 under the same conditions as used in magnetic isolation (Figure 4B). As expected, more protein was obtained from DAB-coated *S. oneidensis* MR-1 than from the original *S. oneidensis* MR-1 ($p < 0.01$, data not shown). A result was consistent with the result of DAB-coated *S. oneidensis* MR-1 *versus* DAB-polymerized *E. coli* K12 when using other types of nanobeads, showing reduced enrichment of DAB-coated *S. oneidensis* MR-1 ($p < 0.001$) and supporting that the Fe-FA-Os-DAB linkage is essential for specifically capturing EET-capable bacteria.

Enrichment of *S. oneidensis* MR-1 from a two-in-one solution (*S. oneidensis* MR-1 and *E. coli* K12) subjected to a DAB polymerization reaction was demonstrated in an

electrochemical assay. Significantly more electricity was produced by the EET-capable strain than by the EET-deficient strain (Figure 4C). Upon adding DAB working solution to the two-in-one bacterial solution, DAB polymer was generated and then deposited on the surface of *S. oneidensis* MR-1. These DAB-coated microbial cells were further enriched using the M@FA-Os NP-mediated magnetic isolation process and inoculated in LB medium until the OD_{600} reached 1.0 and removed most nanobeads. In the electrochemical measurement, the microbial current production (I_c) from the enriched sample increased significantly compared to that in the original two-in-one bacterial solution. This was attributed to the ratio of *S. oneidensis* MR-1 to *E. coli* K12 which increased after DAB-labeled magnetic separation (Figure 4D). Although the enriched sample contained a minority of *E. coli* K12 due to an unavoidable non-specific adhesion during the conjugation step, and *E. coli* K12 grew faster than *S. oneidensis* MR-1 under aerobic LB conditions at 30°C (Figure S3), the earlier rise of I_c was higher from the enriched sample than that from the original sample, evidenced that M@FA-Os NP-mediated enrichment of MR-1 from the mixed culture was specific and feasible. No bioelectricity enhancement and additional oxidation current were detected in the electrochemical reactor containing *S. oneidensis* MR-1 mixed with and without nanobeads. (Figure S4).

5.2.3 Current production in magnetically enriched inoculation from the soil sample

To evaluate a natural sample, we applied our magnetic isolation approach to microbial consortia from soil sampled from a humus-abundant environment. In this environment, the ability of anaerobic metabolism or EET may be a key factor in the survival and activity of microbial cells (39). The various cellular morphologies observed in the TEM (Figure 5A–C) images indicated the presence of microbial consortia in the collected

soil sample. TEM showed that the nanobeads attached to the cell surface of cells, which was also observed in scanning electron microscopy (Figure 5D). The heterogeneous adhesion of nanobeads on specific bacteria likely reflects that different strains have different DAB polymerization abilities and microbial surface characteristics.

To identify the taxa of microbial cells associated with MNPs, 16S rRNA gene-based community analysis of the magnetically isolated microbial culture was performed. To obtain a sufficient amount of DNA for 16S rRNA gene analysis, nanobead-conjugated bacteria were additionally incubated in LB under aerobic conditions for seven h, and the relative abundance of microbial species was compared with that in the original sample (Figure 6A). The relative abundance of *Enterobacteriaceae* and *Enterobacterales* increased by approximately 3- and 20-fold, respectively, compared with that in the original sample. In contrast, dominant species in the original sample, such as *Comamonas*, *Microvirgula aerodenitrificans*, and *Planococcaceas*, were present at very low levels (Figure S5).

To examine whether the M@FA-Os NPs could enrich electrogenic bacteria, we performed single-potential amperometry in a LB medium at 30°C. As with 16S rRNA gene analysis, nanobeads were removed from the bacterial solution after incubation in LB under aerobic conditions. The I_c from cells enriched *via* magnetic isolation gradually increased to approximately 100–150 nA in 15 h and continued increasing for more than 35 h (Figure 6B). The original sample displayed an I_c peak at 10 nA in 5 h, and the I_c did not rise over 35 h (Figure 6B). After 35 h, the I_c of the enriched sample was 16-fold higher than that of the unprocessed sample. Given that electrogenic bacteria growth is associated with current production, the initial transition current in the original culture may not be attributable to EET but rather to electrode oxidation of the abiotic substrate in the LB medium. Furthermore, we incubated for more than a week to examine the stability of I_c for its implementation on MFCs (Figure 6C). While the I_c

from the original sample showed a steep decrease after the peak, the I_c did not decrease with the bacterial sample enriched by M@FA-Os NPs, demonstrating the higher stability of microbial current generation from the enriched sample. Consequently, the total electric charge was about twice higher with cells enriched with M@FA-Os NPs than the original sample (Figure 6C). High stability in I_c is most likely due to the colonization of electrogenic bacteria on the electrode, which may be suppressed by other bacteria in the original sample. Accordingly, DPV revealed the distinct oxidative signals peaked at–0.15 and –0.25 V in the original and enriched samples (Figure S6), respectively, suggesting that different redox substrates dominantly mediate current production. These data demonstrate the successful M@FA-Os NPs-mediated enrichment of electrogenic bacteria from environmental microbial consortia.

To further support the conclusion, we performed alpha-diversity analysis, principal coordinate analysis (PCoA), and Venn diagram to estimate the difference between the original sample and the enriched sample using M@FA-Os NPs (Figure S6-S8). Amplicon sequencing was conducted to understand the differences in microbial communities by the enrichment of M@FA-Os NPs and the electrochemical cultivation. In total, 954,308 reads were obtained with a range of 73,857–113,334 reads for each sample (Table S2). Chao1 and Shannon index values of the original sample before and after the electrochemical incubation were at a similar level (Figure S7). In contrast, the values of the enriched sample before and after the electrochemical incubation were smaller than the original samples, which indicates less diversity of microbial communities. The results indicate that the process with M@FA-Os NPs clearly enriched specific microorganisms. Furthermore, the PCoA plot showed that the original sample and enriched samples before and after the electrochemical incubation formed separate clusters (Figure S8), indicating that M@FA-Os NPs and electrochemical cultivation contributed to the change of microbial community. Venn diagram presented

that some bacteria genera captured by M@FA-Os NPs also existed in the original and the enriched samples after electrochemical incubation, indicating these strains contributing to the current production from microbial consortia were enriched using M@FA-Os NPs (Figure S9). Accordingly, a positive correlation was observed for *Enterobacterales*, *Lysinibacillus*, and *Paenibacillus anaericanus*, (Figure 6D–F). Other species, such as *Clostridium hydrogeniformass*, *Clostridium tertium*, and *Enterobacteriaceae,* also exhibited positive correlations after electrode incubation, suggesting that these microbes are electrogenic bacteria (Figure S10). Consistently, *Enterobacter cloacae* SgZ-5T and *Lysinibacillus sphaericus* D-8 have been reported as electrogenic bacteria (40, 41). Given that *Enterobacterales* was enriched using the nanobeads, the positive correlation between current production and relative abundance of *Enterobacterales* supports that M@FA-Os NPs can enrich electrogenic bacteria without the need for electrochemical incubation.

The relative abundance of other electrogenic candidates from the Venn diagram was not positively correlated with I_c. For example, the counts of *Clostridioides*, *Paenibacillus*, and *Aeromonas* showed an obvious negative correlation with the I_c at +0.2 V (Figure 6G and S9), probably indicating that extracellular electron uptake occurred during this anaerobic electrochemical measurement; indeed, *Clostridium autoethanogenum* and *Clostridium pasteurianum* DSM 525 were previously reported to uptake extracellular electrons (42, 43). Additionally, *Bacillus sp*., such as *Bacillus megaterium* LLD-1 and *Bacillus cereus*, are electrogenic bacteria but displayed a low correlation in our study, suggesting that the carbon source in the LB medium did not induce *Bacillus sp*. to generate a current, as these cells mainly uptake glucose which did not contain in LB medium (44, 45).

5.3 Discussion

The incubation of electrogenic bacteria from the consortia by running MFCs requires a few weeks to enrich the electrogenic bacteria (**Table S2**). In contrast, our culture-free method for enriching electrogenic bacteria takes only minutes because we establish a specific adhesion system for capturing electrogenic bacteria by M@FA-Os NPs from the environment. Furthermore, enriched bacteria consortia by M@FA-Os NPs showed a larger current production and remarkably better stability than the original microbial consortia (**Figure 6B-C**). In addition, the fabrication of M@FA-Os NPs by modifying the surface of the commercial product of MNP is straightforward and cost-efficient. These properties of M@FA-Os NPs demonstrate the practical implementation of our method for improving power generation and stability in MFCs without long incubation and using expensive additives (46, 47). By applying our DAB-Os covalently linking magnetic isolation strategy, electrogenic bacteria were enriched from an environmental soil sample with increased relative abundances of *Enterobacteriaceae* and *Enterobacterales* compared to those in the original sample, without an additional electrochemical incubation process. *Enterobacter* as a genus of the order *Enterobacterales* has served as a significant electrogenic bacteria in MFCs (48). Huang *et. al.* also reported *Enterbacto*r, the only species representing the order of *Enterobacterales*, as a dominant species in MFCs (49). However, it took one year for the enrichment of *Enterbactor* to reach the relative abundance of 33.4%. On the other hand, our method can enrich *Enterobacteriaceae* and *Enterobacterales* to 76.1 and 21.8%, respectively, in minutes before electrochemical measurement, and the relative abundance of *Enterobacterales* remained after electrochemical measurement. Furthermore, such quick enrichment also facilitates making decisions for the suitability of the environment or water source for MFCs application, which has been difficult

before constructing and running the reactor, as demonstrated in numerous case studies (50-52). Rapid enrichment of environmental electrogenic bacteria by our method can accelerate the practical implementation of MFCs.

The bacterial sample enriched using our method showed better stability in current production during electrochemical incubation for a week than the original soil sample, supporting the feasibility of our method applying to the system of MFCs. The stability of power output in MFCs was enhanced by activating different metabolic pathways (53). However, because MFCs oxidize various substrates from natural or industrial water sources, the activation of specific metabolic pathways is not realistic for practical MFC application. Our results suggested that the enrichment of EET-capable bacteria *via* nanobeads is a potential strategy to stabilize microbial power generation in real MFCs. The covalent binding between OsO_4 and the DAB polymer on the bacterial surface may be crucial for capturing electrogenic bacteria. Upon the addition of OsO_4, the brown DAB polymer immediately changes to an "Os black" form as a product of Os(IV) or Os(VI) (54). Additionally, OsO_4 with its oxidative ability can easily react with a carbon-carbon double bond (C=C) to form an Os ester (55). Thus, $Os(VIII)O_4$ may oxidize C=C onto the DAB polymer and be reduced to an $Os(IV)O_4$-DAB or $Os(VI)O_4$-DAB structure (**Scheme S1**). Therefore, when M@FA-Os NPs are added to DAB-covered bacteria, two oxygens on M@FA-Os NPs can react with DAB to form an Os(IV) ester. Consistent with our results, DAB-covered bacteria were not washed away from the Os-grafted MNPs, even under electrostatically unfavorable conditions in which non-specific adhesion of bacteria was successfully minimized. Given that the FT-IR spectroscopy revealed the formation of Os=N from Os=O upon grafting of OsO_4 onto M@FA NPs (Figure 1B), the efficiency of capturing DAB-polymer-coated bacteria was improved through the conservation of the number of Os=O ligands. In the present study, we suppressed the non-specific binding of nanobeads to K12 and MR-1 in the absence

of DAB polymer. The binding of MR-1 in the absence of DAB polymer with nanobeads can be easily removed during the washing step (**Figure 3A-B**). On the other hand, non-specific binding of K12 with nanobeads only can be suppressed during the binding step with the specific ionic strength of the buffer (**Figure 3C**). Previous studies showed that K12 could attach to the substrate and form an irreversible adhesion within 30 min (56, 57). K12 with adhesive fimbriae (~1 μm) can strengthen the contact between bacteria and substrates, suggesting that K12 might interact with nanobeads (20–50 nm) during the binding process, which results in irreversible conjugation between both and being impossible to separate them during washing process (58). Therefore, a suitable buffer used in the binding process is essential to provide large electrostatic repulsion between nanobead and K12, thus reducing the condition of non-specific conjugation (58).

5.4 Conclusion

In the present study, we developed a quick enrichment method for accelerating electrogenic bacteria from the environment, which simplifies the process of the enrichment of electrogenic bacteria and enhances the efficiency and stability of microbial current production. Compared to conventional methods, this method is simple and inexpensive and can be implemented in MFCs, which is expected to contribute to its practical application. Furthermore, since the M@FA-Os NPs target DAB polymerized electrogenic bacteria with electron transfer proteins potentially with any transient metal centers, our method also may facilitate identifying the novel types of genes that are critical for the EET mechanism *via* further analyzing taxa and genetic information from the enriched electrogenic bacteria. Therefore, the present method enables the practical implementation of improving the efficiency of MET systems and increasing our understanding of microbial electron transport mechanisms.

5.5 Materials and methods

Reagents and material

Iron(II,III) oxide nanoparticles (Fe_3O_4 NPs, 97%), DAB [$(C_6H_3(NH_2)_2)_2$, 98%], OsO_4 (4%), and CelLytic™ B cell Lysis were purchased from Sigma-Aldrich (St. Louis, MO, USA). FA ($C_{19}H_{19}N_7O_6$, 98%) was from Nacalai Tesque (Kyoto, Japan). NaOH (97%), NaCl (99.5%), HEPES ($C_8H_{18}N_2O_4S$, 99%), sodium bicarbonate ($NaHCO_3$, 99.5%), NH_4Cl (99.5%), magnesium chloride hexahydrate ($MgCl_2 \cdot 6H_2O$, 98%), calcium chloride dihydrate ($CaCl_2 \cdot 2H_2O$, 99.9%), and cobalt(II) chloride hexahydrate ($CoCl_2 \cdot 6H_2O$, 99%) were obtained from Wako (Osaka, Japan). Ultra-purified water (double-distilled water, DDW) was obtained using a Direct-Q® 5 UV Remote Water Purification System (Millipore, Billerica, MA, USA). LB medium and yeast extract were from BD Biosciences (Franklin Lakes, NJ, USA).

Preparation of M@FA-Os NPs

Controlled functionalization of MNPs was performed using FA and OsO_4 solutions. After dispersing 0.06 g Fe_3O_4 NPs into 30 mL DDW, 0.1 M FA in 1 mL of 5.0N NaOH at pH 13 was added to the solution; this mixture was stirred for 18 h in the dark and at 25°C to form FA-modified Fe_3O_4 NPs (M@FA NPs). The sample was collected by a magnetic rack for 1 min, and the pellet of M@FA NPs was resuspended in DDW. After washing the M@FA NPs at least three times with DDW, they were dispersed in 30 mL DDW, and 10.0 mL of 1% OsO_4 solution was added, followed by intense stirring at room temperature for four h to form osmium-exposed Fe_3O_4 NPs (M@FA-Os NPs). The M@FA-Os NPs were washed at least three times, as described above. The final samples were stored in 1 mL DDW until use. To prepare M@FA-Co, the protocol was

the same as that described above, except that the OsO_4 was replaced with $CoCl_2$. The methods used to characterize the materials, including powder X-ray diffraction, Fourier transform infrared (FT-IR) spectroscopy, X-ray photoelectron spectroscopy, and TEM, are presented in **Supporting Information I**.

Cultivation of bacteria

Shewanella oneidensis MR-1 and *E. coli* K12 were cultured in 10 mL sterilized LB medium at 30°C and 37°C, respectively, for 20 h. Before use in all experiments, the culture samples were washed at least three times with a defined medium (DM), prepared as described below, with repeated centrifugation (7000 rpm, 5 min), and then resuspended in fresh DM. The OD_{600} of the cell suspension was set to 1.0; these samples were used in the DAB polymerization reaction.

The DM was prepared by adding NaCl (10 g L^{-1}), HEPES (7.2 g L^{-1}), $NaHCO_3$ (2.5 g L^{-1}), NH_4Cl (1.0 g L^{-1}), $MgCl_2{\cdot}6H_2O$ (0.2 g L^{-1}), $CaCl_2{\cdot}2H_2O$ (0.08 g L^{-1}), and 0.5 g L^{-1} yeast extract in 1 L DDW, followed by standard sterilization in an autoclave.

2.4. DAB polymerization on the bacteria surface

To prepare the DAB working solution, 0.0057 g DAB was dissolved in 0.105 mL of 0.1 M HCl solution and sonicated for 30 min; next, 3.695 mL of 0.05 M Tris-HCl (pH 8.0) was added to the previous solution and sonicated for 15 min. The solution was filtered through a 0.22-μm filter to obtain the DAB working solution.

DAB working solution (1.5 mL) was added to 1 mL of *S. oneidensis* MR-1 and *E. coli* K12 at an OD_{600} of 1.0, and the sample solution was blended for 30 min. In the *S. oneidensis* MR-1 group, the solution color gradually became brown during the reaction as the DAB polymer formed. No color was formed in the *E. coli* K12 group during the

reaction. After the reaction, the bacterial sample was washed at least three times using DDW.

The procedures used to characterize the bacterial samples, including TEM, scanning electron microscopy, and zeta potential measurement, are presented in **Supporting Information I**.

Determination of an optimized buffer system for binding and washing processes

The OD_{600} of the bacterial solutions of *S. oneidensis* MR-1 and *E. coli* K12 was adjusted to 0.25 in 1 mL of binding buffer (water and PBS at concentrations of 0.001, 0.005, 0.02, 0.05, or 0.1 M and pH 3, 5, 7, 9, or 11). M@FA-Os NPs (10 μL) were added to the above bacterial solution and gently shaken for 30 min to conjugate the DAB-marked bacteria. The M@FA-Os NPs could not conjugate to the DAB-unmarked bacteria *S. oneidensis* MR-1 without DAB coating and to DAB polymerization-treated *E. coli* K12. After shaking, the solution was placed on a magnet for 1 min to concentrate the nanobead-conjugated bacteria and remove unbound bacteria. The nanobead-conjugated bacteria were washed twice with various elution buffer solutions containing 0.02 M Tris-HCl and different concentrations of NaCl (0, 0.1, 0.5, and 1.0 M) at different pH values (3, 5, 7, 9, and 11). Based on these tests, the optimal binding and elution conditions were determined as 0.005 M PBS as the binding buffer (pH 7) and 0.02 M Tris-HCl + 0.5 M NaCl as the elution buffer.

Magnetic separation of EET-involved bacteria from the natural bacterial community

The environmental soil sample was sourced from Fukushima, Japan. The soil sample (0.5 g) was mixed with 10 mL DDW and filtered using a ten μm filter to remove large impure particles. After washing three times with DDW, the sample was inoculated into a sterilized LB medium to enrich the bacteria. This step was followed by DAB

polymerization, nanobead binding, and magnetic separation, as described above, to capture EET-capable bacteria from the soil-source microbiomes.

Bicinchoninic acid assay

The pellet of the nanobead-conjugated bacteria was resuspended in 30 μL CelLytic™ B cell Lysis solution and sonicated for 30 min to lyse the cells. The total protein concentration of the lysis solution was determined using a bicinchoninic acid assay kit (see the detailed procedure in **Supporting Information I**).

Whole-cell electrochemistry

The bacteria captured with the nanobeads were cultured in 2 mL of sterilized LB medium under aerobic conditions. To capture samples from a mixture of MR-1 and K12, when the OD_{600} of the culture reached approximately 1.0, the samples were washed twice with DM containing 10 mM lactate. The nanobeads were removed using a magnetic rack. The final samples were adjusted to an OD_{600} of 1.0 with DM containing 10 mM lactate. The environmental samples were washed twice with a sterilized LB medium. The final samples were adjusted to an OD_{600} of 0.5 with a sterilized LB medium. The cell suspensions (200 μL) were loaded onto printed electrodes, and single-potential amperometry was performed using a potentiostat (VMP 3; BioLogic, Seyssins, France), at an electrode potential of +0.2 V versus an Ag reference electrode at 30°C. The background current from a LB medium was subtracted before averaging the microbial current production for each sample. A screen-printed electrochemical array composed of 96 three-electrode electrochemical cells (DRP311L (U100), Metrohm, DropSens, Tokyo, Japan) was used for electrochemical measurement and had a surface area of 0.21 cm^2. The working, counter, and reference electrodes of the printed electrode were carbon, carbon, and silver, respectively.

Another electrochemical measurement was performed in single-chamber, three-electrode reactors. Indium Tin Oxide (ITO)-deposited glass substrate (3.14 cm^2), a platinum wire, and Ag/AgCl (sat. KCl) were used as working, counter, and reference electrodes, respectively. The bacterial samples were adjusted to an OD_{600} of 1.0 with 5 mL of DM containing 10 mM lactate, and the potential on the working electrode was set at +0.2 V versus an Ag/AgCl reference electrode at 30°C. All mediums were purged with nitrogen for 30 minutes before being loaded into the electrochemical measurement. Differential pulse voltammetry (DPV) was conducted with ITO systems by sweeping electrode potential from positive to negative region with an automatic polarization system, using 5.0 mV or −5.0 mV pulse increments, 50 mV pulse amplitude, and 100 ms pulse width, and a 5.0 s pulse period. Background current was subtracted using SOAS software which fits the baseline from regions sufficiently far from the peak, assuming continuation of a similar and smooth charging current throughout the peak region (59).

16S rRNA gene sequencing analysis

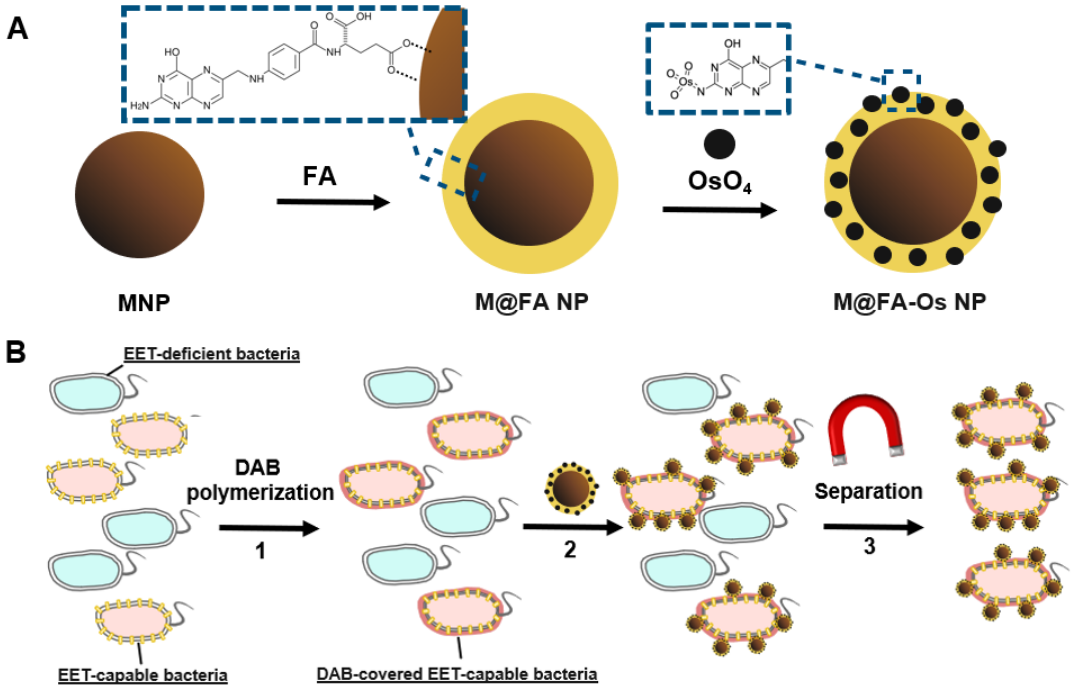
The culture was centrifuged at 16,000 ×g for 5 min, and the supernatant was discarded. The cell pellet was resuspended in 750 μL DNA/RNA shield solution, and DNA was extracted using a ZymoBIOMICS DNA/RNA Miniprep Kit (Zymo Research, Irvine, CA, US) according to the manufacturer's protocol. The DNA concentration was measured using a Qubit™ dsDNA HS assay kit (Thermo Fisher Scientific, Waltham, MA, USA) and Qubit™ 4 fluorometer (Thermo Fisher Scientific). Partial 16S rRNA genes (V4–V5 regions) were amplified using PCR with the primer set 530F (5′-CCATCTGTTCCCTCCCTGTCTCAG-3′) and 907R (5′-CCTATCCCCTGTTGCGTGTCTCAG-3′) (60). The addition of multiplexing indices/Illumina sequencing adapters (Illumina, San Diego, CA, USA) and purification

were performed as described previously (61). Amplicons were sequenced using an Illumina MiSeq platform and MiSeq v3 reagent (Illumina) as the 300 bp end according to Illumina's standard protocol. Raw FASTQ files were de-multiplexed based on their unique barcodes using the QIIME 2 demux plugin (62). De-multiplexed sequences from each sample were treated using the QIIME 2 dada2 plugin to yield the feature table (63). The QIIME 2 feature-classifier plugin was used to align feature sequences to a pre-trained SILVA-138 99% database to generate the taxonomy table (64).

2.10. Statistical analysis

Statistical analysis was performed by using Student's t-test or one way ANOVA using SPSS Software (IBM, Armonk, New York, USA). A p-value of < 0.05 will be considered statistically significant. *: $P < 0.05$; **: $P < 0.01$; ***: $p < 0.001$; ****: $p < 0.0001$)

5.6 Figures



Scheme 1. Preparation of Osmium-Exposed Magnetic Nanoparticles (M@FA-Os NPs) and Workflow for Selective Isolation of Electrogenic Bacteria

(A) Schematic illustration of sequential surface modification of magnetic nanoparticles (MNPs) using folic acid (FA) and osmium tetroxide (OsO4) to form osmium-exposed MNPs (M@FA-Os NPs). (B) Experimental procedure applied to capture and isolate electrogenic bacteria from a mixture using M@FA-Os NPs as follows: (1) The electrogenic bacteria were coated with a DAB polymer after outer membrane cytochrome (OMC)-catalyzed DAB polymerization. (2) M@FA-Os NPs were added to bind with DAB polymer-coated bacteria. (3) Electrogenic bacteria bound to M@FA-Os NPs were concentrated and isolated using a remote magnet.

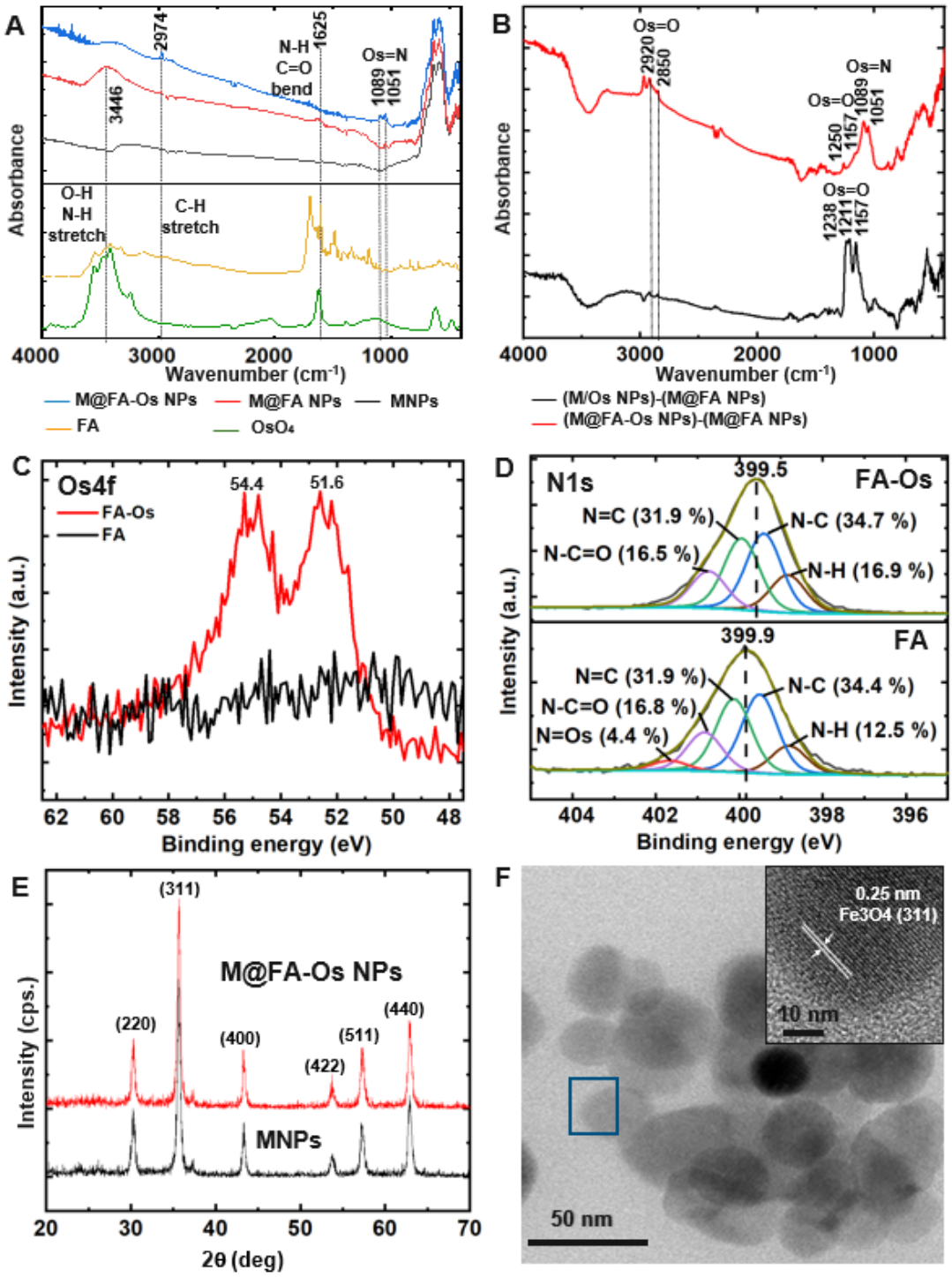


Figure 1. Characterization of nanobeads using Fourier-transform infrared spectroscopy (FT-IR), X-ray photoelectron spectroscopy (XPS), X-ray diffraction (XRD), and transmission electron microscopy (TEM).

(A) Absorbance FT-IR spectrum of folic acid, osmium tetroxide, magnetic nanoparticles (MNPs), MNPs conjugated with folic acid (M@FA NPs), and MNPs conjugated with osmium tetroxide and FA (M@FA-Os NPs). **(B)** Difference FT-IR spectrum of M@FA-Os NPs minus M@FA NPs and MNP/Os minus M@FA NPs. XPS

spectra of a 1:1 stoichiometric mixture of FA and OsO_4 without MNPs and FA displaying binding energy signals of **(C)** Os 4f and **(D)** N 1s. **(E)** Crystalline and composition analysis of MNPs and M@FA-Os NPs, as assessed from powder X-ray diffraction patterns. **(F)** TEM images of M@FA-Os NPs. The high magnification image in the inset (black frame) shows M@FA-Os NPs with evident lattice fringes, indicating crystal planes of (311). Higher magnification of the area in Figure 1F is marked using a blue frame.

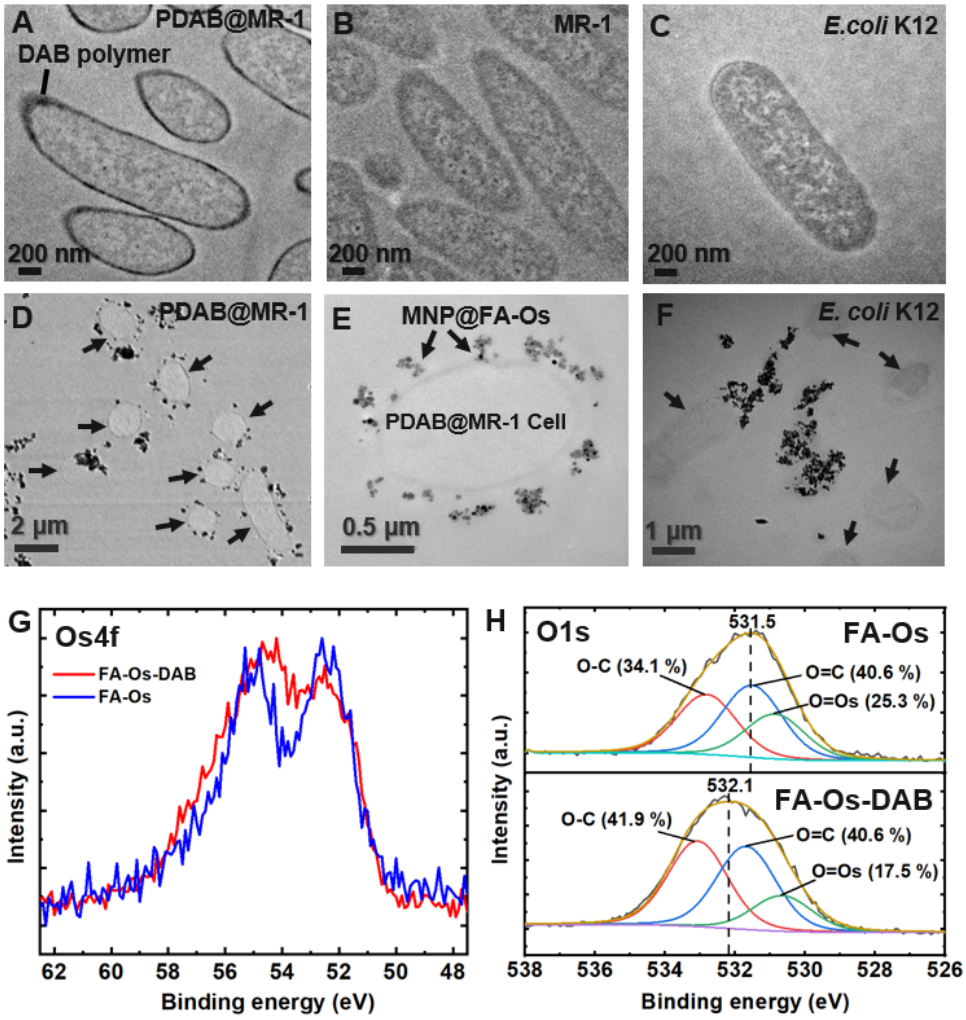


Figure 2. Evaluation of the effect of DAB polymerization for targeting electroactive bacteria.

Transmission electron microscopy (TEM) images of **(A)** DAB-stained *Shewanella oneidensis* MR-1, **(B)** *Shewanella oneidensis* MR-1 without DAB staining, and **(C)** DAB-stained *E. coli* K12. The efficiency of nanobead deposition onto the bacteria surface. TEM images of **(D)** cells and **(E)** a single cell for DAB-polymerized *S. oneidensis* MR-1 with nanobeads and **(F)** DAB-treated *E. coli* K12 cells with

nanobeads. X-ray photoelectron spectra of folic acid and osmium tetroxide-conjugated DAB (FA-Os-DAB) and FA-Os without magnetic nanoparticles showing the binding energies of **(G)** Os 4f and **(H)** O 1s.

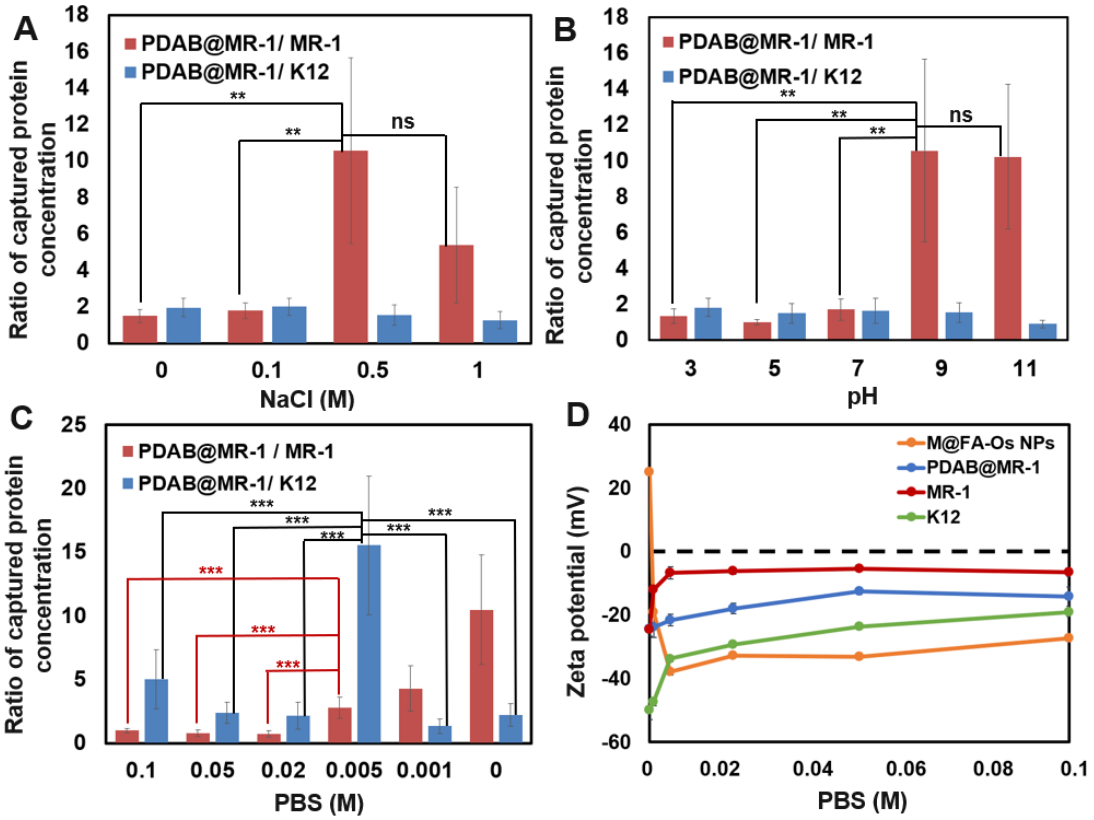


Figure 3. Effect of washing and binding conditions on protein concentration after processing with magnetic nanoparticles conjugated with folic acid and osmium tetroxide (M@FA-Os NPs).

(A–B) The binding condition was fixed with ultrapure water at pH 7, and the washing condition was modified as follows: **(A)** ionic strength (NaCl 0, 0.1, 0.5, and 1.0 M with 0.02 M Tris-HCl at pH 9) and **(B)** pH 3, 5, 7, 9, and 11 with 0.02 M Tris-HCl + 0.5 M NaCl. The ratios of the protein concentration of the DAB polymer-coated *S. oneidensis* MR-1 (PDAB@MR-1) and those of *S. oneidensis* MR-1 and DAB-treated *E. coli* K12 were compared. **(C)** The washing condition was fixed as 0.02 M Tris-HCl + 0.5 M NaCl, pH 9, whereas the binding condition was modified by using different ionic strengths (0, 0.001, 0.005, 0.02, 0.05, and 0.1 M PBS) at pH 7. The ratios of the protein concentration of the PDAB@MR-1 and those of *S. oneidensis* MR-1 and DAB-treated *E. coli* K12 were compared (ns: no significance, $^{**}p < 0.01$ and $^{***}p < 0.001$). **(D)** Zeta potential evaluation of M@FA-Os NPs and bacteria: PDAB@MR-1, *S. oneidensis* MR-1, and *E. coli* K12.

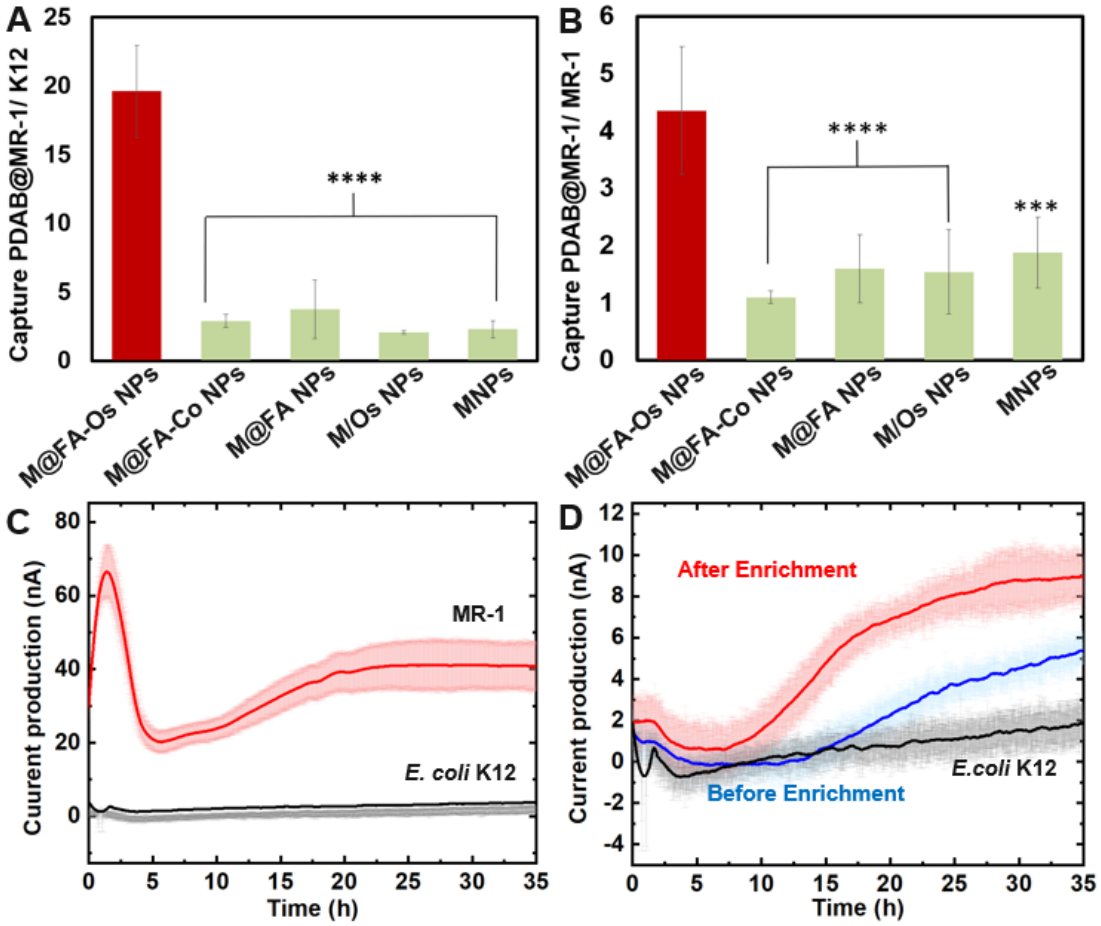


Figure 4. Enrichment of *S. oneidensis* MR-1 cells using magnetic nanoparticles (MNPs) conjugated with folic acid and osmium tetroxide (M@FA-Os NPs).

The capture efficiency was determined by quantifying the protein from the lysed bacterial sample. The ratio of the protein level in DAB-polymerized *S. oneidensis* MR-1 to that in **(A)** DAB-treated *E. coli* K12 or **(B)** original *S. oneidensis* MR-1 captured using different materials was evaluated (****$p < 0.0001$ and ***$p < 0.001$, n = 3) **(C)** Cathodic current production by *S. oneidensis* MR-1 and *E. coli* K12 is depicted by red and black lines, respectively. **(D)** Anodic current monitoring conducted on printed electrodes poised at +0.2 V with lactate as the sole electron donor in an anaerobic chamber at 30°C. The different groups included DAB-polymerized *S. oneidensis* MR-1 before and after enrichment from the two-in-one sample solution and *E. coli* K12, depicted as blue, red, and black curves, respectively. The light blue, red, and gray error bars represent the standard error of the means in DAB-polymerized *S. oneidensis* MR-1 before and after enrichment from the two-in-one sample solution and *E. coli* K12, respectively (n = 3).

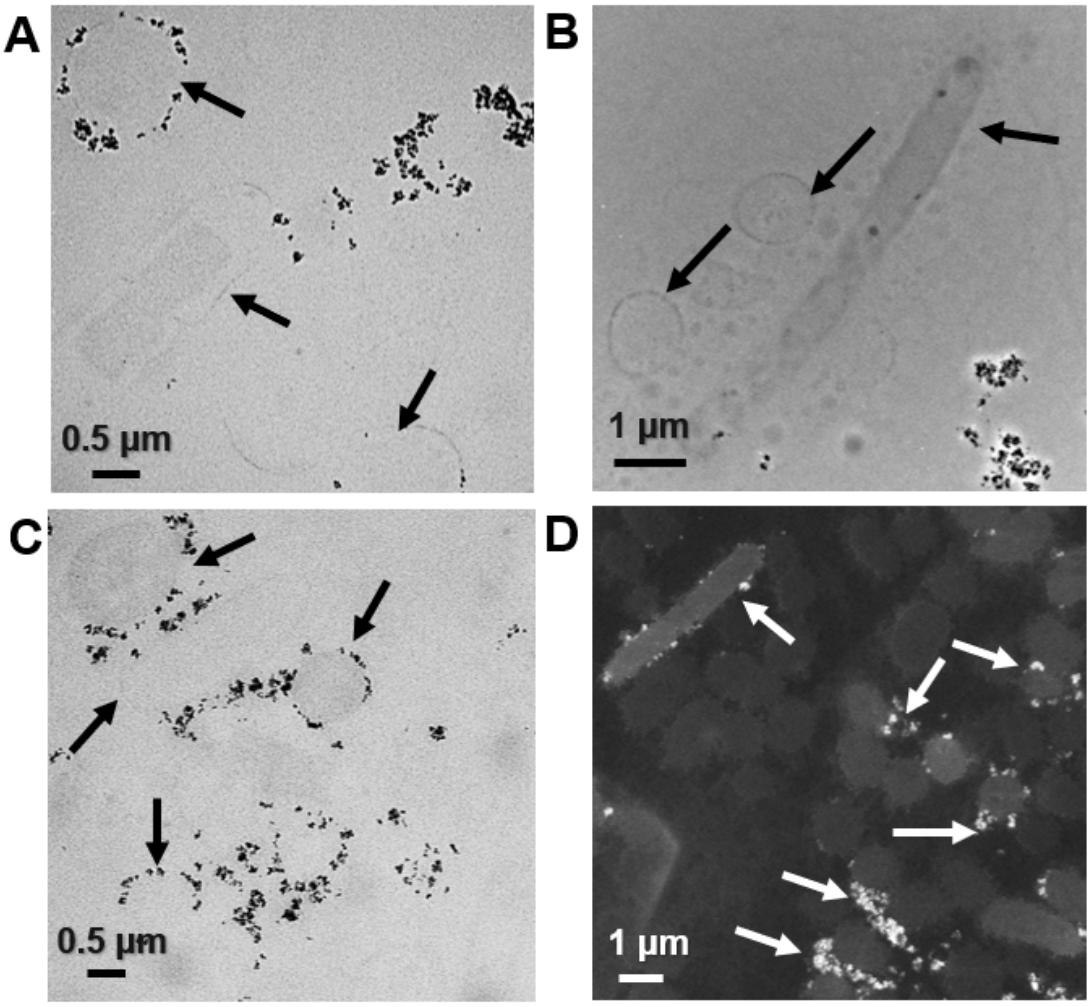


Figure 5. Morphological Characterization of the DAB-Polymerized Bacterial Community Processed with M@FA-Os Nanoparticles

(A–C) Transmission electron microscopy (TEM) and **(D)** scanning electron microscopy images of a bacterial community after treatment with DAB polymerization and processing with magnetic nanoparticles conjugated with folic acid and osmium tetroxide (M@FA-Os NPs). The black arrows indicate the heterogeneous attachment of nanobeads onto the different bacterial strains. The white arrows in D indicated the positions of nanobeads with significantly brighter contrast contributed by the higher conductivity.

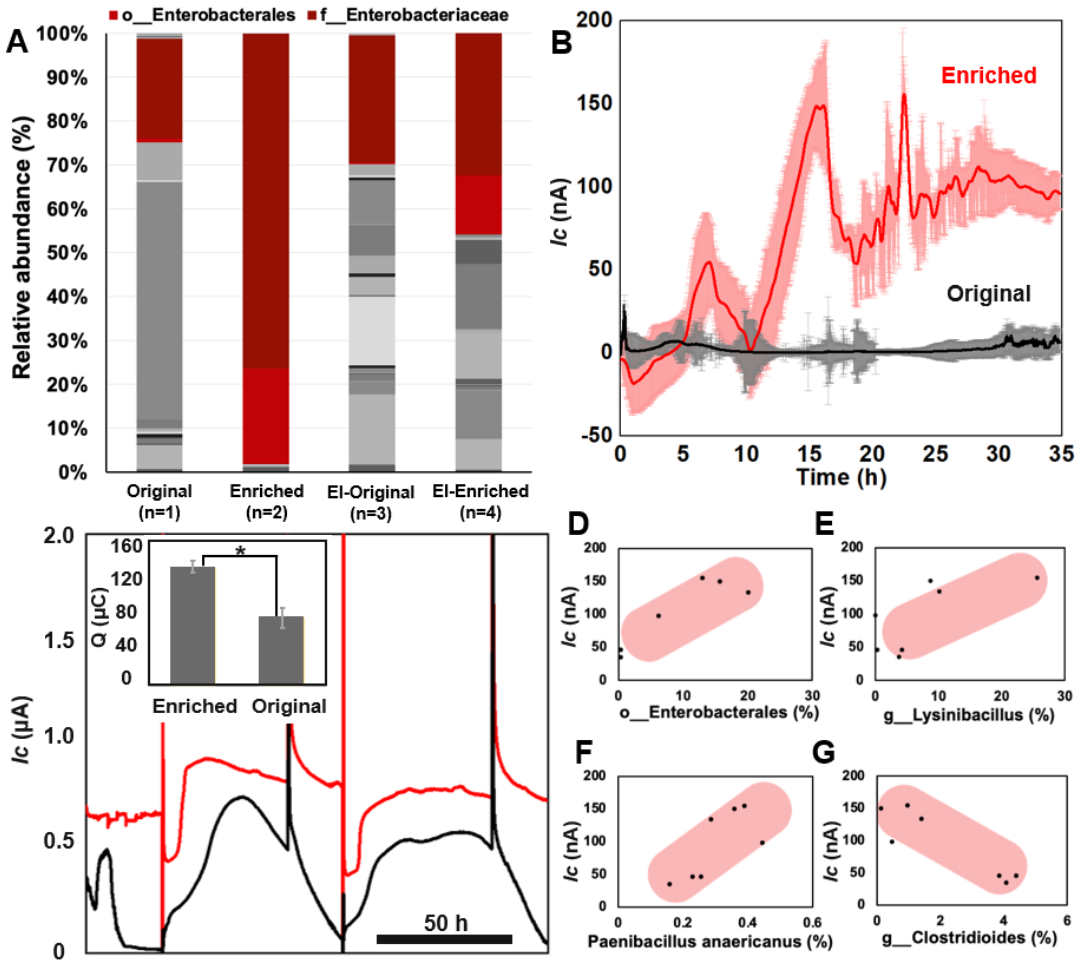


Figure 6. Microbial Composition and Electrochemical Response of Magnetically Enriched Bacterial Communities Using M@FA-Os Nanoparticles

(A) Relative abundance of microbial 16S rRNA sequences classified using the Miseq system. "Captured" is the sample treated by magnetic nanoparticles conjugated with folic acid and osmium tetroxide (M@FA-Os NPs) before electrochemical measurement. "Original" is the sample that was not treated using our method. Electrochemical incubation (EI)-captured and EI-original are the Captured and Original samples enriched after EI for 35 h, respectively. **(B)** Anodic current (I_c) *versus* time measurements conducted on printed electrodes poised at +0.2 V with the LB medium in an anaerobic chamber at 30°C. The I_c time profile from the Captured and Original samples are depicted using red and black lines, respectively. The error bars represent the standard error of the means (n = 3). **(C)** Representative long-term I_c time course from the Captured and Original samples. Anodic current monitoring on indium tin oxide electrodes poised at +0.2 V with lactate as a sole electron donor under anoxic conditions at 30°C. The data shown here are I_c for 170 h after the first current saturation in the Captured and Original samples. Medium exchange at 35 (number 1) and 110 h (number 3) and differential pulse voltammograms at 80 (number 2) and

160 h (number 4) are highlighted. Charge (Q) in the inset calculated from the I_c of the Original and Captured samples during electrochemical incubation for 170 h (n=3). (*p <0.05). Plots of I_c at 35 h *versus* relative abundance from **(D)** *Enterobacterales*, **(E)** *Lysinibacillus*, **(F)** *Paenibacillus anaericanus*, and **(G)** *Clostridioides* (n = 7).

5.7 Supporting information

Detailed Experimental Protocol

Powder X-ray diffraction

Powder X-ray diffraction measurement was performed using an RINT-Ultima III (Rigaku, Tokyo, Japan) at 40 kV and 40 mA to determine the crystallographic structure of magnetic nanoparticles (MNPs) and MNPs grafted with osmium via folic acid (M@FA-Os NPs). MNPs and M@FA-Os NPs (0.1 g) were dried using a t-BuOH freeze dryer.

FT-IR spectroscopy

Fourier-transform infrared (FT-IR) spectra were obtained using an IRTracer-100 (Shimadzu, Kyoto, Japan). Nanobeads were dried using a t-BuOH freeze dryer and mixed with KBr to prepare the sample disk for further measurement under a N_2-filled environment.

X-ray photoelectron spectroscopy

PHI 5000 VersaProbe II (ULVAC-PHI, Kanagawa, Japan) was used to obtain the X-ray photoelectron spectra of folic acid (FA), FA-Os, FA-Os-DAB, M@FA, and M@FA-Os NPs. To prepare FA-Os and FA-Os-DAB analytes, 0.16 M FA and OsO_4 were stoichiometrically mixed and sonicated for 1 h to form FA-Os. DAB monomer in DDW (1 mL; 0.16 M) was prepared and mixed with 0.1 mL H_2O_2 (30%), followed by mild agitation for 1 h to generate the DAB polymer. The as-prepared FA-Os and DAB

polymer were mixed and then stirred for 30 min to form the FA-Os-DAB sample. All analytes were separately dropped on indium tin oxide glass substrates to form a thin film for XPS measurement. CasaXPS Version 2.3.25PR1.0 software was used to analyze the XPS results.

TEM

The size, morphology, and crystal structure of M@FA-Os NPs and bio-samples were directly characterized using transmission electron microscopy (TEM; JEOL JEM2100F, Tokyo, Japan) at 200 kV. A colloid of nanobeads was prepared in 99% ethanol and then dropped onto carbon-coated copper grids (300 mesh), which were incubated overnight at 25°C to obtain the dried sample for further observation. Microbial samples (with M@FA-Os NPs) for TEM were prepared as described by Deng et al. (12). *Shewanella oneidensis* MR-1 (DAB), *Shewanella oneidensis* MR-1, and *E. coli* K12 (DAB) were centrifuged at 7300 ×g for 5 min. The pellets were mixed with 0.4 mL OsO_4 and gently rotated for 1 h (this step was skipped for the binding of bacteria with M@FA-Os NPs). The bacterial samples were washed three times with HEPES buffer solution and the cell pellets were dehydrated through multi-step immersion in a gradient of ethanol (25, 50, 75, and 99%) for 20 min per step. Resin samples were prepared as described by McGlynn et al. (13). Cell pellets after dehydration were immersed in a solution containing 50% LR white resin and 50% ethanol for 1 h. The pellets were collected by centrifugation and immersed in 100% LR white resin for 1.5 h. The cell samples were centrifuged, mixed with 100% LR white resin, and incubated under vacuum condition for 20 min to remove all the residual ethanol. The samples were incubated in an oven at 60°C for 48 h to form resin with bacteria inside. A microtome was applied to cut the resin samples into sections for observation using TEM. The resin samples were trimmed

using a glass knife and sectioned using a diamond knife (Sumi knife type SK 1045; Sumitomo Electric Hardmetal Itami, Hyogo, Japan) at a speed of 1.0 mm s^{-1} and thickness of 70 nm.

SEM

The morphology of bacteria capable of extracellular electron transfer (EET) conjugated with M@FA-Os NPs was directly characterized using an analytical field emission scanning electron microscope (Zeiss AURIGA FE-SEM/FIB/EDX, Oberkochen, Germany). The bio-samples were prepared as described in the TEM section above. These samples were placed on copper grids with platinum coating at 1 kV and 4 mA under vacuum for 180 s and then measured using scanning electron microscopy (SEM).

Zeta potential measurement

Zeta potentials of 1.0 mg mL^{-1} of M@FA-Os NPs at different ionic strengths and pH levels were measured using a Zeta-potential and Particle size Analyzer ELSZ-2000 (Otsuka, Chiyota, Tokyo, Japan). To observe the zeta potential difference for samples at various ionic strengths and pH, 100 μL of bacterial sample (OD_{600} of 1.0) was added to 1 mL double distilled water (DDW) or phosphate-buffered saline (PBS) at different concentrations (0.001, 0.005, 0.02, 0.05, and 0.1 M) and different pH levels (3, 5, 7, 9, and 11).

BCA assay

The Pierce BCA Protein Assay Kit (Thermo Fisher Scientific, Waltham, MA, USA) was used according to the manufacturer's instructions (65) Briefly, BCA Reagent A was mixed with BCA Reagent B (Reagent A:B = 50:1), and 200 μL of the BCA Reagent A and B mixture was added into each well of a 96-well microplate. Standard solutions

containing different protein concentrations were prepared to draw a calibration curve. The samples and standards (20 μL each) were added to each well. The 96-well microplate was incubated at 37°C for 1 h, after which a microplate reader SH-9000 (Corona Electric, Hitachinaka, Ibaraki, Japan) was used to measure the absorbance at 562 nm. The absorbance of the samples was converted to the protein concentration using the calibration curve drawn using the standards.

Supplementary Figures

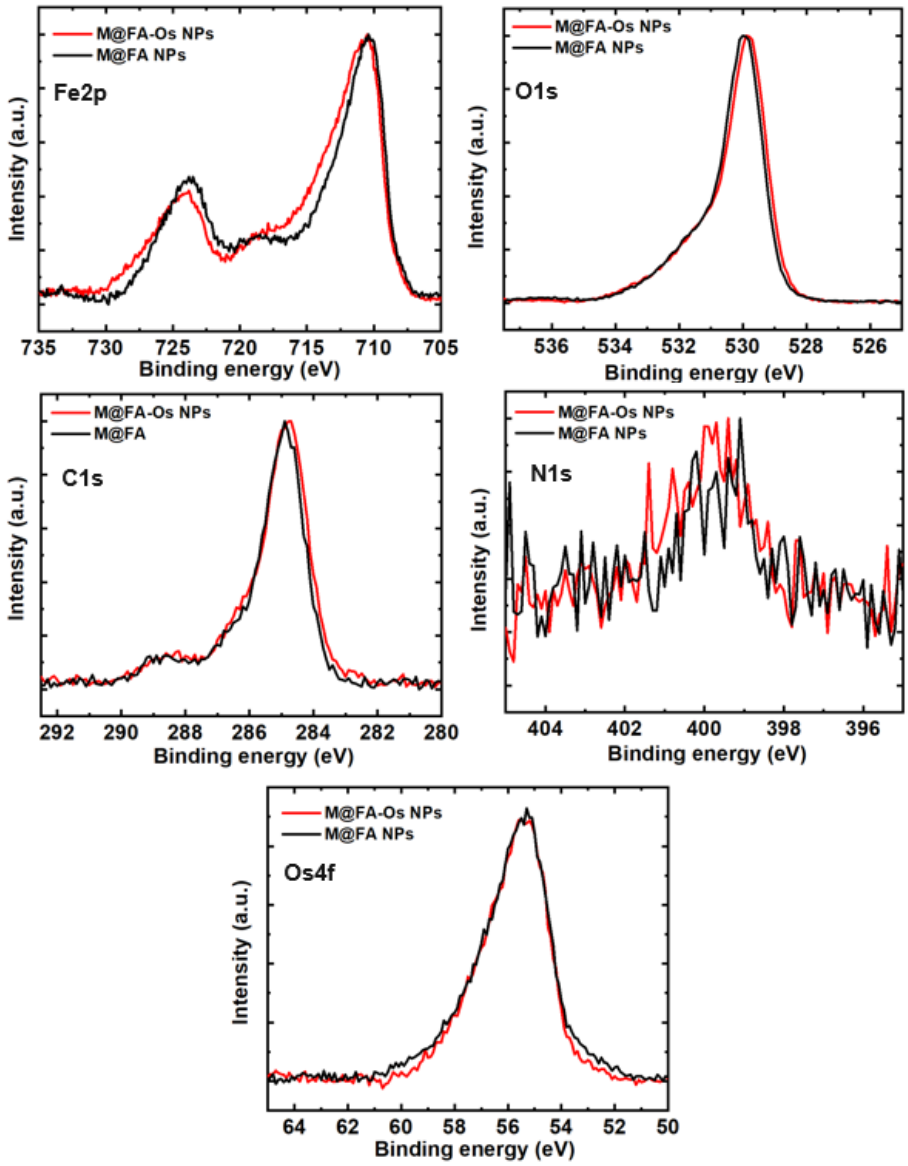


Figure S1. XPS spectra of M@FA-Os and M@FA NPs. The binding energies of Fe in the $2p_{3/2}$ and $2p_{1/2}$ orbitals were 710.4 and 723.8 eV, respectively. The binding energies of O in 1s, C in 1s, and N in 1s orbitals were 529.9, 284.8, and 399.6 eV, respectively. The overlapping binding energy of Os in 4f and Fe in 3p was approximately 55.3 eV.

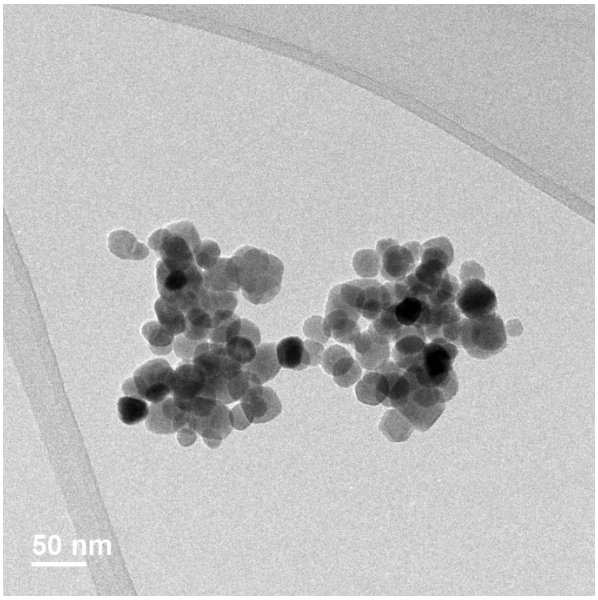


Figure S2. TEM images of bare MNPs on carbon-coated copper grids.

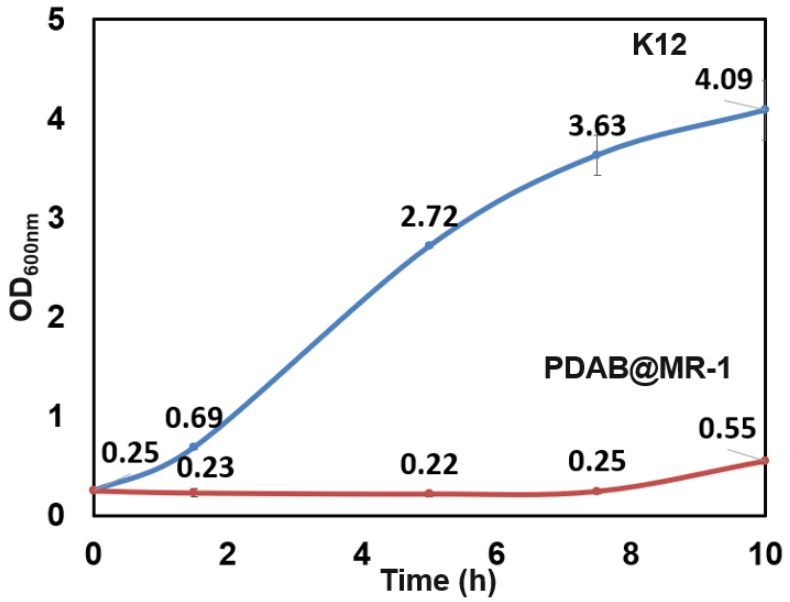


Figure S3. Growth curves of *S. oneidensis* MR-1 and *E. coli* K12 evaluated with optical density at 600 nm. All bacteria were treated with DAB polymers and cultured under aerobic conditions in LB medium at 30°C for 10 h before evaluating electricity production and proliferation.

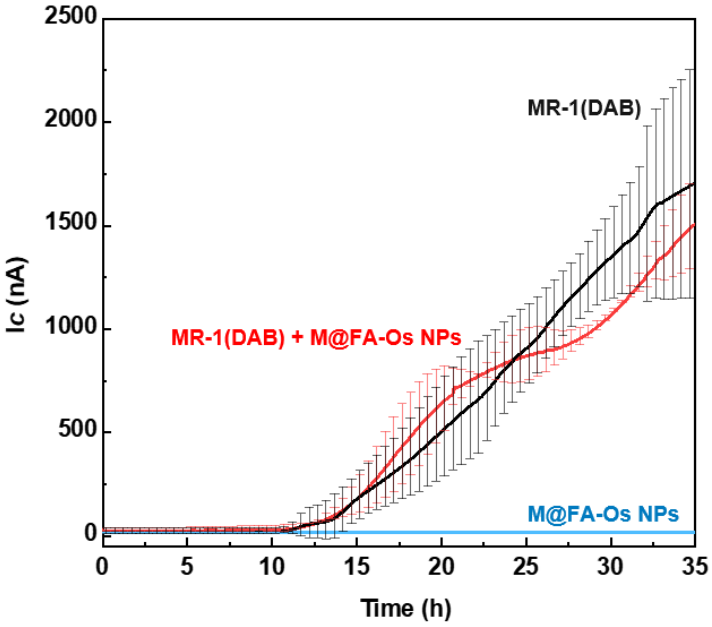


Figure S4. Anodic current (I_c) *versus* time measurements conducted on indium tin oxide electrodes poised at +0.2 V with lactate as a sole electron donor under anoxic conditions at 30°C. The I_c time profile from DAB-polymerized *Shewanella oneidensis* MR-1 with and without MNPs conjugated with osmium tetroxide and FA (M@FA-Os NPs), and only M@FA-Os NPs depicted using black, red, and bule lines, respectively. The error bars represent the standard error of the means (n = 3).

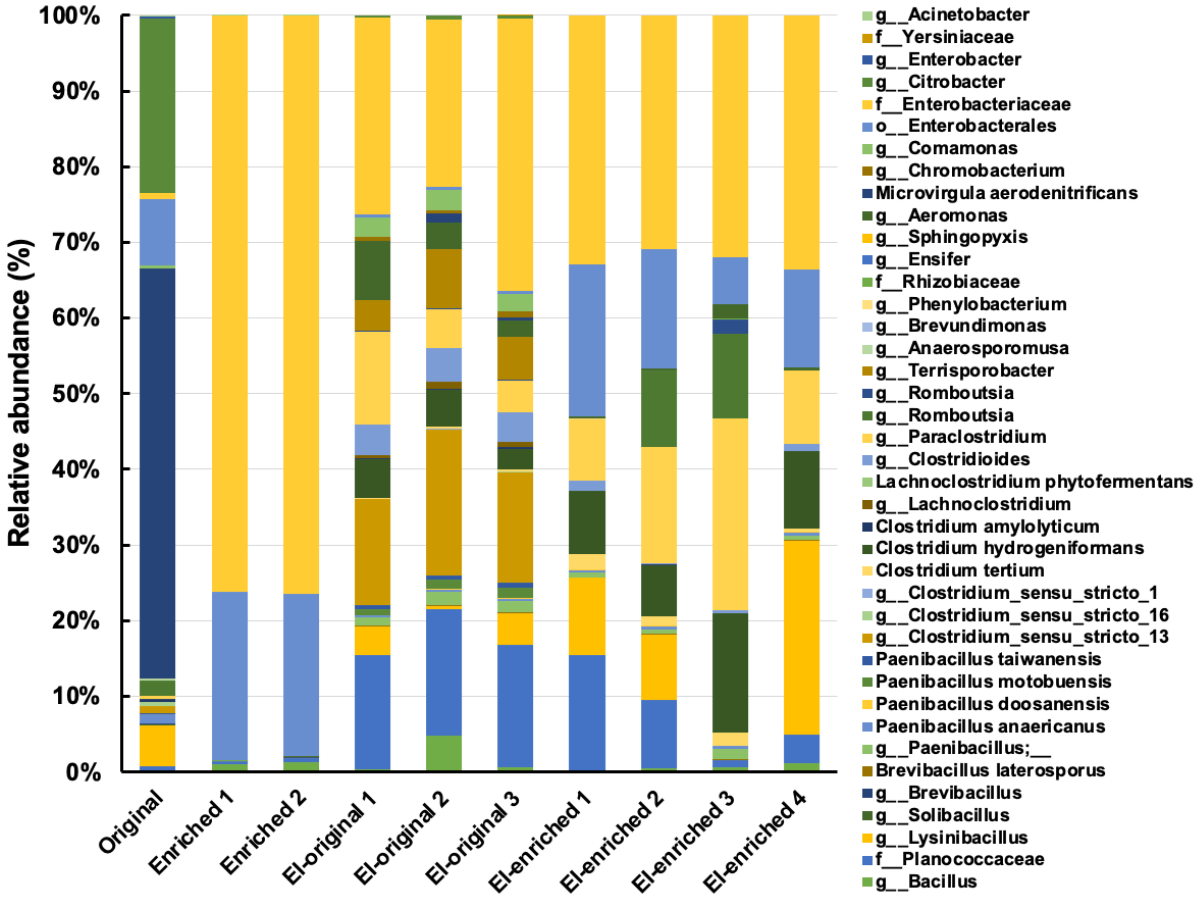


Figure S5. Relative abundance of all operational taxonomic units (OTUs) under four conditions of enriched and original sample before/after electrochemical incubation (EEI) for 35 h. The OTUs highlighted in red showed a low relative abundance before the electrochemical assay and greatly increased after the electrochemical assay.

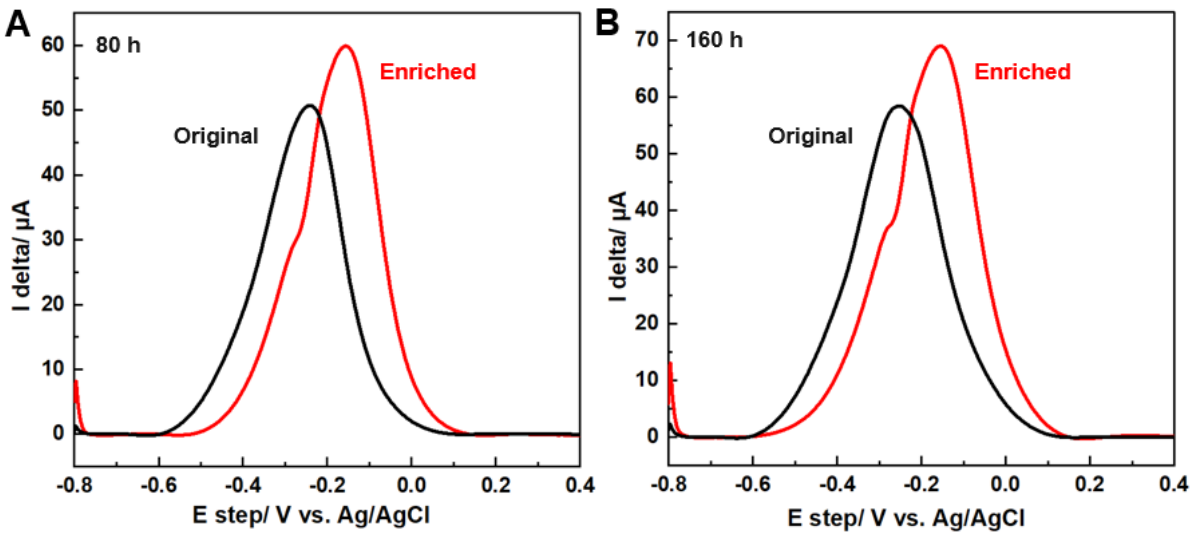


Figure S6. Differential pulse voltammograms from the enriched and original samples. "Enriched" is the sample treated by magnetic nanoparticles conjugated with folic acid and osmium tetroxide (M@FA-Os NPs) before electrochemical measurement. "Original" is the sample that was not treated using our method. The data shown here are DPV at electrochemical incubation for **(A)** 80 and **(B)** 160 h in the enriched and original samples as shown in **Figure 6C**.

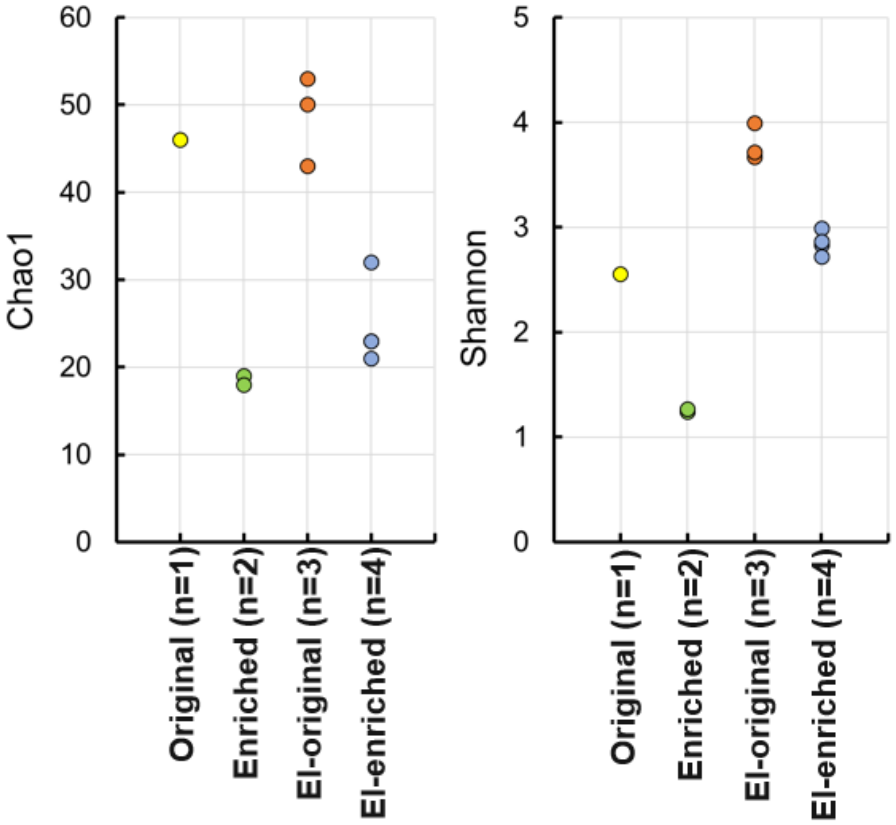


Figure S7. Alpha diversity of microbial community units under four conditions of enriched and original sample before/after electrochemical incubation (EI) for 35 h. The values of (A) Chao1 and (B) Shannon indices are plotted: Original, original sample; "Enriched" is the MNP-enriched sample before electrochemical measurement. "Original" is the sample that was not treated using our method. Electrochemical incubation (EI)- enriched and EI-original are enriched and original samples enriched through EI for 35 h, respectively.

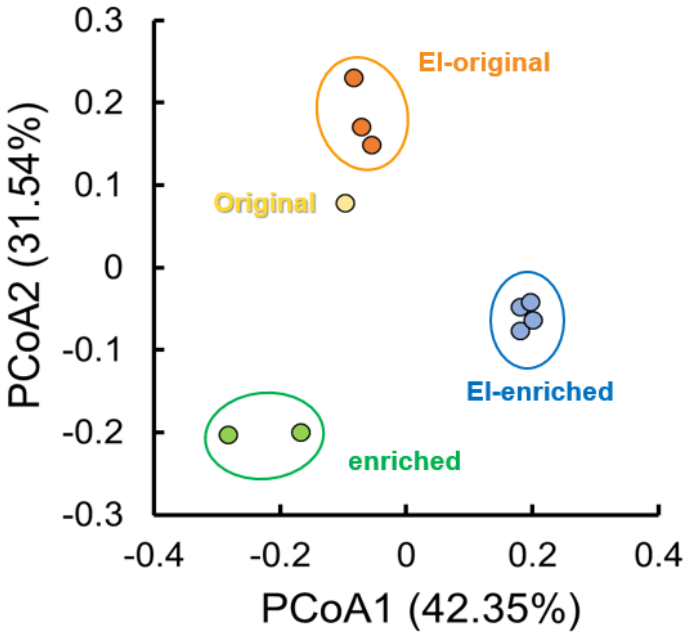


Figure S8. Principal coordinate analysis (PCoA) of all operational taxonomic units under four conditions of enriched and original samples before/after electrochemical incubation (EI) for 35 h based on the unweighted UniFrac distances. Circles highlight each cluster: Original (yellow), the sample that was not treated using our method; Enriched (green), enriched samples with the M@FA-Os NPs; Electrochemical incubation (EI)-original (orange), and EI- enriched (blue), the enriched and original samples enriched through EI for 35 h, respectively.

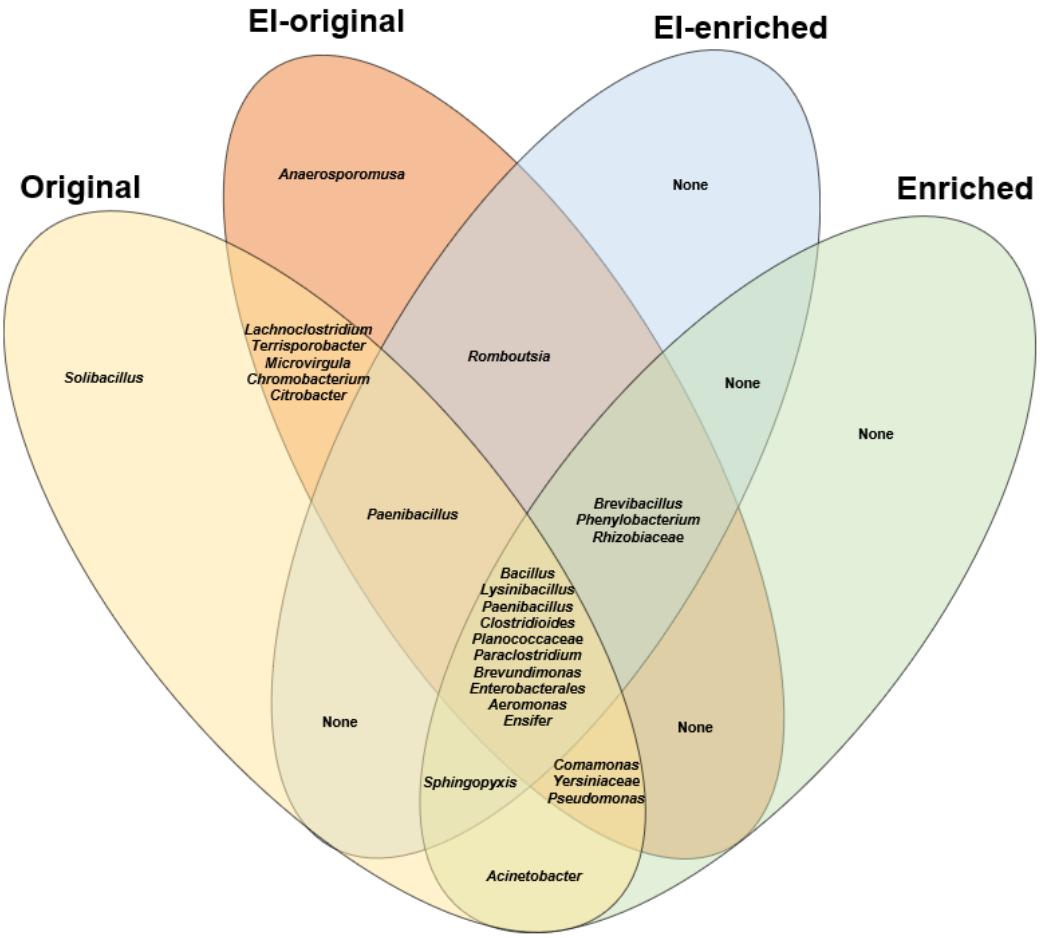


Figure S9. Venn diagram of the bacterial genera in the four conditions (Original, Enriched, EI-original, EI- enriched). Microbial community overlaps between the conditions are presented by overlaps in the diagram. Original (yellow), the sample that was not treated using our method; Enriched (green), enriched samples with the M@FA-Os NPs; Electrochemical incubation (EI)-original (orange), and EI- enriched (blue), the enriched and original samples enriched through EI for 35 h, respectively.

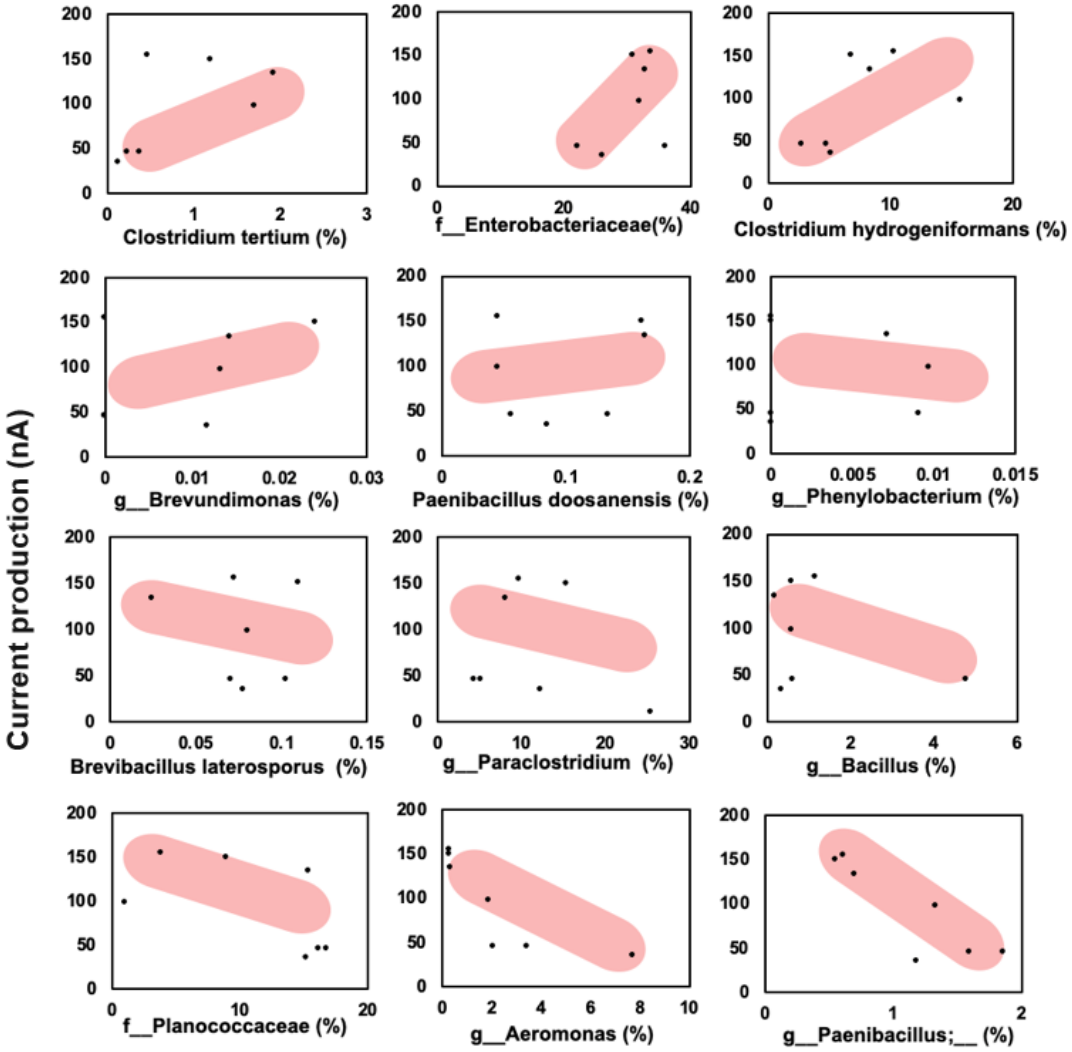
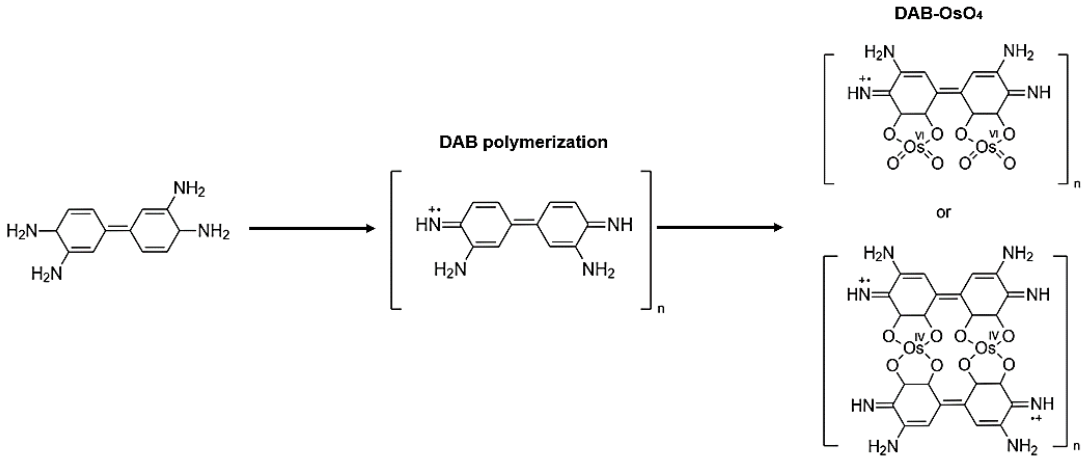


Figure S10. Correlation of bacterial relative abundance with current production (nA) from electrochemical samples (n = 7).



Scheme S1. Proposed mechanism of covalent bond formation between DAB polymer and OsO4. First, the DAB monomer is oxidized by H2O2, with the catalysts of heme iron centers in cytochrome, to form the DAB polymer. The double bond in the DAB polymer is further oxidized by a strong oxidant (OsO4) to form osmic ester bonds, thus generating two types of osmium-conjugated DAB polymers, Os(IV)O4-DAB or Os(VI)O4-DAB.

Enriched Method	Electrochemical system	P_{max}	Time	Ref
MFC only	Dual-chamber MFC	1487	~24 d	(66)
	Dual-chamber MFC	27.3	62 d	(67)
MFC with NPs	Dual-chamber MFC with FeS/FeS_2 NPs	519	46 d	(68)
	Sediment MFC with Fe_2O_3 NPs	87.85	10 d	(69)
M@FA-Os NPs enrichment	None	2828	<1 d	This work

Table S1. Various bacterial enriched methods using different electrochemical systems, maximum of power density (P_{max}), and required time for reaching P_{max}.

Samples	name	input	filtered	denoised	non-chimeric	Accession No.
Original	NIMS-Ele-C	180,625	123,366	123,174	102,003	DRR374771
Enriched	NIMS-Ele-1	136,426	91,813	91,725	87,310	DRR374769
	NIMS-Ele-2	126,312	88,221	87,791	83,430	DRR374770
EI-original	NIMS-Ele-F7	179,635	126,362	125,969	109,789	DRR374778
	NIMS-Ele-E7	144,510	101,237	100,855	85,074	DRR374773
	NIMS-Ele-E72	125,396	87,655	87,221	73,857	DRR374774
EI-enriched	NIMS-Ele-F4	158,471	111,586	111,268	95,450	DRR374775
	NIMS-Ele-F42	189,129	131,978	131,695	113,334	DRR374776
	NIMS-Ele-F5	175,199	122,156	121,926	106,397	DRR374777
	NIMS-Ele-D4	161,581	113,034	112,855	97,664	DRR374772

Table S2. The numbers of filtered, denoised and non-chimeric reads processed from raw FASTQ data. "Enriched" is the M@FA-Os NP-enriched sample before electrochemical measurement. "Original" is the sample that was not treated using our method. Electrochemical incubation (EI)- enriched, and EI-original are enriched, and original samples enriched through EI for 35 h, respectively.

5.8 References

1. B. E. Logan, R. Rossi, A. Ragab, P. E. Saikaly, Electroactive microorganisms in bioelectrochemical systems. *Nat. Rev. Microbiol.,* **17**, 307-319 (2019).
2. D. R. Lovley, Bug juice: harvesting electricity with microorganisms. *Nat. Rev. Microbiol.,* **4**, 497-508 (2006).
3. K. Rabaey, R. A. Rozendal, Microbial electrosynthesis - revisiting the electrical route for microbial production. *Nat. Rev. Microbiol.,* **8**, 706-716 (2010).
4. L. Shi *et al.*, Extracellular electron transfer mechanisms between microorganisms and minerals. *Nat. Rev. Microbiol.,* **14**, 651-662 (2016).

5. M. Waheed, N. Divya, O. Akihiro, Pathogens electrogenicity as a tool for in-situ metabolic activity monitoring and drug assessment in biofilms. *iScience,* **24**, 102068 (2021).

6. L. Beuth, C. P. Pfeiffer, U. Schröder, Copper-bottomed: electrochemically active bacteria exploit conductive sulphide networks for enhanced electrogeneity. *Energy Environ. Sci.,* **13**, 3102-3109 (2020).

7. B. Cao *et al.*, Silver nanoparticles boost charge-extraction efficiency in Shewanella microbial fuel cells. *Science* **373**, 1336-1340 (2021).

8. X. Deng, D. Luo, A. Okamoto, Defined and unknown roles of conductive nanoparticles for the enhancement of microbial current generation: A review. *Bioresour. Technol.,* **350** (2022).

9. K. Rabaey, G. Lissens, S. D. Siciliano, W. Verstraete, A microbial fuel cell capable of converting glucose to electricity at high rate and efficiency. *Biotechnol. Lett.,* **25**, 1531-1535 (2003).

10. Y. Liu, F. Harnisch, K. Fricke, R. Sietmann, U. Schroder, Improvement of the anodic bioelectrocatalytic activity of mixed culture biofilms by a simple consecutive electrochemical selection procedure. *Biosens. Bioelectron.,* **24**, 1006-1011 (2008).

11. G. T. Sun, A. Thygesen, A. S. Meyer, Acetate is a superior substrate for microbial fuel cell initiation preceding bioethanol effluent utilization. *Appl. Microbiol. Biotechnol.,* **99**, 4905-4915 (2015).

12. X. Deng, N. Dohmae, K. H. Nealson, K. Hashimoto, A. Okamoto, Multi-heme cytochromes provide a pathway for survival in energy-limited environments. *Sci. Adv.,* **4**, eaao5682 (2018).

13. S. E. McGlynn, G. L. Chadwick, C. P. Kempes, V. J. Orphan, Single cell activity reveals direct electron transfer in methanotrophic consortia. *Nature,* **526**, 531-535 (2015).

14. A. C. Ruifrok, D. A. Johnston, Quantification of histochemical staining by color deconvolution. *Anal. Quant. Cytol. Histol.,* **23**, 291-299 (2001).

15. A. M. Seligman, M. J. Karnovsky, H. L. Wasserkrug, J. S. Hanker, Nondroplet ultrastructural demonstration of cytochrome oxidase activity with a polymerizing osmiophilic reagent, diaminobenzidine (DAB). *J. Cell Biol.,* **38**, 1-14 (1968).

16. A. Garber *et al.*, FeGenie: A comprehensive tool for the identification of iron genes and iron gene neighborhoods in genome and metagenome assemblies. *Front. Microbiol.,* **11**, 37 (2020).

17. D. Naradasu, A. Guionet, W. Miran, A. Okamoto, Microbial current production from Streptococcus mutans correlates with biofilm metabolic activity. *Biosens. Bioelectron.,* **162**, 112236 (2020).

18. T. Hyeon, Chemical synthesis of magnetic nanoparticles. *Chem. Commun.,* 10.1039/b207789b, 927-934 (2003).

19. C. R. Kalaiselvan *et al.*, Manganese ferrite (MnFe2O4) nanostructures for cancer theranostics. *Coord. Chem. Rev.,* **473**, 214809 (2022).

20. P. B. Kharat, S. B. Somvanshi, P. P. Khirade, K. M. Jadhav, Induction heating analysis of surface-functionalized nanoscale CoFe2O4 for magnetic fluid hyperthermia toward noninvasive cancer treatment. *ACS Omega,* **5**, 23378-23384 (2020).

21. S. B. Somvanshi *et al.*, Hyperthermic evaluation of oleic acid coated nano-spinel magnesium ferrite: Enhancement via hydrophobic-to-hydrophilic surface transformation. *J. Alloys Compd.,* **835**, 155422 (2020).

22. S. B. Somvanshi, P. B. Kharat, M. V. Khedkar, K. M. Jadhav, Hydrophobic to hydrophilic surface transformation of nano-scale zinc ferrite via oleic acid coating: Magnetic hyperthermia study towards biomedical applications. *Ceram. Int.,* **46**, 7642-7653 (2020).

23. S. B. Somvanshi *et al.*, Multifunctional nano-magnetic particles assisted viral RNA-extraction protocol for potential detection of COVID-19. *Mater. Res. Innov.,* **25**, 169-174 (2021).

24. S. B. Somvanshi *et al.*, Microfluidic paper-based aptasensor devices for multiplexed detection of pathogenic bacteria. *Biosens. Bioelectron.,* **207**, 114214 (2022).

25. Y. Jin, F. Liu, C. Shan, M. Tong, Y. Hou, Efficient bacterial capture with amino acid modified magnetic nanoparticles. *Water Res.,* **50**, 124-134 (2014).

26. Y. J. Sung *et al.*, Novel antibody/gold nanoparticle/magnetic nanoparticle nanocomposites for immunomagnetic separation and rapid colorimetric detection of Staphylococcus aureus in milk. *Biosens. Bioelectron.,* **43**, 432-439 (2013).

27. O. Johansson, J. Backman, Enhancement of immunoperoxidase staining using osmium tetroxide. *J. Neurosci. Methods,* **7**, 185-193 (1983).

28. S. E. Frederick, E. H. Newcomb, Cytochemical localization of catalase in leaf microbodies (peroxisomes). *J. Cell Biol.,* **43**, 343-353 (1969).

29. C. N. Nguyen, B. N. Tran, H. N. Thi, P. P. Huu, H. N. Thi, Physical absorption of folic acid and chitosan on dihydroartemisinin-loaded poly-lactic-co-glycolic acid nanoparticles via electrostatic interaction for their enhanced uptake and anticancer effect. *J. Nanomater.,* **2019** (2019).

30. S. Xie *et al.*, Folic acid coordinated Cu–Co site N-doped carbon nanosheets for oxygen reduction reaction. *ACS Appl. Mater. Interfaces.,* **13**, 3949-3958 (2021).

31. C. C. Wang, C. Y. Chang, C. Y. Chen, Study on metal ion adsorption of bifunctional chelating/ion-exchange resins. *Macromol. Chem. Phys.,* **202**, 882-890 (2001).

32. A. O. Chong, K. Oshima, K. B. Sharpless, Synthesis of dioxobis (tert-alkylimido) osmium (VIII) and oxotris (tert-alkylimido) osmium (VIII) complexes. Stereospecific vicinal diamination of olefins. *J. Am. Chem. Soc.,* **99**, 3420-3426 (1977).

33. R. S. McDowell, M. Goldblatt, Vibrational spectrum and force field of osmium tetroxide. *Inorg. Chem.,* **10**, 625-630 (1971).

34. I.-C. Masthoff *et al.*, Study of the growth process of magnetic nanoparticles obtained via the non-aqueous sol–gel method. *J. Mater. Sci.,* **49**, 4705-4714 (2014).

35. J. Walton, P. Wincott, N. Fairley, A. Carrick, *Peak fitting with CasaXPS: a Casa pocket book* (Accolyte Sci.,, 2010).

36. G. P. López, D. G. Castner, B. D. Ratner, XPS O 1s binding energies for polymers containing hydroxyl, ether, ketone and ester groups. *Surf. Interface Anal.,* **17**, 267-272 (1991).

37. T. Foglia, P. Barr, A. Malloy, M. Costanzo, Oxidation of unsaturated fatty acids with ruthenium and osmium tetroxide. *J. Am. Oil Chem. Soc.,* **54**, A870-A872 (1977).

38. S.-M. Hsu, E. Soban, Color modification of diaminobenzidine (DAB) precipitation by metallic ions and its application for double immunohistochemistry. *J. Histochem. Cytochem.,* **30**, 1079-1082 (1982).

39. A. Briones, The secrets of El Dorado viewed through a microbial perspective. *Front. Microbiol.,* **3**, 239 (2012).

40. H. He *et al.*, Characterization of a new electrochemically active bacterium, Lysinibacillus sphaericus D-8, isolated with a WO3 nanocluster probe. *Process Biochemi.,* **49**, 290-294 (2014).

41. L.-X. You *et al.*, Extracellular electron transfer of Enterobacter cloacae SgZ-5T via bi-mediators for the biorecovery of palladium as nanorods. *Environ. Int.,* **123**, 1-9 (2019).

42. F. Kracke, B. Virdis, P. V. Bernhardt, K. Rabaey, J. O. Krömer, Redox dependent metabolic shift in Clostridium autoethanogenum by extracellular electron supply. *Biotechnol. Biofuels.,* **9**, 1-12 (2016).

43. R. Gallardo *et al.*, In silico analysis of Clostridium acetobutylicum ATCC 824 metabolic response to an external electron supply. *Bioprocess Biosyst. Eng.,* **39**, 295-305 (2016).

44. L.-X. You *et al.*, Flavins mediate extracellular electron transfer in Gram-positive Bacillus megaterium strain LLD-1. *Bioelectrochemistry,* **119**, 196-202 (2018).

45. S. Li *et al.*, Extracellular electron transfer of Bacillus cereus biofilm and its effect on the corrosion behaviour of 316L stainless steel. *Colloids Surf. B Biointerfaces.,* **173**, 139-147 (2019).

46. B. E. Logan, J. M. Regan, Microbial fuel cells—challenges and applications. *Environ. Sci. Technol.,* **40**, 5172-5180 (2006).

47. B. H. Kim, I. S. Chang, G. M. Gadd, Challenges in microbial fuel cell development and operation. *Appl. Microbiol. Biotechnol.,* **76**, 485-494 (2007).

48. S. A. Masih, M. Devasahayam, Optimisation and the efficient design of an Enterobacter cloacae dual-chambered membrane microbial fuel cell for enhanced power generation. *Int. J. Ambient Energy,* **36**, 11-18 (2015).

49. L. Huang, X. Li, T. Cai, M. Huang, Electrochemical performance and community structure in three microbial fuel cells treating landfill leachate. *Process Saf. Environ. Prot.,* **113**, 378-387 (2018).

50. D. H. L. Leung *et al.*, Engineering S. oneidensis for performance improvement of microbial fuel cell—a mini review. *Appl. Biochem. Biotechnol.,* **193**, 1170-1186 (2021).

51. P. Choudhury, U. S. Prasad Uday, T. K. Bandyopadhyay, R. N. Ray, B. Bhunia, Performance improvement of microbial fuel cell (MFC) using suitable electrode and Bioengineered organisms: A review. *Bioengineered,* **8**, 471-487 (2017).

52. M. Li *et al.*, Microbial fuel cell (MFC) power performance improvement through enhanced microbial electrogenicity. *Biotechnol. Adv.,* **36**, 1316-1327 (2018).

53. J. Kan, L. Hsu, A. C. M. Cheung, M. Pirbazari, K. H. Nealson, Current production by bacterial communities in microbial fuel cells enriched from wastewater sludge with different electron donors. *Environ. Sci. Technol.,* **45**, 1139-1146 (2011).

54. D. L. White, S. Andrews, J. Faller, R. J. Barrnett, The chemical nature of osmium tetroxide fixation and staining of membranes by x-ray photoelectron spectroscopy. *Biochim. Biophys. Acta. Biomembr.,* **436**, 577-592 (1976).

55. J. Riemersma, Osmium tetroxide fixation of lipids for electron microscopy a possible reaction mechanism. *Biochim. Biophys. Acta. Biomembr.,* **152**, 718-727 (1968).

56. D. F. Rodrigues, M. Elimelech, Role of type 1 fimbriae and mannose in the development of Escherichia coli K12 biofilm: from initial cell adhesion to biofilm formation. *Biofouling,* **25**, 401-411 (2009).

57. J. F. Jones *et al.*, Oriented adhesion of Escherichia coli to polystyrene particles. *Appl. Environ. Microbiol.,* **69**, 6515-6519 (2003).

58. V. Carniello, B. W. Peterson, H. C. van der Mei, H. J. Busscher, Physico-chemistry from initial bacterial adhesion to surface-programmed biofilm growth. *Adv. Colloid Interface Sci.,* **261**, 1-14 (2018).

59. V. Fourmond *et al.*, SOAS: A free program to analyze electrochemical data and other one-dimensional signals. *Bioelectrochemistry,* **76**, 141-147 (2009).

60. J. G. Caporaso *et al.*, Ultra-high-throughput microbial community analysis on the Illumina HiSeq and MiSeq platforms. *ISME J.,* **6**, 1621-1624 (2012).

61. M. Hirai *et al.*, Library construction from subnanogram DNA for pelagic sea water and deep-sea sediments. *Microbes Environ.,* **32**, 336-343 (2017).

62. J. G. Caporaso *et al.*, QIIME allows analysis of high-throughput community sequencing data. *Nat. Methods,* **7**, 335-336 (2010).

63. B. J. Callahan *et al.*, DADA2: High-resolution sample inference from Illumina amplicon data. *Nat. Methods,* **13**, 581-583 (2016).

64. N. A. Bokulich *et al.*, Optimizing taxonomic classification of marker-gene amplicon sequences with QIIME 2's q2-feature-classifier plugin. *Microbiome,* **6**, 1-17 (2018).

65. T. Scientific, Pierce BCA protein assay kit. *Pierce BCA* **449** (2013).

66. Y. Liu, F. Harnisch, K. Fricke, R. Sietmann, U. Schröder, Improvement of the anodic bioelectrocatalytic activity of mixed culture biofilms by a simple consecutive electrochemical selection procedure. *Biosens. Bioelectron.,* **24**, 1006-1011 (2008).

67. C. Li, L. Zhang, L. Ding, H. Ren, H. Cui, Effect of conductive polymers coated anode on the performance of microbial fuel cells (MFCs) and its biodiversity analysis. *Biosens. Bioelectron.,* **26**, 4169-4176 (2011).

68. Y. Cui *et al.*, Biosynthesized iron sulfide nanoparticles by mixed consortia for enhanced extracellular electron transfer in a microbial fuel cell. *Bioresour. Technol.,* **318**, 124095 (2020).

69. X. Xu, Q. Zhao, M. Wu, J. Ding, W. Zhang, Biodegradation of organic matter and anodic microbial communities analysis in sediment microbial fuel cells with/without Fe (III) oxide addition. *Bioresour. Technol.,* **225**, 402-408 (2017).

Chapter 6 Summary and Future Perspectives

6.1 Summary

This dissertation investigates how *Pseudomonas aeruginosa* maintains viability under anaerobic, energy-limited conditions by using extracellular electron transfer (EET). Through a combination of electrochemical quantification, genetic manipulation, and molecular transport analysis, this work defines how redox-active metabolites (RAMs), efflux pumps, and membrane permeability collectively determine the efficiency of RAM-mediated metabolism and shape bacterial survival.

A high-throughput 96-well electrochemical platform was developed to precisely quantify PCN-driven EET and establish the minimal metabolic rate required to sustain viability without growth. This platform enabled mechanistic dissection of transport processes that constrain electron-shuttle function. Efflux pumps, traditionally viewed as detoxification systems, were shown to act instead as bioenergetic regulators: their activity dissipates the proton-motive force, drives compensatory metabolism, and reduces antibiotic resistance under low-energy conditions. Membrane permeability emerged as a second major determinant of RAM-supported metabolism. Highly permeable RAMs, such as pyocyanin, sustain higher metabolic flux and enhance antibiotic susceptibility through metabolism-linked stress.

Extending these insights to natural environments, osmium-grafted magnetic nanobeads were developed as a culture-free tool to selectively enrich electroactive bacteria (EAB) based on outer-membrane redox activity. This method rapidly isolated electrogenic taxa from environmental microbiota, improving current generation and enabling the identification of microbes that rely on EET to survive in low-energy niches.

Together, these findings establish transport-governed EET as a central mechanism supporting bacterial persistence under energetic scarcity and provide new methodological and conceptual tools for investigating redox-based survival strategies across both pathogenic and environmental microbial systems.

6.2 Future perspectives

6.2.1 Essential metabolic functions for survival under low-energy conditions

This work demonstrates that under low-energy, non-growing conditions, cells are not metabolically quiescent but instead maintain a minimal yet adjustable level of metabolic activity. In Chapter 2, by using efflux pump activity and PCN-mediated redox cycling as quantitative readouts, we showed that cells actively increase metabolic flux to compensate for excessive PMF dissipation. These findings indicate that low-energy cells possess positive metabolic requirements for survival, rather than persisting as passively surviving entities, and they highlight the central role of PMF homeostasis in low-power physiology.

A natural next question is: beyond PMF, what are the critical cellular functions that require a baseline metabolic flux for survival under low-energy conditions? Two candidates emerging from this work are ion homeostasis and membrane homeostasis. First, prior studies have shown that elevated ion concentrations impose osmotic stress, forcing cells to spend ATP or PMF to prevent plasmolysis and maintain turgor (1, 2). How bacteria allocate limited metabolic resources to operate ion transporters and sustain osmotic balance under energy limitation remains largely unresolved, and represents a promising direction for future research. Second, membrane homeostasis—particularly the maintenance of lipid composition, fluidity, and integrity—may represent an additional and substantial energetic demand. This hypothesis is supported by two lines of evidence: (i) in collaborative work with the Newman laboratory,

membrane-disrupting agents such as colistin dramatically reduced survival compared with antibiotics targeting intracellular processes (3); and (ii) findings from Chapter 4 show that RAM-mediated redox cycling and metabolic flux are tightly coupled to membrane permeability and transport properties. Together, these observations suggest that membrane maintenance may be a central component of the energetic floor that defines low-energy survival. Future experiments that directly perturb lipid remodeling, membrane energetics, and permeability regulation under anaerobic, energy-limited conditions—while monitoring both current output and viability—will be essential for constructing a more complete model of bacterial maintenance metabolism.

6.2.2 Can cells reach even lower metabolic states?

A second direction is to investigate whether cells can enter metabolic states that operate at rates even lower than those of non-growing but readily resuscitable populations. Viable-but-non-culturable (VBNC) cells represent an extreme low-energy state in which metabolic activity is markedly reduced (4). Previous work comparing VBNC populations with persister-like cells—cells that survive antibiotic exposure and can resume growth under oxic, nutrient-rich conditions—has shown that VBNC cells exhibit substantially lower membrane potential and PMF (5). This observation raises an intriguing possibility: do VBNC cells actively downshift their metabolic rate and relinquish certain maintenance functions to further minimize energetic demand? If so, this would suggest that processes essential for survival in the non-growing state may become partially or entirely dispensable in the VBNC state.

Genetic approaches offer a powerful route to probe the minimal energetic architecture required for bacterial survival. During research exchange at the Newman laboratory, genome-wide screening strategies such as Tn-seq were being explored to identify determinants of survival under energy-limited conditions. Coupling such genetic

screens with the high-throughput electrochemical platform developed in this thesis could enable direct mapping of gene deletions to maintenance metabolism, thereby defining which cellular processes constitute the irreducible energetic core necessary for long-term viability.

6.2.3 Applying rapid EET-enrichment tools to assess the generality of low-energy survival strategies across natural microbial ecosystems

The osmium-grafted magnetic nanobead enrichment strategy developed in Chapter 5 opens new opportunities for characterizing extracellular electron transfer (EET) across diverse natural ecosystems. Having demonstrated in earlier chapters that EET provides a crucial mechanism for sustaining viability under energy-limited conditions in *Pseudomonas aeruginosa*, an important next step is to investigate whether similar strategies are employed by environmentally relevant microorganisms. By applying the M@FA-Os NP–based enrichment method to anaerobic or microoxic environments—such as sediments, wastewater, subsurface aquifers, and hypoxic biofilms—researchers can rapidly isolate distinct electroactive taxa and compare their redox-based survival strategies.

6.3 References

1. J. M. Wood, Bacterial responses to osmotic challenges. *J Gen Physiol* **145**, 381-388 (2015).
2. W. Epstein, The roles and regulation of potassium in bacteria. *Prog Nucleic Acid Res Mol Biol* **75**, 293-320 (2003).
3. J. A. Ciemniecki, C.-L. Ho, R. D. Horak, A. Okamoto, D. K. Newman, Mechanistic study of a low-power bacterial maintenance state using high-throughput electrochemistry. *Cell* **187**, 6882-6895.e6888 (2024).
4. J. Liu, L. Yang, B. V. Kjellerup, Z. Xu, Viable but nonculturable (VBNC) state, an underestimated and controversial microbial survival strategy. *Trends in Microbiology* **31**, 1013-1023 (2023).

5. X. Jin *et al.*, Sensitive bacterial V*m* sensors revealed the excitability of bacterial V*m* and its role in antibiotic tolerance. *Proceedings of the National Academy of Sciences* **120**, e2208348120 (2023).

Published Content and Contributions

1. Ciemniecki, J. A., **Ho, C. L.**, Horak, R. D., Okamoto, A., & Newman, D. K. (2024). Mechanistic study of a low-power bacterial maintenance state using high-throughput electrochemistry. *Cell*, *187*(24), 6882-6895. DOI: 10.1016/j.cell.2024.09.042

C.-L.H. was responsible for performing the experiments, analyzing the data, and preparing the manuscript. This work was adapted into **Chapter 2**.

2. **Ho, C. L.**, Horak, R. D., K. Thalhammer, Newman, D. K., & Okamoto, A. (2025). Efflux pump activity limits an anaerobic metabolism powered by phenazines redox cycling. In prep.

C.-L.H. was responsible for conceptualizing the study, performing the experiments, analyzing the data, and preparing the manuscript. This work was adapted into **Chapter 3**.

3. **Ho, C. L.**, & Okamoto, A. (2025). Diffusion-driven redox metabolism sensitizes Pseudomonas aeruginosa to antibiotics under a low-energy condition. In prep.

C.-L.H. was responsible for conceptualizing the study, performing the experiments, analyzing the data, and preparing the manuscript. This work was adapted into **Chapter 4**.

4. **Ho, C. L.**, Emran, M. Y., Ihara, S., Huang, W., Wakai, S., Li, W. P., & Okamoto, A. (2023). Osmium-grafted magnetic nanobeads improve microbial current generation via culture-free and quick enrichment of electrogenic bacteria. *Chemical Engineering Journal*, *466*, 142936. DOI: 10.1016/j.cej.2023.142936

C.-L.H. was responsible for conceptualizing the study, performing the experiments, analyzing the data, and preparing the manuscript. This work was adapted into **Chapter 5**.

Acknowledgment

Throughout my journey from undergraduate studies to the final stage of my doctoral degree, I have been fortunate to meet countless individuals who supported and encouraged me. I would like to express my deepest gratitude to everyone who has accompanied me along the way

First, I would like to thank my undergraduate advisor, Professor Chen-Sheng Yeh, senior student Wei-Peng Li, and all the members of my former laboratory. Your guidance and support gave me the opportunity to pursue research in Japan, which ultimately led me into the fascinating world of microbiology.

I am also grateful to the Chinese friends I met in Japan—Huang Wenyuan, Luo Dan, Yan Kangmin, Wen Xinxin, Deng Xiao, and all the members of the NIMS “old lunch group.” Your companionship in both research and daily life helped me quickly adapt to living and studying abroad. Through your support and our many academic exchanges, I was able to gain a much deeper understanding of microbiology and electrochemistry than I could have achieved on my own.

My sincere thanks go to my Japanese colleagues as well. To Ihara: from our master’s program to our PhD years, we have gone through so much together—preparing JSPS applications, attending the ASM conference in the United States, cleaning the laboratory, and now preparing for graduation. More than colleagues, I consider us comrades. Thank you for your thoughtful advice on research and writing, and for your responsible and dependable attitude toward laboratory affairs. Working with you has been a genuine pleasure.

I also wish to thank Fujikawa and Takenawa-san. Every discussion with you has been a valuable learning experience. Your patience and guidance deepened my

understanding of molecular biology and encouraged me to continue exploring this field further.

I am grateful to our administrative staff, Yamaguchi and Uematsu-san, for guiding me through all institutional procedures, from graduation requirements to expense management and arrangements for my research visit to the United States. I also thank Sakurai and Naito-san for your assistance in the laboratory; you saved me countless hours in locating reagents and materials and making 96-well electrode plates.

My heartfelt thanks go to my friends in Taiwan—Kuo Yi-Ho, Yao Mu-Li, Liao Hsin-Yen, Chen Yi-An, Holly, Yang Pei-Hsuan, and Chang Yung-Hao. During the more stressful periods of my studies, your companionship and conversations helped me regain balance and perspective. A special thanks to Kuo Yi-Ho for taking care of Diu while I was away from Japan.

I also want to thank Pham, Silvia, Arpit, and Mariam. Conversations with you have always been refreshing—whether about research, life, or cross-cultural insights—and I truly treasured those moments.

I extend my gratitude to the members of the Nano-bio group for your continued support in research.

Next, I would like to thank everyone in the Newman Lab at Caltech who welcomed me during my short-term research stay. I am especially grateful to Dr. John, Richard, and Korbi for your scientific guidance; my thesis would not have reached its current depth without your help. I am also deeply thankful to Professor Dianne Newman for your mentorship and for the wonderful memory of enjoying the autumn leaves together in Japan—what a remarkable trip.

In addition, I would like to extend my sincere gratitude to my host, Nancy, and her family, Flanagan and Caira, for their companionship and support during my time at

Caltech. Your kindness and warmth made my stay in the United States truly meaningful and unforgettable.

I would also like to express my sincere appreciation to my supervisor, Professor Okamoto. You cultivated my interest from microbial electrochemistry to physiology. When I had the opportunity to collaborate with the Newman Lab, I realized how deeply passionate I am about microbial physiology. Thank you for your mentorship and encouragement throughout these years.

Finally, I would like to thank my family, my sweet girl Diu, my beloved partner, Chiang Huai-En, and his family. Without your unconditional love and support, I would never have reached this milestone. Thank you for giving me strength whenever I felt anxious or uncertain, and for helping me rise again each time I stumbled.

As I close this chapter of my academic journey, I am reminded that none of these achievements were accomplished alone. Every step forward was made possible by the guidance, trust, and generosity of those around me.

As Isaac Newton once wrote, *"If I have seen further, it is by standing on the shoulders of giants."*

This thesis stands upon the support, wisdom, and kindness of all of you. For that, I am deeply and forever grateful.